

Supporting Information

Super-Ion Inspired Colorful Hybrid Perovskite Solar Cells

Hong Fang, Puru Jena*

Department of Physics, Virginia Commonwealth University, 701 West Grace Street, 23284,
VA, United States
E-mail: pjena@vcu.edu

Content

I. Calculated ionization potential and electron affinity of some super ions.....	2
II. Derivation of a model for band gaps of ionic crystals.....	3
III. Effects of the ionicity $\Delta\chi$ and Coulomb potential V_c on the band gap position.....	13
IV. Results of the molecular dynamics simulations.....	14
V. Simulated X-ray diffraction pattern.....	28
VI. Effective ionic radii of the super ions.....	29
VII. NBO analysis of the super alkali halides.....	57
VIII. DFT calculated electronic band structures.....	58
IX. DFT calculated electronic density of states.....	64
X. Phonon calculations of $\text{MAGe}(\text{BH}_4)_3$ and $\text{MASn}(\text{BH}_4)_3$	73
XI. Stability analyses of the hybrid perovskite under moisture.....	74
XII. Vibrational spectra of super halide molecule with water.....	76
XIII. Inorganic super alkali $[\text{Li}_3\text{O}]^+$	78
XIV. Electronic structures of the hybrid perovskites composed of hyper halogens.....	79
XV. Bowing factors of $\text{AM}[\text{I}_{1-x}(\text{BH}_4)_x]_3$ ($\text{A} = \text{MA}$ and FA ; $\text{M} = \text{Ge}$ and Sn ; $x = 0, 1/3, 2/3, 1$) from band gaps.....	80

I. Calculated ionization potential and electron affinity of some super ions

Table S1 Calculated ionization potential of organic super-alkalis (methylammonium $[\text{CH}_3\text{NH}_3]^+$, MA^+ ; formamidinium $[\text{HC}(\text{NH}_2)_2]^+$, FA^+), inorganic super-alkali, $[\text{Li}_3\text{O}]^+$, and electron affinity of super-halogens $[\text{MX}_3]^-$ ($\text{M} = \text{Ge}, \text{Sn}, \text{Pb}$; $\text{X} = \text{Cl}, \text{Br}, \text{I}$), $[\text{BH}_4]^-$, as well as hyper-halogens $[\text{M}(\text{BH}_4)_3]^-$ ($\text{M} = \text{Ge}, \text{Sn}$) compared to those of the elementary ions. $[\text{M}(\text{BH}_4)_3]^-$ are called hyper-halogens as they are composed of super-halogen, $[\text{BH}_4]^-$ [1]. The ionization potential is computed as the difference between energy of the cation state and the neutral state. The electron affinity is the difference between the energy of the neutral and the anion states. The energies of the super-alkalis and super- and hyper-halogens (commonly referred to as super-ions) are calculated from their relaxed geometries with corresponding ionic states. Note that the ionization potential of the super-alkalis are smaller than that of Li^+ and the electron affinity of the super-halogens are (close to or) higher than that of Cl^- .

Alkali and Super-alkalis Ionization Potential (eV)		Halogen and (Super/Hyper) Halogens Electron Affinity (eV)	
Li^+	5.62	Cl^-	3.71
MA^+	4.13	$[\text{GeCl}_3]^-$	4.14
FA^+	4.81	$[\text{GeBr}_3]^-$	4.08
Cs^+	4.01	$[\text{GeI}_3]^-$	3.99
$[\text{Li}_3\text{O}]^+$	3.88	$[\text{SnCl}_3]^-$	4.40
		$[\text{SnBr}_3]^-$	4.25
		$[\text{SnI}_3]^-$	4.12
		$[\text{PbBr}_3]^-$	4.76
		$[\text{PbI}_3]^-$	4.42
		$[\text{BH}_4]^-$	3.42
		$[\text{Ge}(\text{BH}_4)_3]^-$	4.46
		$[\text{Sn}(\text{BH}_4)_3]^-$	4.41

II. Derivation of a model for band gaps of ionic crystals

An archetypal example of an ionic crystal is NaCl. An ionic bond is spontaneously formed between Na^+ and Cl^- ions when the two atoms, initially far apart, are brought into the vicinity of each other. The bond formation first involves energy cost (i.e. ionization potential, IP) to ionize Na and the energy gain (i.e. electron affinity, EA) to add that electron to Cl. The net energy price in the process is,

$$h_2 = \text{IE}(\text{alkali}) - \text{EA}(\text{halogen}) \quad (\text{S1})$$

Similarly, it costs the energy,

$$h_1 = \text{IE}(\text{halogen}) - \text{EA}(\text{alkali}) \quad (\text{S2})$$

to take the valence electron from Cl and put it on Na. The energy difference between these two

$$h_1 - h_2 = \chi_h - \chi_a = \Delta\chi \quad (\text{S3})$$

is a measure of the ionicity of the bond. Note that $\chi_h = \text{IE}(\text{halogen}) + \text{EA}(\text{halogen})$ and $\chi_a = \text{IE}(\text{alkali}) + \text{EA}(\text{alkali})$ correspond to Pauling's electronegativity of the halogen and the alkali, respectively. This process can be represented by a one-dimensional potential well as shown in Figure S1. When the two atoms are far away from each other, the Coulomb interaction V_c is zero.

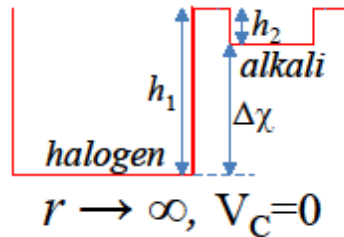


Fig. S1 One-dimensional representation of an alkali (e.g. Na) and a halogen (e.g. Cl) separated far apart ($r \rightarrow \infty$), where the Coulomb potential is zero ($V_c = 0$).

Spontaneous formation of the ionic bond between Na and Cl at a critical distance is made possible when Coulomb attraction between the two ions overcomes the energy cost h_2 as shown in Figure S2. As the two ions come closer, they will form the molecule with a shorter interatomic distance at its energy minimum.

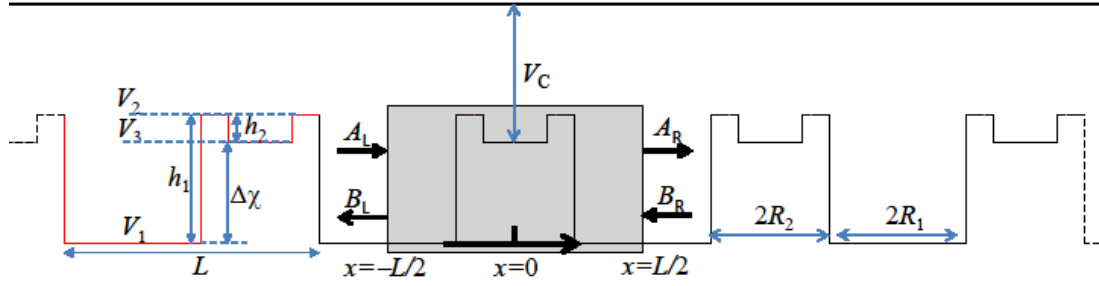


Fig. S2 The one-dimensional square-potential model of an ionic crystal. The unit cell, as highlighted in red, consists of one cation and one anion separated by the equilibrium bond length. L is the lattice parameter and R_1 (R_-) and R_2 (R_+) are the ionic radius of the anion and the cation, respectively. The energy of the whole system is lowered due to the Coulomb interaction (V_c) between the cations and anions. The lattice is equivalent to a series of repetitive potential barriers as indicated in the shaded area. A_L and A_R represent the electron waves moving in the x -direction on the left and right of the barrier, respectively, while B_L and B_R represent the electron wave moving in the opposite x -direction.

A one-dimensional model of periodic lattice is formed with repetitive potential units as shown in Figure S2. The energy of the whole system will be lowered by V_c due to the Coulomb interaction between the cations and the anions. An electron can be viewed as moving in an equivalent lattice consisting of repetitive energy barriers as highlighted in the shaded area of Figure S2. For the convenience of calculation, we also move up the energy of the whole system so that the potential of the anion core (V_1) in Figure S2 is zero. The cation is represented by a simplified core-shell model with V_3 the core potential and its width the core radius. The difference h_2 between V_2 and V_3 is the shell energy barrier that binds the valence electron to the cation core. Later we will show that, compared to h_1 , h_2 is small enough to be neglected. The resulting model potential under such approximation will become a periodic square potential with a step height of $\Delta\chi$. In such case, the electron under consideration needs to tunnel through the single barrier of $\Delta\chi$ to move from the halogen to the alkali. A simple analytic form of the electron transmission probability can be obtained as will be shown in Eq. (S33) in the following.

We represent the electron by a wave packet which is the superposition of the energy eigenstates. These chosen states are also eigenstates of the translation operator with respect to the lattice constant and adopt the form of Bloch waves which are delocalized throughout the whole lattice. At each edge of the barrier, the wave will reflect as well as transmit. The reflected and transmitted waves will then interfere -- some adding constructively while some adding destructively -- resulting in energy bands with gaps between them. There are two equivalent ways to formulate this problem. One is to compute the relation between the wave

on the left side of the barrier and the wave on the right side of the barrier, as shown in Figure S2 by A_L/B_L and A_R/B_R , respectively [2].

$$\begin{pmatrix} A_L \\ B_L \end{pmatrix} = \mathbf{T} \begin{pmatrix} A_R \\ B_R \end{pmatrix} \quad (\text{S4})$$

\mathbf{T} is called the transmission matrix

$$\mathbf{T} = \begin{pmatrix} t_{11} & t_{12} \\ t_{21} & t_{22} \end{pmatrix}. \quad (\text{S5})$$

This method is mathematically more convenient for the calculation, especially when there are multiple piecewise potential barriers between the left and right wave signals. The second method is to compute the relation between the incoming wave A_L/B_R and the outgoing wave A_R/B_L in Figure S2 [2].

$$\begin{pmatrix} A_R \\ B_L \end{pmatrix} = \mathbf{S} \begin{pmatrix} A_L \\ B_R \end{pmatrix} \quad (\text{S6})$$

\mathbf{S} is called the scattering matrix.

$$\mathbf{S} = \begin{pmatrix} t & \tilde{r} \\ r & \tilde{t} \end{pmatrix}, \quad (\text{S7})$$

where t (r) and \tilde{t} (\tilde{r}) are the transmission (reflection) amplitudes on the left and on the right of the barrier, respectively. From Eq. (S4-S7), the scattering matrix can be represented by the elements of the transmission matrix as

$$\mathbf{S} = \begin{pmatrix} t & \tilde{r} \\ r & \tilde{t} \end{pmatrix} = \begin{pmatrix} 1/t_{11} & -t_{12}/t_{11} \\ t_{21}/t_{11} & \det(\mathbf{T})/t_{11} \end{pmatrix}, \quad (\text{S8})$$

where $\det(\mathbf{T})$ is the determinant of the transmission matrix.

For a lattice system with N unit cells and periodic boundary condition, it requires $\mathbf{T}^N = \mathbf{I}$ (the identity matrix), hence $\det(\mathbf{T}) = 1$. This yields

$$t = \tilde{t} \quad (\text{S9})$$

according to Eq. (S8). Because of the conservation law, i.e. the incoming signal must equal the outgoing signal

$$|A_L|^2 + |B_R|^2 = |A_R|^2 + |B_L|^2. \quad (\text{S10})$$

The scattering matrix then must be a unitary matrix

$$\mathbf{S}^\dagger \mathbf{S} = \mathbf{I}, \quad (\text{S11})$$

where \mathbf{S}^\dagger is the adjoint of the scattering matrix. From Eq. (S11), we obtain

$$t^* \tilde{r} + r^* \tilde{t} = 0, \quad (\text{S12})$$

We write the transmission and reflection amplitudes into complex forms as

$$t = \tilde{t} = |t| e^{-i\varphi}, \quad r = |r| e^{i\theta}, \quad \tilde{r} = |r| e^{i(\theta+2\Delta)}, \quad (\text{S13})$$

where we have used Eq. (S9). We also used the conservation law

$$|t|^2 + |r|^2 = |\tilde{t}|^2 + |\tilde{r}|^2, \quad (\text{S14})$$

so that

$$|\tilde{r}| = |r|. \quad (\text{S15})$$

In Eq. (S13), φ is the phase difference between the transmitted and the incident waves. θ and $(\theta + 2\Delta)$ are the phase delays of the reflected waves on the left and the right of the barrier, respectively. Substituting Eq. (S13) into Eq. (S12), we obtain

$$t = \sqrt{T} e^{-i\varphi}, \quad r = \pm i \sqrt{R} e^{-i(\varphi+\Delta)}, \quad \tilde{r} = \pm i \sqrt{R} e^{-i(\varphi-\Delta)}, \quad (\text{S16})$$

where $T = |t|^2$ and $R = |r|^2$ are the transmission and the reflection probability, respectively.

A general electron eigenstate with energy E can be written as

$$\Phi_E = a\Phi_R + b\Phi_L \quad (\text{S17})$$

with the wave incident from the left

$$\Phi_L = \begin{cases} e^{ikx} + re^{-ikx} & (x \leq -L/2) \\ te^{ikx} & (x \geq L/2) \end{cases} \quad (\text{S18})$$

and from the right

$$\Phi_R = \begin{cases} te^{-ikx} & (x \leq -L/2) \\ e^{-ikx} + \tilde{r}e^{ikx} & (x \geq L/2) \end{cases}, \quad (\text{S19})$$

where

$$k = \frac{\sqrt{2m(E - V_1)}}{\hbar} = \frac{\sqrt{2mE}}{\hbar} \quad (\text{S20})$$

with $V_1=0$ in our setting. m is the electron mass. Since Φ_E is a Bloch wave, the wave function and its first derivative should satisfy

$$\begin{cases} \Phi_E(x+L) = e^{iqL}\Phi_E(x) \\ \Phi_E'(x+L) = e^{iqL}\Phi_E'(x) \end{cases}. \quad (\text{S21})$$

Solving Eq. (S20), we get

$$\cos(qL) = \frac{t^2 - r\tilde{r}}{2t} e^{ikL} + \frac{1}{2t} e^{-ikL}. \quad (\text{S22})$$

Inserting Eq. (S16) into Eq. (S22), we finally obtain

$$\cos(qL) = \cos(kL - \varphi) / \sqrt{T}. \quad (\text{S23})$$

The left-hand-side (LHD) of this equation has values between $[-1, 1]$. The numerator on the right-hand-side (RHS) also has values between $[-1, 1]$. However, since the transmission probability T must be ≤ 1 , some values of the RHS will be out of the range $[-1, 1]$ and the corresponding energy will be inaccessible, hence presence of the energy band gaps. Figure S3 is a graphical form of Eq. (S23). Solutions of Eq. (S23) are those between the two red lines, forming three energy bands and two energy gaps. The extreme values of the RHS correspond to

$$kL - \varphi = n\pi \quad (n = \text{integer}). \quad (\text{S24})$$

Eq. (S23) suggests that the band gap depends on the transmission probability T of the electron wave in the lattice. With smaller transmission probability, larger range of kL values will correspond to RHS values that are out of $[-1, 1]$, hence larger band gaps. With certain value of kL (i.e. energy according to Eq. (S20)), the phase delay φ of the transmission will dictate when Eq. (S24) is satisfied, hence will decide the position of the band gap.

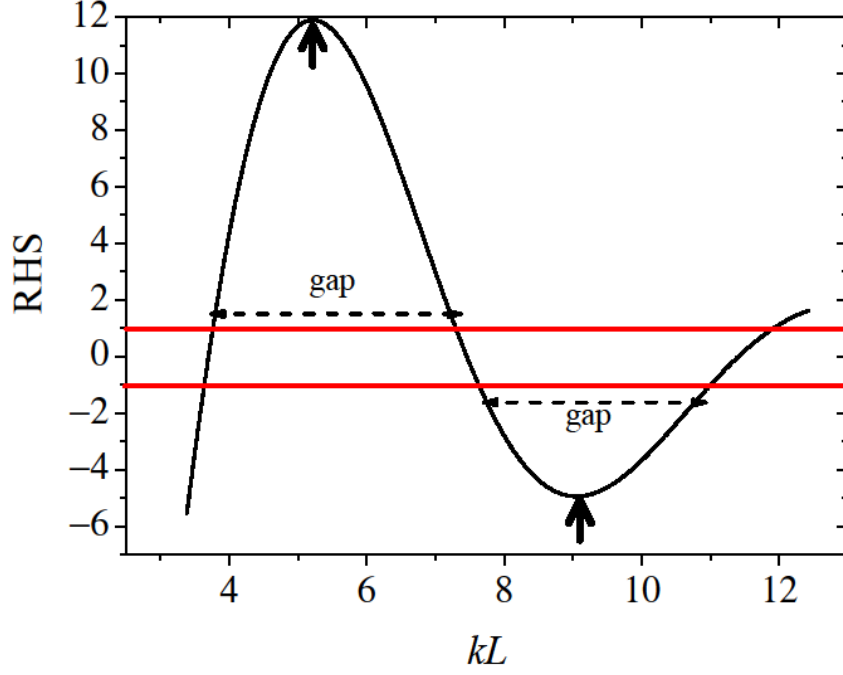


Fig.S3 Graphical representation of Eq. (S23). The solutions of the right hand side (RHS) are within the range of $[-1, 1]$ between the red lines. The black arrows indicate the positions of the extreme values of the periodic function $\cos(kL - \varphi)$ on the RHS when Eq. (S24) is satisfied.

In our model for (super) alkali halides, we are dealing with only one valence electron per unit cell. For a total of N unit cells, the first band will contain N energy states. Therefore, the band gap between the valence and the conduction bands of the model will be the first gap to appear.

To further derive the expressions for the transmission probability T and the phase angle φ in our one-dimensional model, we note from Eq. (S10),

$$|A_L|^2 - |B_L|^2 = |A_R|^2 - |B_R|^2. \quad (\text{S25})$$

This can be also obtained directly from the conservation of the momentum on the left and right sides of the barrier

$$\hbar k_L (|A_L|^2 - |B_L|^2) = \hbar k_R (|A_R|^2 - |B_R|^2) \quad (\text{S26})$$

with $k_L = k_R = k$ in our model. For the electron incident from the left, $B_R = 0$, we have

$$T = \left| \frac{A_R}{A_L} \right|^2, \quad R = \left| \frac{B_L}{A_L} \right|^2 \quad (\text{S27})$$

and

$$\begin{pmatrix} A_L \\ B_L \end{pmatrix} = \begin{pmatrix} t_{11} A_R \\ t_{21} A_R \end{pmatrix} \quad (\text{S28})$$

according to Eq. (S4)-(S5). Therefore, we obtain

$$T = \left| \frac{1}{t_{11}} \right|^2, \quad (\text{S29})$$

where

$$t_{11} = \frac{1}{2}(m_{11} + m_{22}) + \frac{i}{2} \left(km_{12} - \frac{m_{21}}{k} \right). \quad (\text{S30})$$

m_{ij} in Eq. (S30) are the elements of the matrix equal to the product of the transmission matrices for the three barrier regions in Figure S2 – two V_3 regions and one V_2 region. These matrix elements are cosh or sinh functions of κ_2 and κ_3 with

$$\kappa_2 = \sqrt{2m(V_2 - E)}/\hbar, \quad \kappa_3 = \sqrt{2m(V_3 - E)}/\hbar. \quad (\text{S31})$$

m is the electron mass. With

$$V_3 \approx V_2 = \Delta\chi, \quad (\text{S32})$$

the problem can be simplified significantly, and we can obtain

$$T = \frac{1}{1 + \frac{1}{4} \left(\frac{k}{\kappa} + \frac{\kappa}{k} \right)^2 \sinh^2(2\kappa R_2)}, \quad (\text{S33})$$

where

$$\kappa = \frac{\sqrt{2m(\Delta\chi - E)}}{\hbar}. \quad (\text{S34})$$

In our model, as shown in Figure S2, the difference between V_3 and V_2 is h_2 in Eq. (S1) which is the difference between ionization potential of the cation and the electron affinity of the anion. Table S2 lists these values for the super alkali halides considered in this study. We can see that, for all the ionic bonds considered here, $h_2 \ll h_1$, confirming that Eq. (S32) is valid. Thus, we will use Eq. (S33) in the following calculations.

TABLE S2 Calculated h_1 , h_2 , the electronegativity of super-halogen χ_h , the electronegativity of super-alkali χ_a and the ionicity $\Delta\chi$ for the super-alkali halide bonds, as defined in Eq. (S1)-(S3). MA⁺ refers to methylammonium [CH₃NH₃]⁺ and FA⁺ refers to formamidinium [HC(NH₂)₂]⁺.

Ionic Bond	h_1 (eV)	h_2 (eV)	χ_h (eV)	χ_a (eV)	$\Delta\chi$ (eV)
LiF	20.86	2.12	24.91	6.17	18.74
LiCl	14.64	1.93	18.90	6.17	12.73
LiBr	13.30	2.05	17.41	6.17	11.24
LiI	11.67	2.34	15.51	6.17	9.34
NaF	20.81	1.90	24.91	6.00	18.91
NaCl	14.59	1.71	18.90	6.00	12.90
NaBr	13.25	1.84	17.41	6.00	11.41
NaI	11.62	2.12	15.51	6.00	9.51
KF	20.88	0.98	24.91	5.02	19.89
KCl	14.67	0.79	18.90	5.02	13.88
KBr	13.32	0.91	17.41	5.02	12.39
KI	11.69	1.20	15.51	5.02	10.49
RbF	21.03	0.82	24.91	4.70	20.21
RbCl	14.81	0.63	18.90	4.70	14.20
RbBr	13.47	0.75	17.41	4.70	12.71
RbI	11.84	1.03	15.51	4.70	10.81
CsF	20.96	0.49	24.91	4.46	20.45
CsCl	14.74	0.30	18.90	4.46	14.44
CsBr	13.40	0.42	17.41	4.46	12.95
CsI	11.76	0.71	15.51	4.46	11.05
CsGeCl ₃	9.48	0.60	13.34	4.46	8.88
CsGeBr ₃	8.91	0.57	12.78	4.46	8.32
CsGeI ₃	8.20	0.52	12.14	4.46	7.68
CsSnCl ₃	9.53	0.16	13.81	4.46	9.35
CsSnBr ₃	8.92	0.27	13.11	4.46	8.65
CsSnI ₃	8.23	0.30	12.38	4.46	7.92
MAGeCl ₃	10.50	0.77	13.34	3.61	9.73
MAGeBr ₃	9.92	0.74	12.78	3.61	9.17
MAGeI ₃	9.21	0.69	12.14	3.61	8.53
MAGe(BH ₄) ₃	9.64	1.13	12.12	3.61	8.51

MASnCl ₃	10.54	0.34	13.81	3.61	10.20
MASnBr ₃	9.93	0.45	13.11	3.61	9.50
MASnI ₃	9.24	0.47	12.38	3.61	8.77
MASn(BH ₄) ₃	9.63	0.83	12.42	3.61	8.81
MAPbBr ₃	10.55	0.71	13.45	3.61	9.84
MAPbI ₃	9.67	0.77	12.49	3.61	8.88
FAGeCl ₃	11.33	3.10	13.34	5.10	8.24
FAGeBr ₃	10.75	3.07	12.78	5.10	7.68
FAGeI ₃	10.04	3.02	12.14	5.10	7.04
FAGe(BH ₄) ₃	10.48	3.45	12.12	5.10	7.02
FASnCl ₃	11.37	2.67	13.81	5.10	8.71
FASnBr ₃	10.76	2.77	13.11	5.10	8.01
FASnI ₃	10.07	2.80	12.38	5.10	7.28
FASn(BH ₄) ₃	10.45	3.15	12.42	5.10	7.32

The next task is to find the expression of the phase delay in our model. Combining Eq. (S8) and (S30), we can write the transmitted amplitude in the \mathbf{S} matrix as

$$t = \sqrt{T} e^{-i\varphi} = \frac{1}{t_{11}} = \frac{2}{(m_{11} + m_{22}) + i \left(km_{12} - \frac{m_{21}}{k} \right)}. \quad (\text{S35})$$

This suggests that

$$\cot \varphi = \frac{m_{11} + m_{22}}{km_{12} - m_{21}/k} = \frac{2 \coth(2\kappa R_2)}{k/\kappa - \kappa/k}. \quad (\text{S36})$$

To obtain even simpler expressions for the transmission probability T (Eq. (S33)) and the transmission phase angle φ (Eq.(S36)), we note that, numerically, the value of $2\kappa R_2$ should be much larger than 1. This can be readily seen by using the ionic radii of the alkali and the ionicity in Table S2. The smallest value of ionicity in Table S2 is 7.7 eV, while the smallest ionic radius of the alkali is 0.9 Å. Given that we are only interested in the appearance of the first band gap, the energy of the electron is supposed to be much less than 7.7 eV. Thus, according to Eq. (S34), the following is valid for even the smallest $2\kappa R_2$

$$2\kappa R_2 > 10 \gg 1. \quad (\text{S37})$$

Therefore, it is fitting to write

$$\sinh(2\kappa R_2) \approx e^{2\kappa R_2}, \quad \cosh(2\kappa R_2) \approx e^{2\kappa R_2}, \quad \coth(2\kappa R_2) \approx 1. \quad (\text{S38})$$

Thus, Eq. (S33) and (S36) can be further simplified as

$$T = \frac{1}{1 + \frac{1}{4} \left(\sqrt{\frac{\varepsilon}{1-\varepsilon}} + \sqrt{\frac{1-\varepsilon}{\varepsilon}} \right)^2 \exp \left(4 \frac{\sqrt{2m\Delta\chi}}{\hbar} \sqrt{1-\varepsilon} R_2 \right)} \quad (\text{S39})$$

and

$$\varphi = \text{acot} \left(\frac{2}{\sqrt{\frac{\varepsilon}{1-\varepsilon}} - \sqrt{\frac{1-\varepsilon}{\varepsilon}}} \right), \quad (\text{S40})$$

which are defined with the dimensionless quantity

$$\varepsilon = \frac{E}{\Delta\chi} \leq 1. \quad (\text{S41})$$

Eq. (S39) suggests that the transmission probability decreases exponentially as energy decreases and cation radius R_2 increases. Figure S4 shows the simulated value of φ against ε .

Note that φ increases monotonically with the increase of ε .

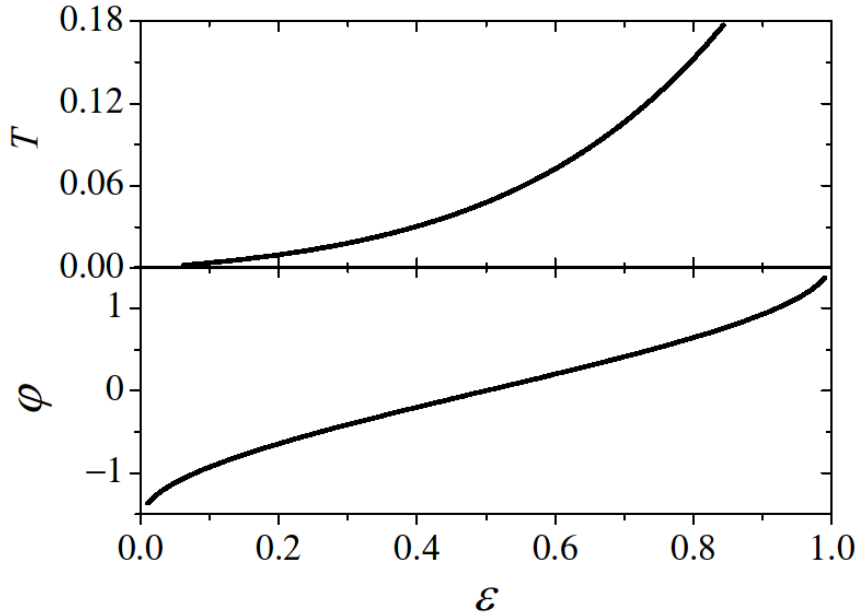


Fig. S4 Simulated transmission probability and transmission phase angle φ changed with ε .

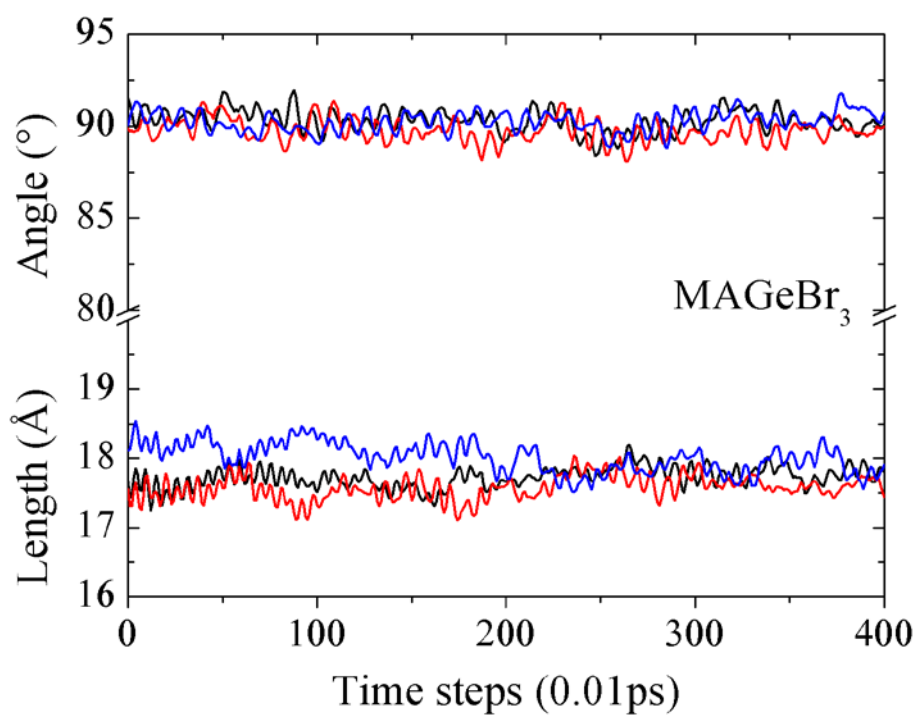
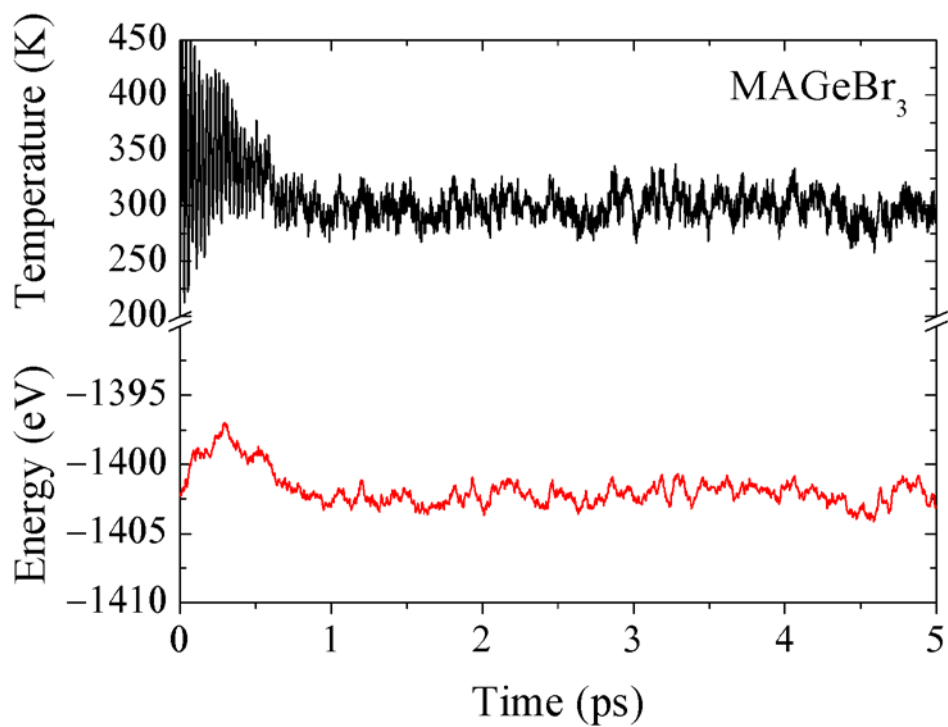
To sum up, the transmission probability T determines the magnitude of the band gaps. The expression for T in Eq. S39 shows that higher bonding ionicity $\Delta\chi$ can result in less transmission probability, hence larger band gap (measured in kL). The transmission phase

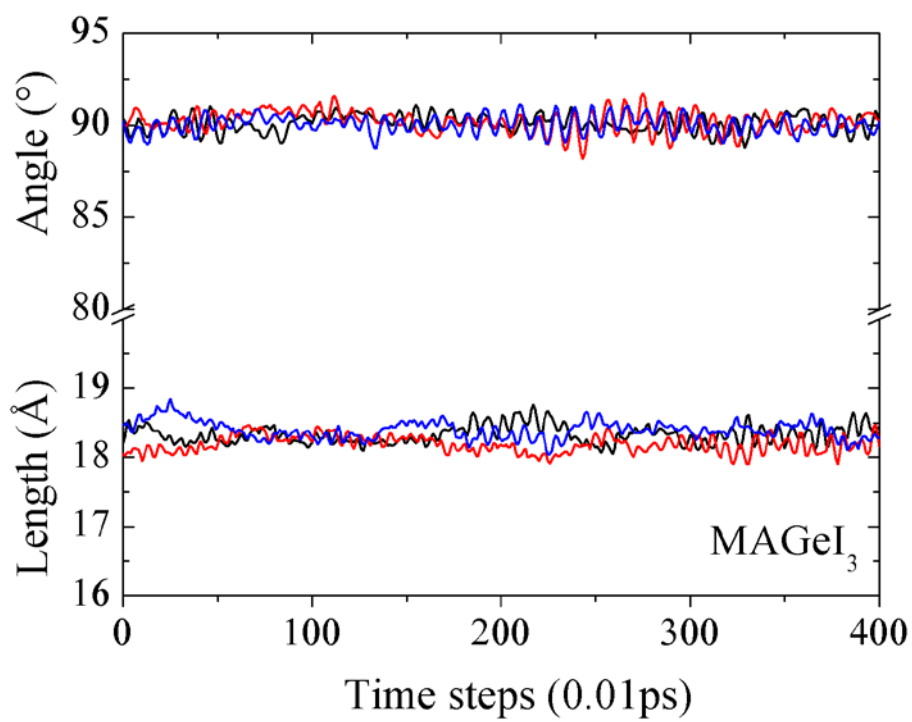
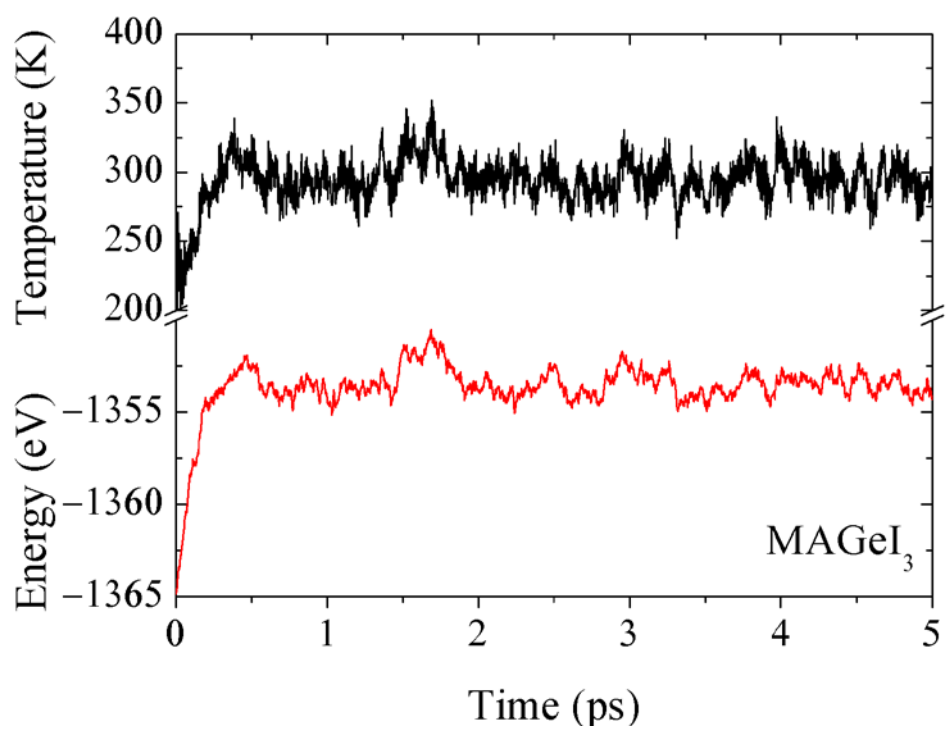
delay φ can determine the position of the band gap through Eq. S23-S24. According to the simulated values as shown in Figure S4, φ will increase monotonically with the ratio between the electron energy and the bonding ionicity $\Delta\chi$. Decreasing the ionicity will increase such ratio, hence φ will also increase. The position of the band gap (in other words, the energy of the maximum of the valence band) will move upwards in energy with the increase (decrease) of φ (ionicity). As the band gap is measured in kL shown in Figure S3, the material with larger lattice size L ($= 2R_+ + 2R_-$ in Fig. S2) will have smaller energy gap.

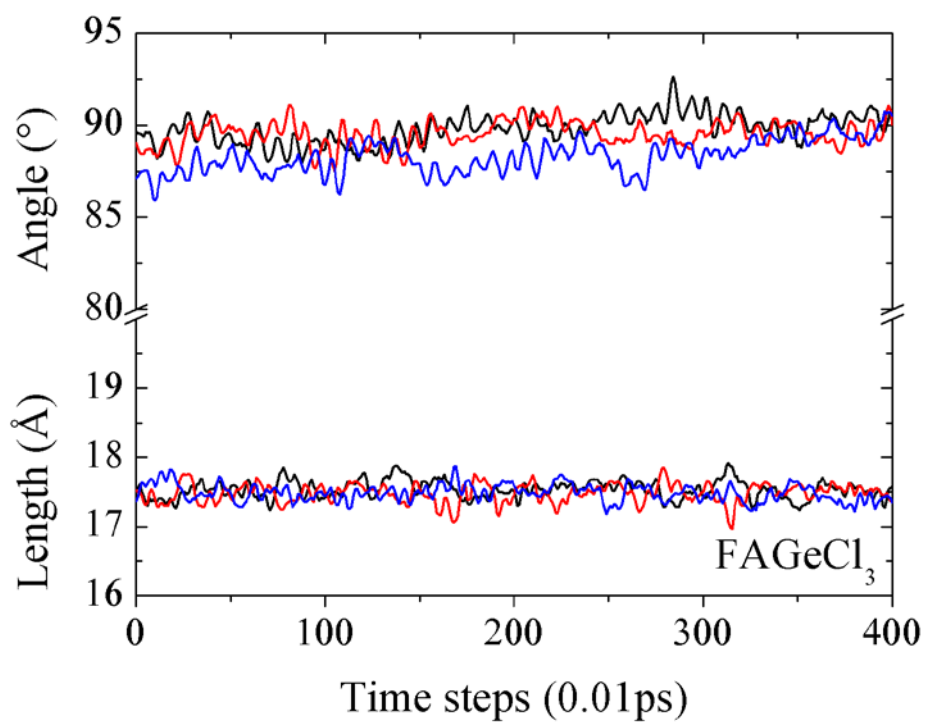
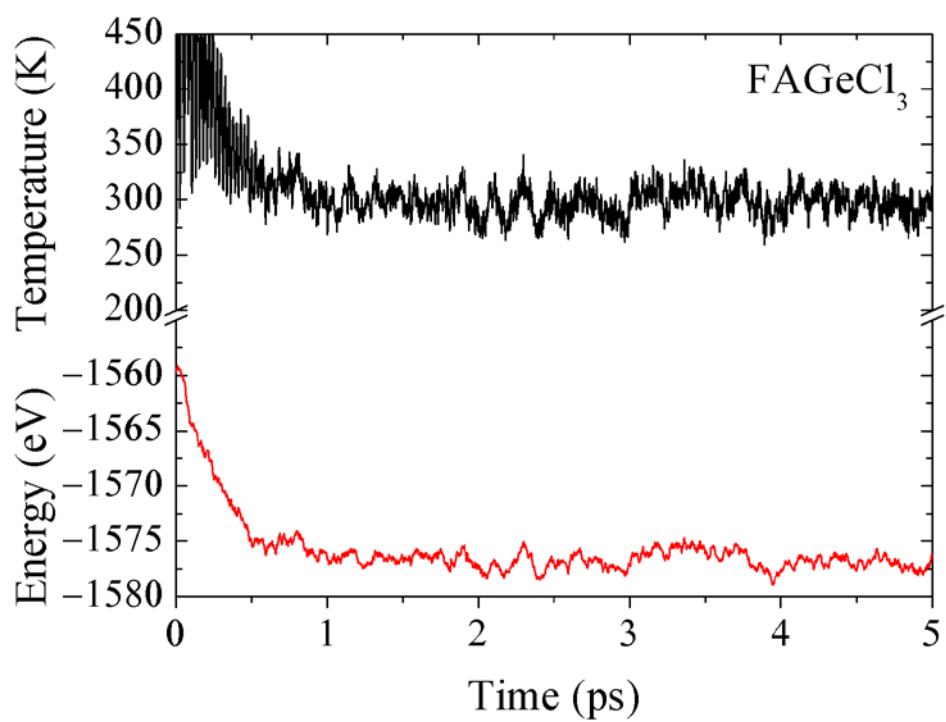
III. Effects of the ionicity $\Delta\chi$ and Coulomb potential V_c on the band gap position

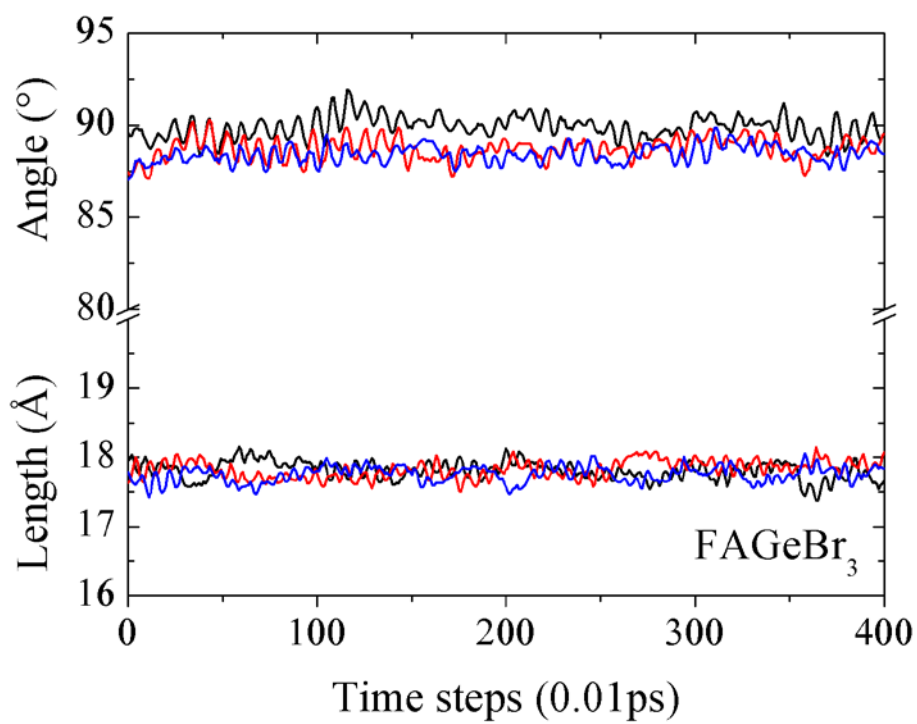
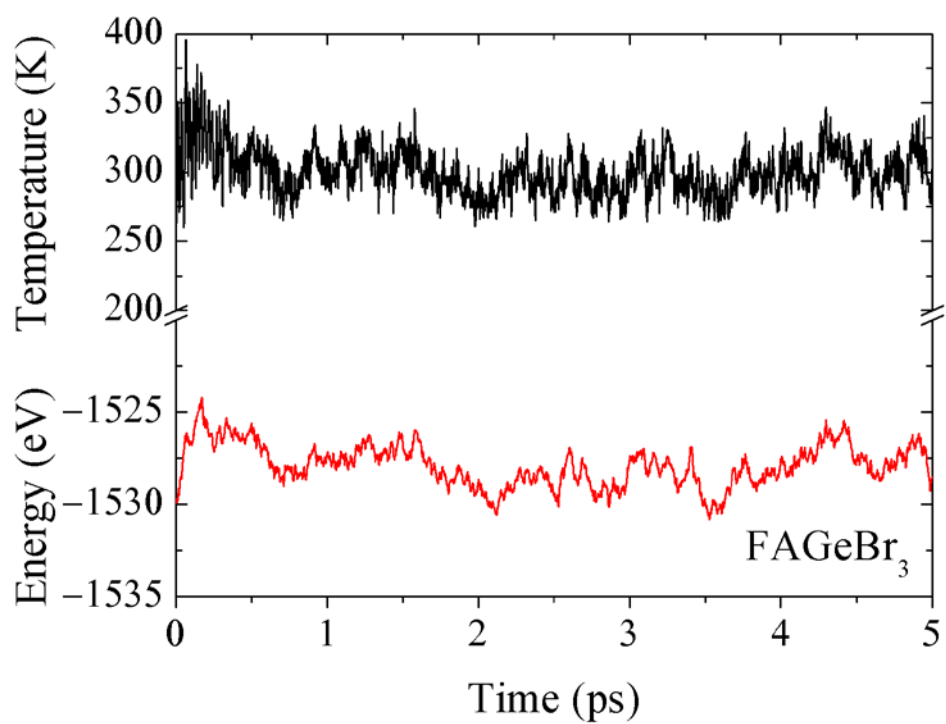
According to the simulated phase delay φ (Eq. S40) in Fig. S4 in the previous section, φ increases with reduced ionicity $\Delta\chi$. Therefore, as stated in the paper, the band gap position (equivalent to the position of the valence band maximum) will move upwards in energy with increasing φ hence decreasing ionicity $\Delta\chi$ according to Eq. S23-S24. Recall that, in our model, we move the whole system up ($V_c + \Delta\chi$) to make $V_1 = 0$ (see Fig. S2). To compare the positions of the maximum of the valence band between different super-alkali halides, we also have to subtract the corresponding ($V_c + \Delta\chi$) from the energy of each material. For materials with lower ionicity, both V_c and $\Delta\chi$ will be smaller compared to that of the more ionic materials, hence will increase the maximum of the valence band further.

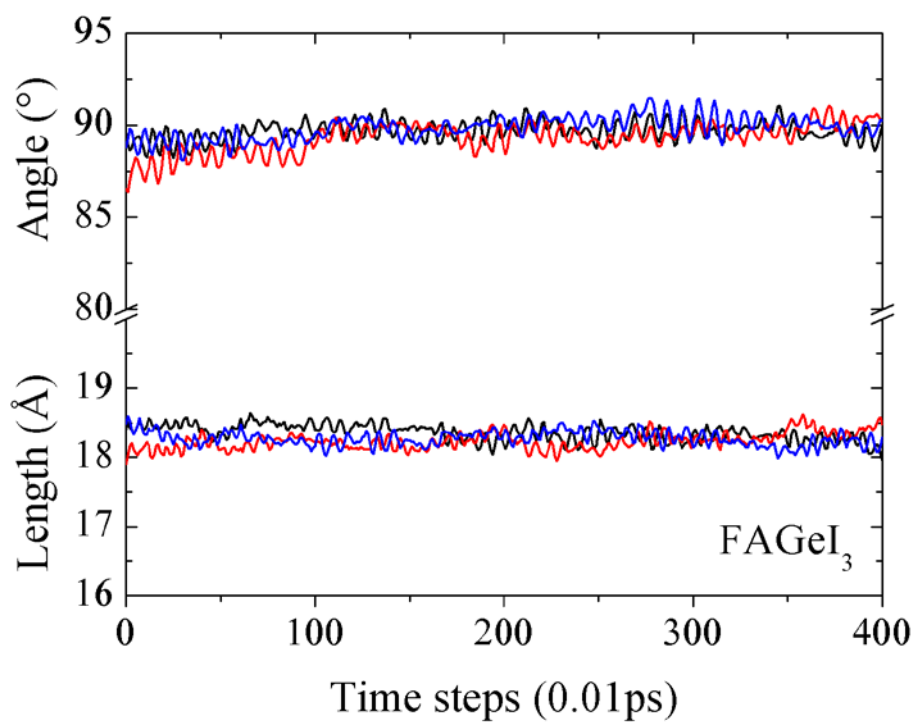
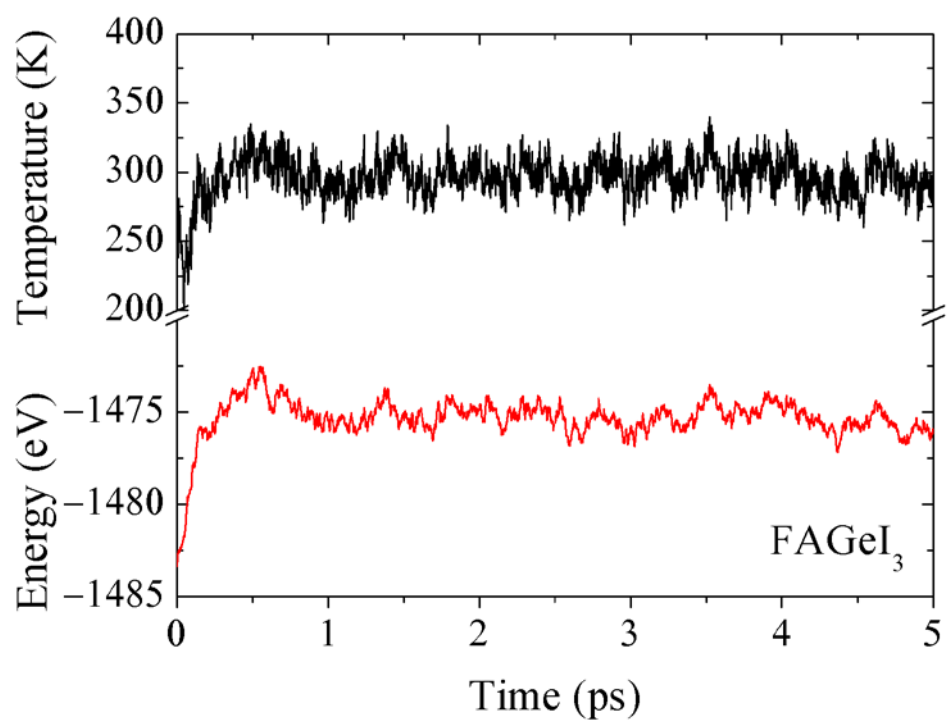
IV. Results of the molecular dynamics simulations

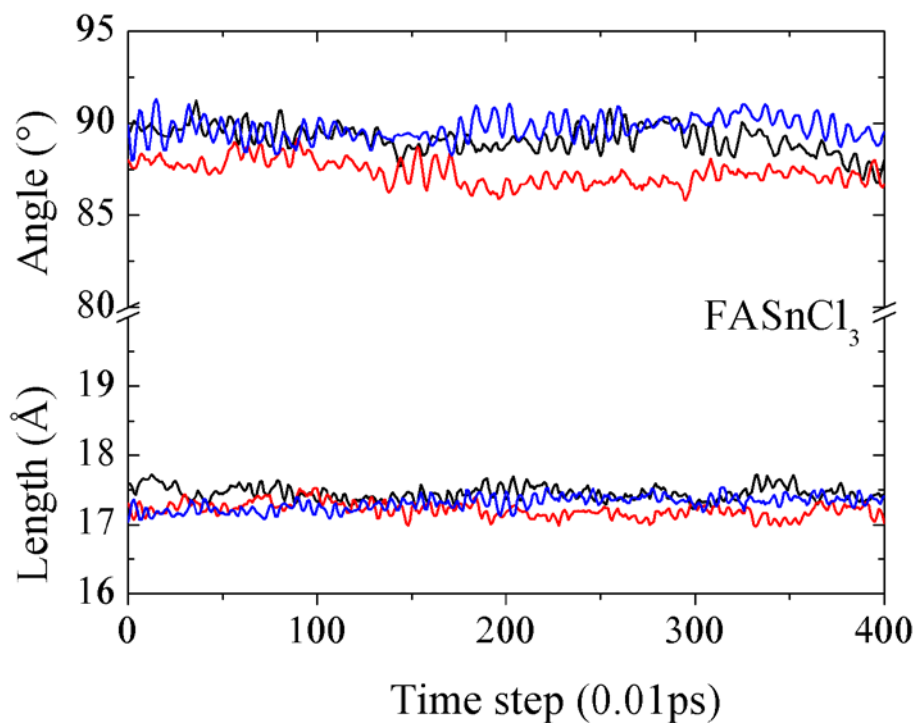
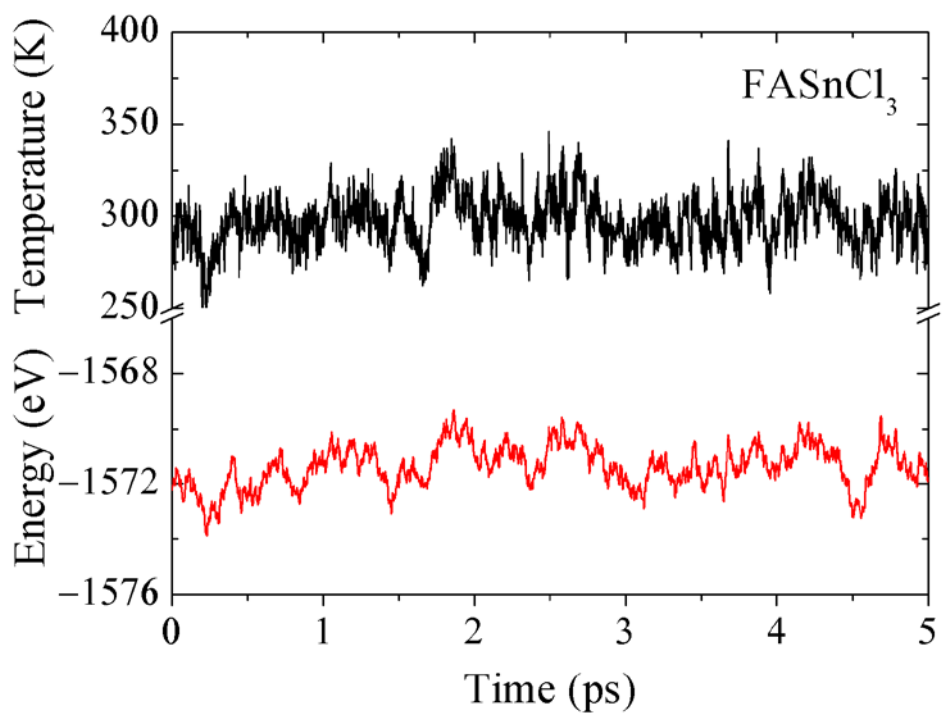


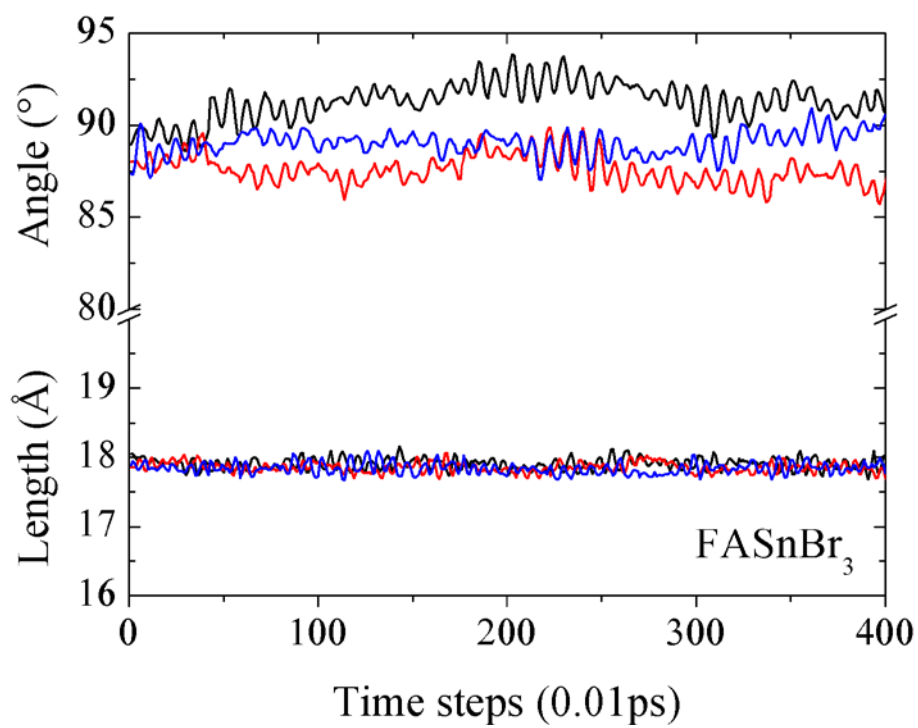
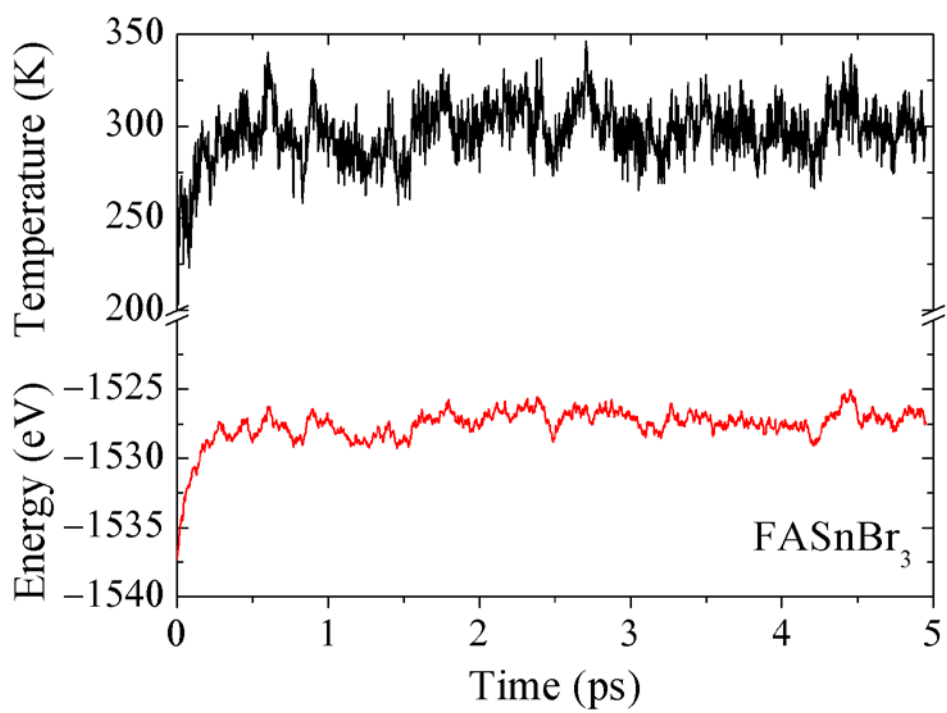


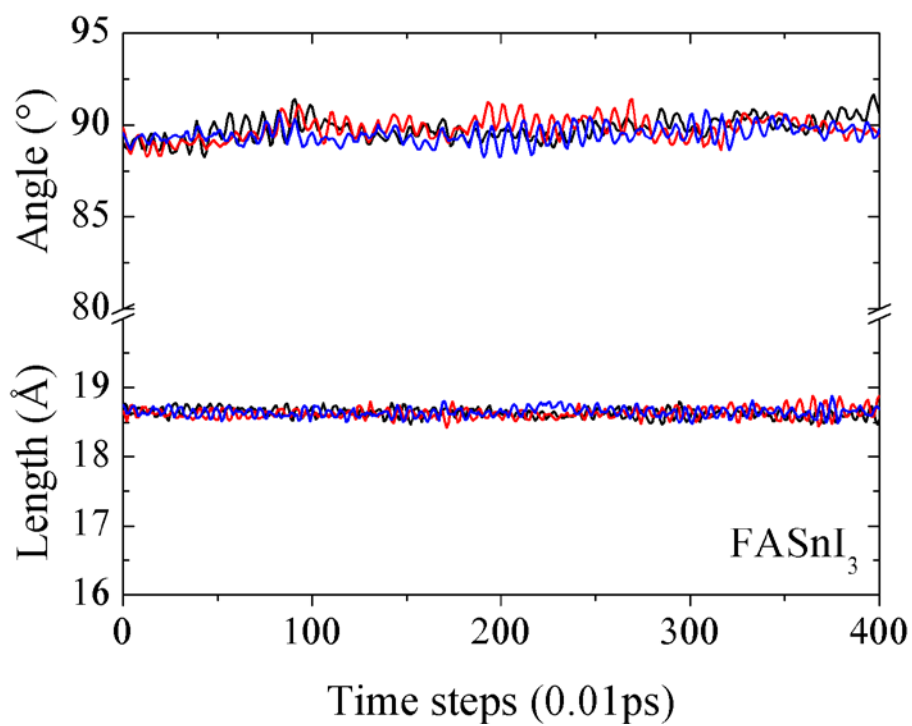
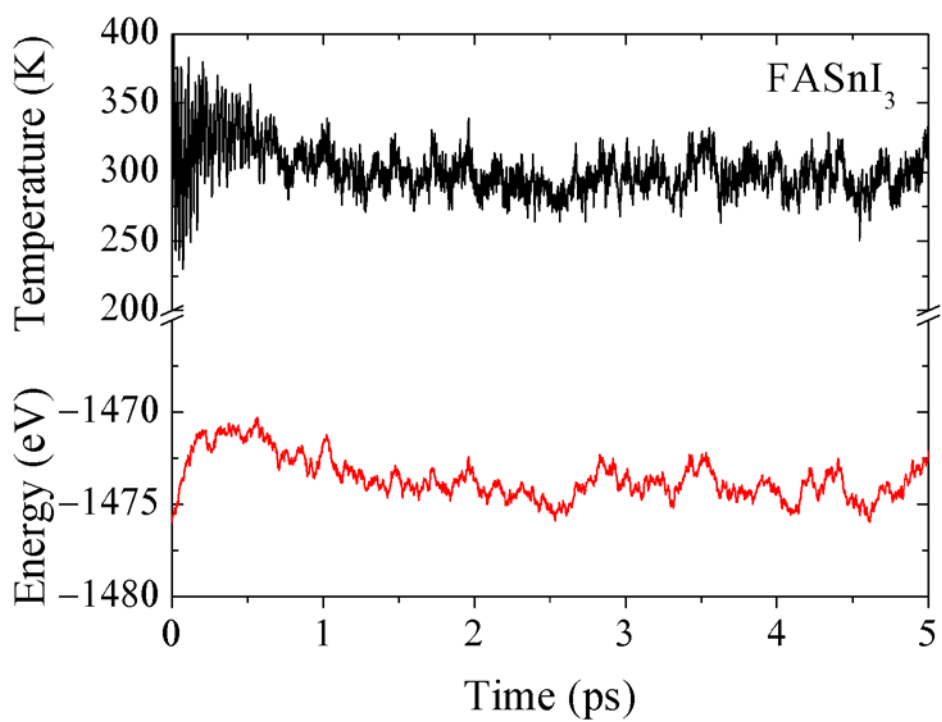


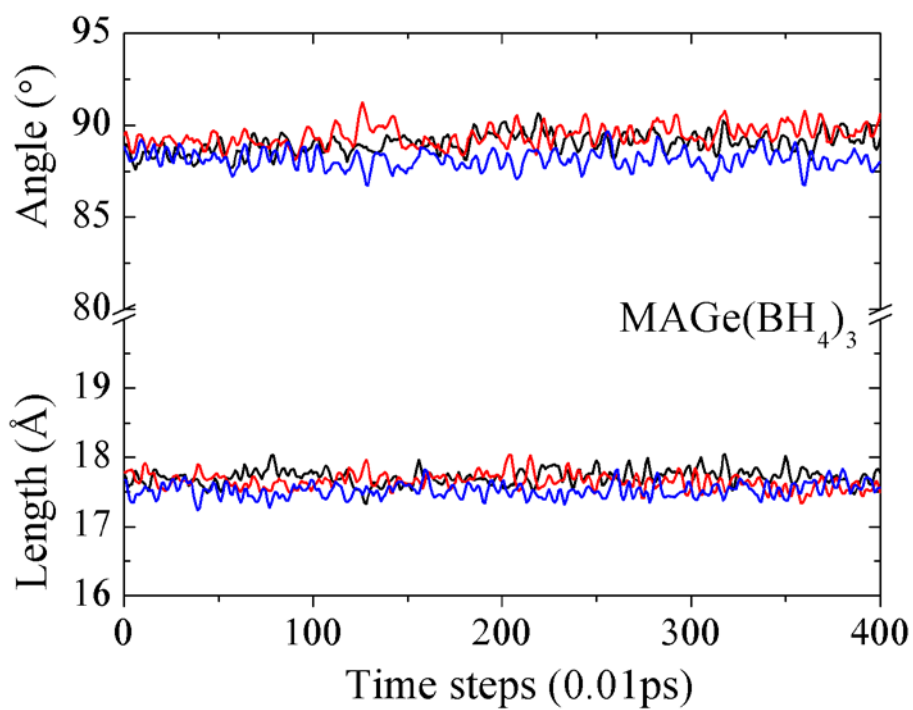
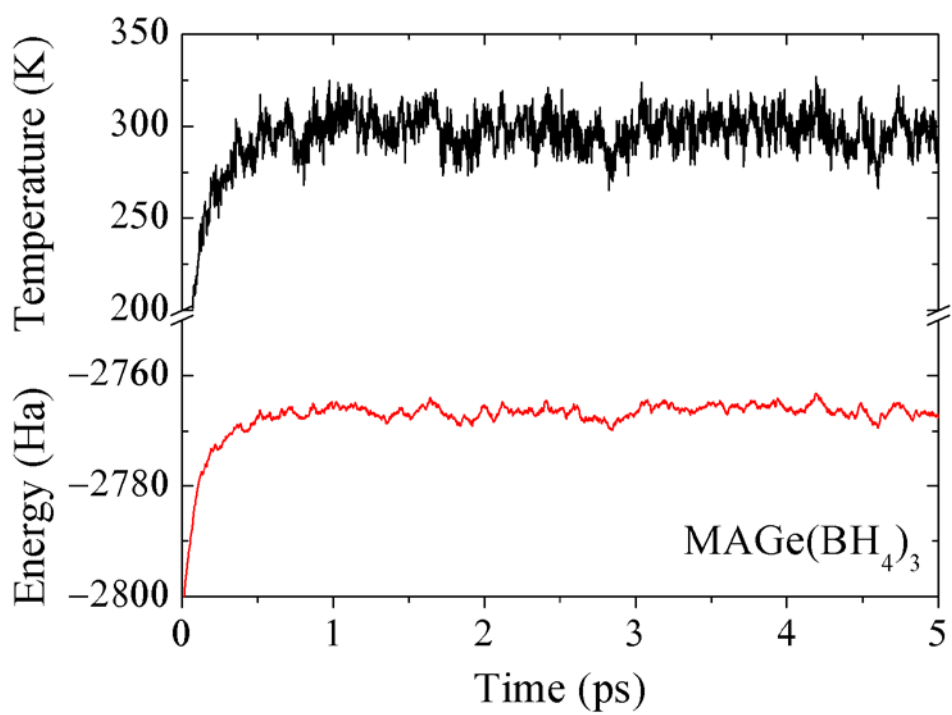


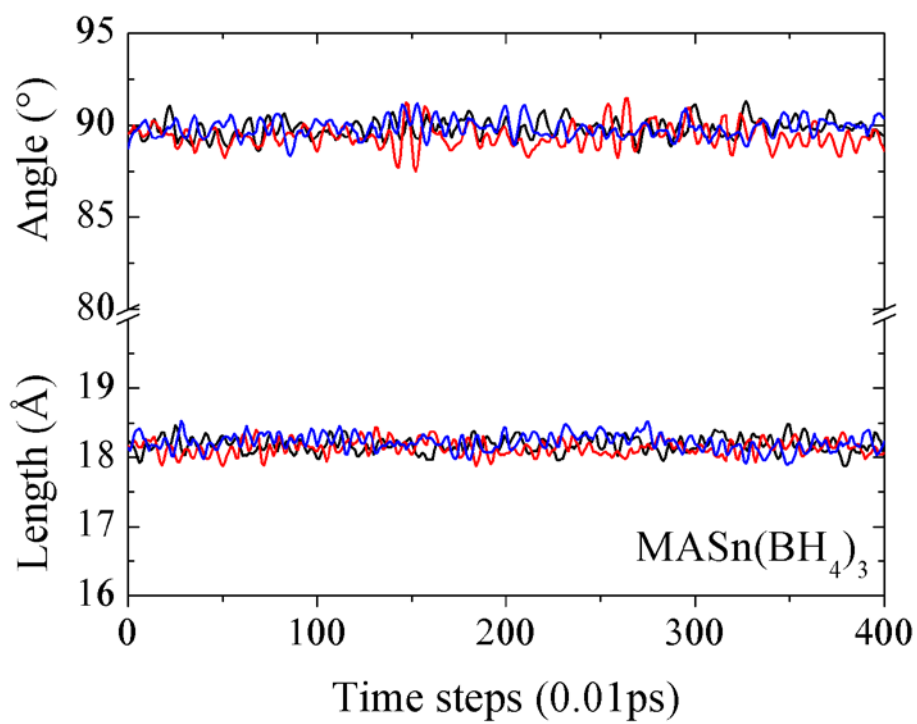
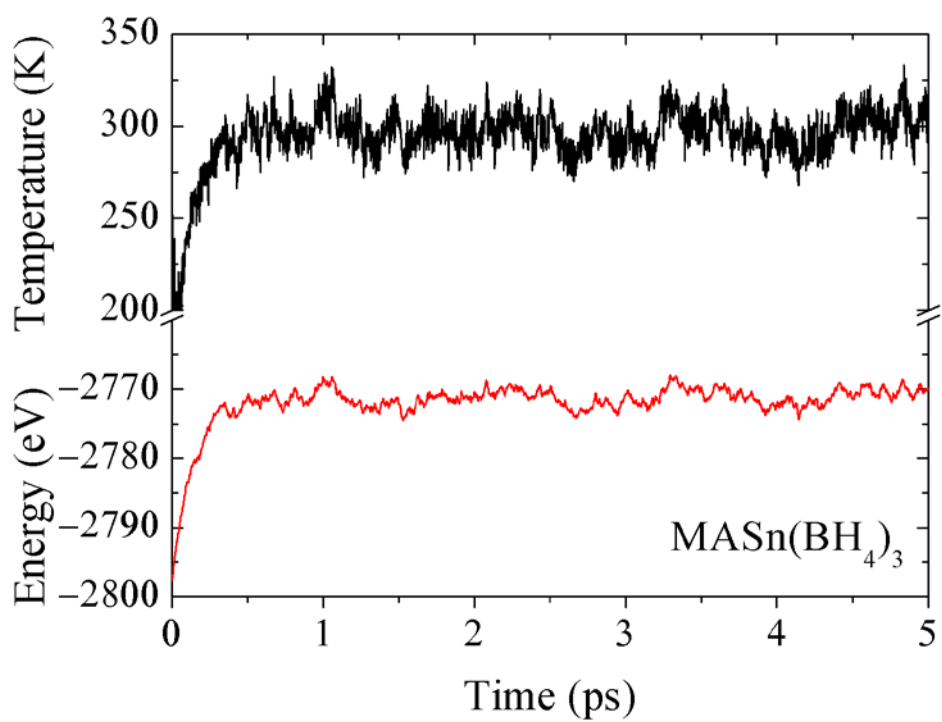


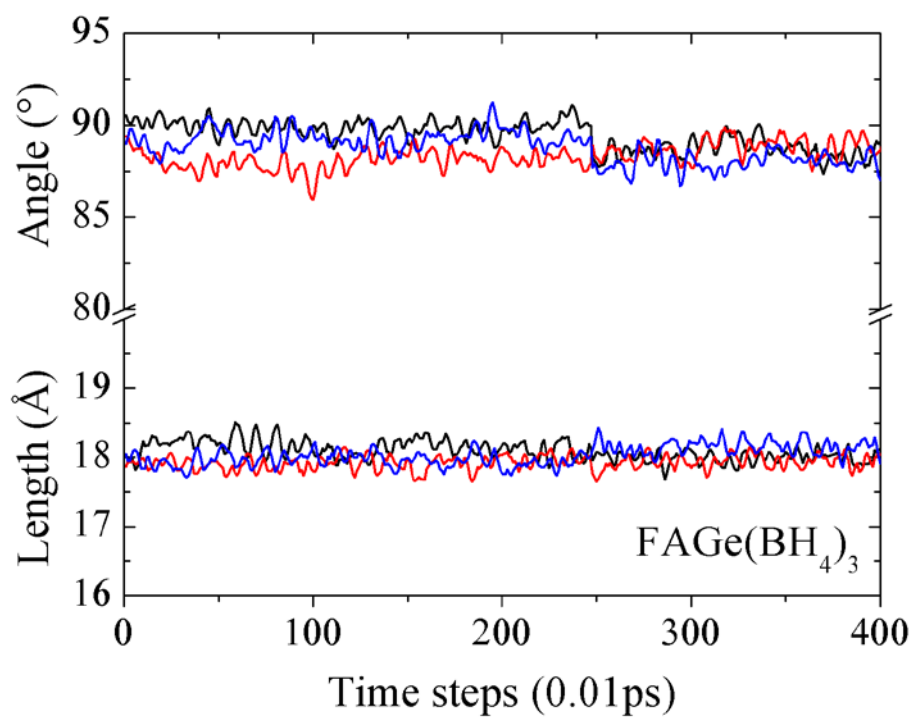
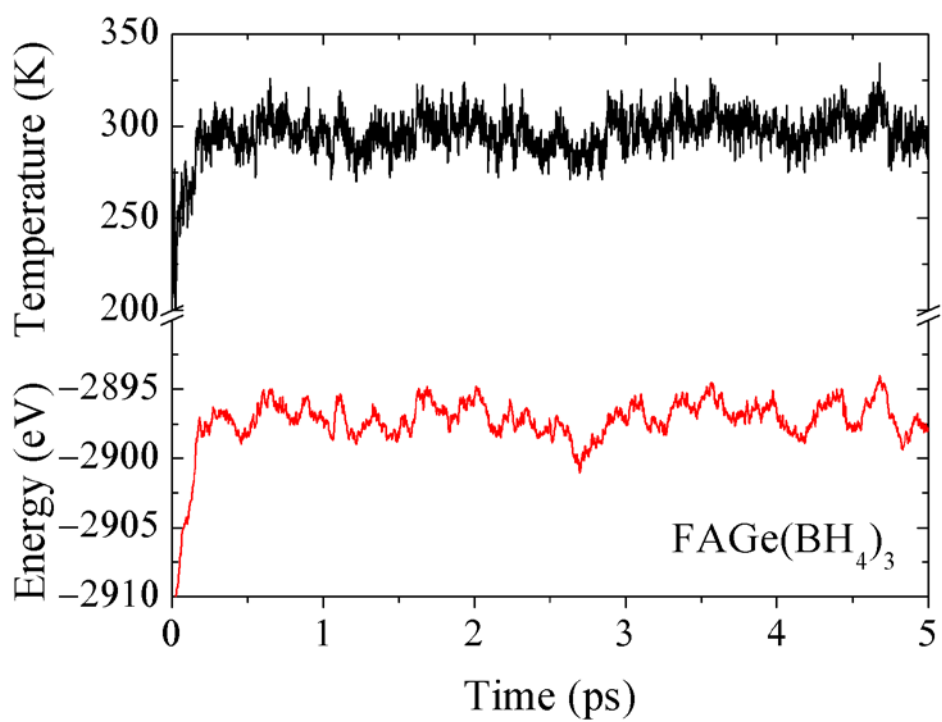


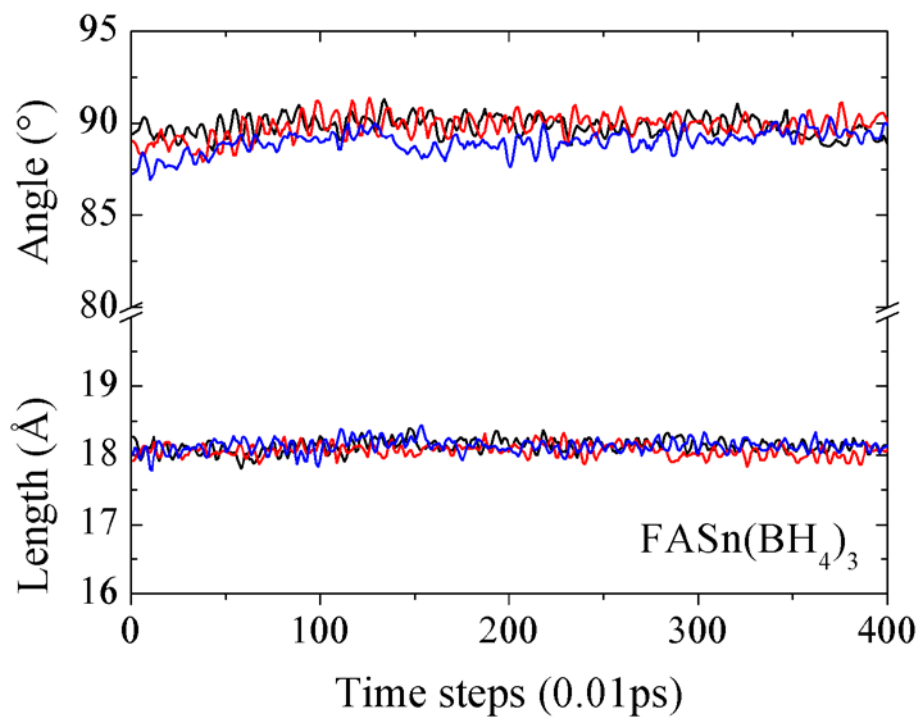
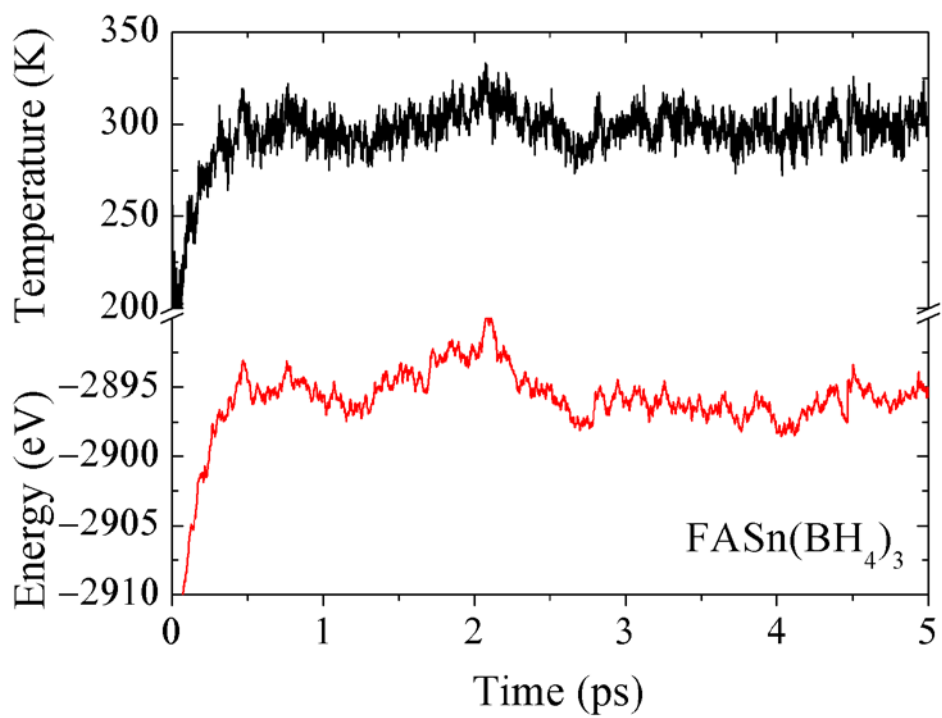


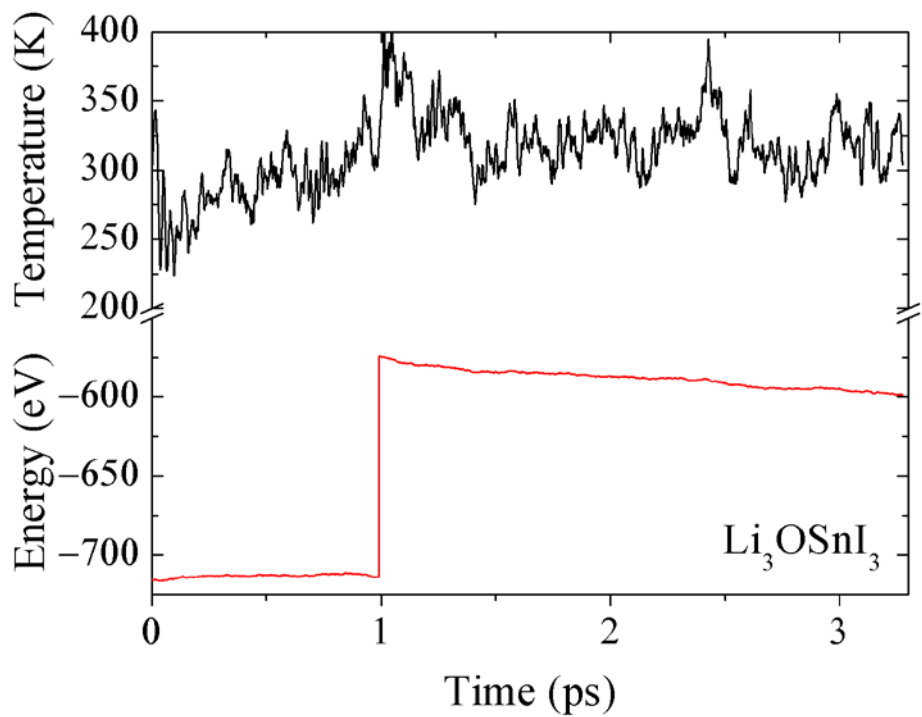
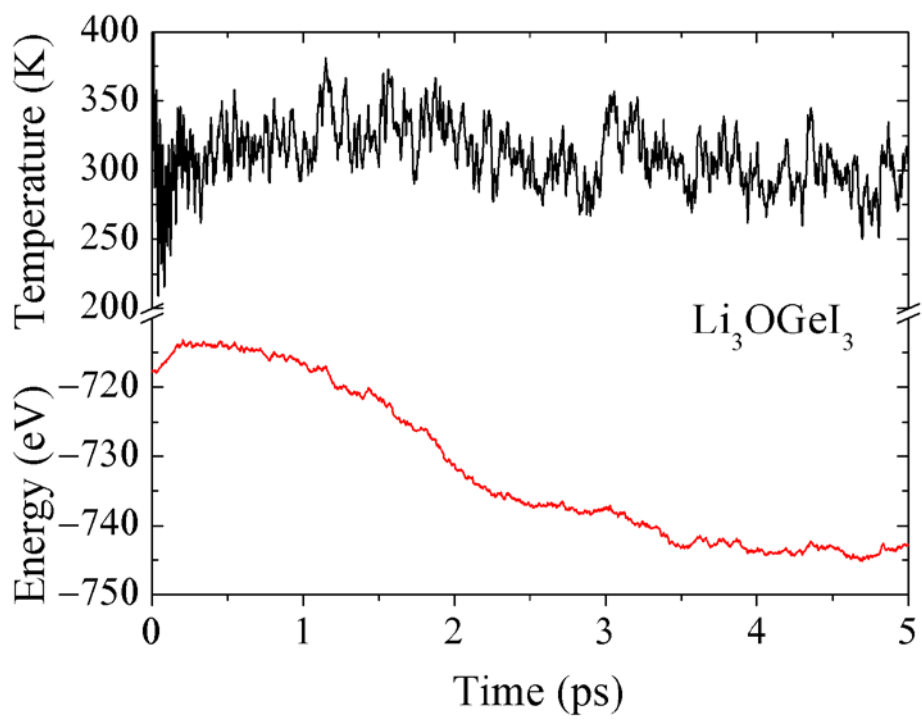












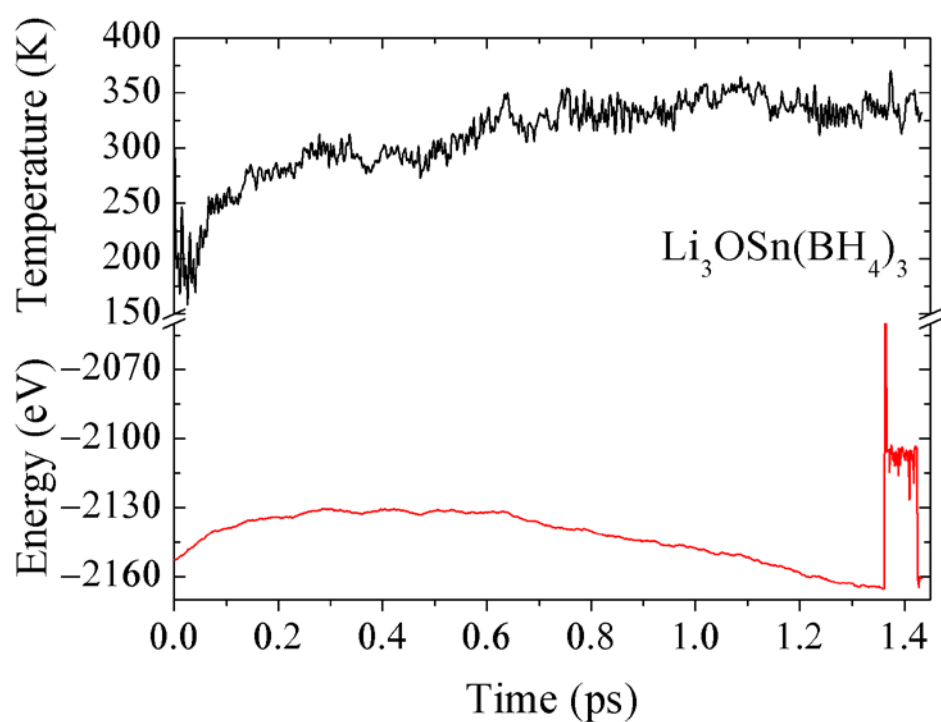
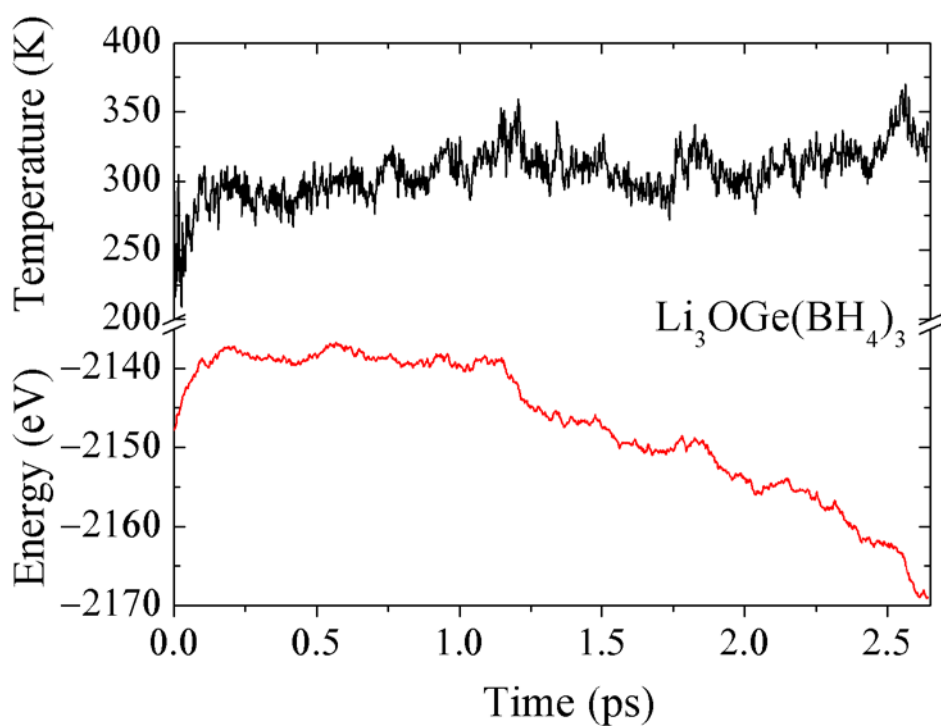


Fig. S5 Free energy and temperature from the molecular dynamics simulations under ambient conditions calculated using $3 \times 3 \times 3$ supercells in the NpT ensemble. The lattice parameters are simulated for 4 ps after the energy and temperature reach equilibrium.

V. Simulated X-ray diffraction pattern

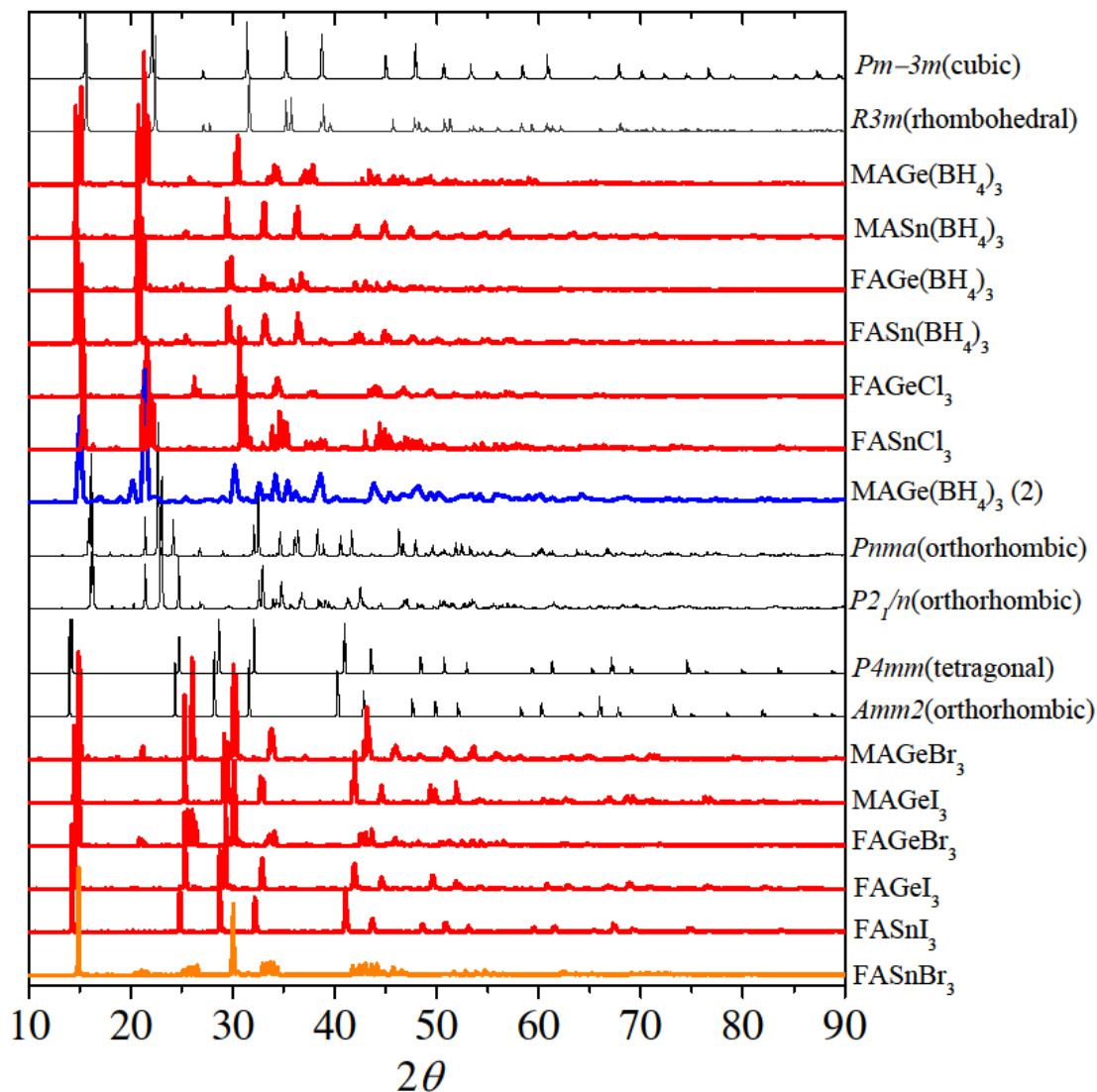


Fig. S6 Simulated X-ray diffraction (XRD) patterns (in red) for the averaged configurations obtained from the molecular dynamics simulations of hybrid perovskites under ambient conditions. These are compared to the XRD patterns (in black) of crystal phases that are usually seen in the hybrid perovskites. The blue line is the pattern of $\text{MAGe}(\text{BH}_4)_3$ after equilibrium starting from a $3 \times 3 \times 2$ supercell with $Pnma$ (orthorhombic) unit cell. This is to show that the crystal structure of the material indeed tends to be stable at a rhombohedral or cubic structure under the simulated ambient condition, as shown by the three peaks around 20° that start to merge into one peak and the many peaks between $30^\circ \sim 40^\circ$ that start to merge into three major peaks. The orange pattern of FASnBr_3 is not any one of the experimental patterns given in the plot and we impose a tetragonal lattice to the material in the study.

VI. Effective ionic radii of the super ions

According to our model discussed in section II and III, the band gap of super alkali halides is dependent on the bonding ionicity and the ionic radii of the cation and anion. For elements in the periodic table, different methods for ionic radii have been developed. One direct method is to measure the bond lengths of binary materials using diffraction techniques. Then, by using the oxygen radius as a reference, a set of radii can be defined for all the other elements in the periodic table.

A less direct method to define the effective ionic radius of an ion is to use the relationship between the polarizability and the radius of a spherical electron cloud. The relationship is

$$\alpha = 4\pi\epsilon_0 R^3, \quad (\text{S43})$$

where α is the electric polarizability calculated from the dipole moment arising from the movement of a spherical electron cloud off-center compared to the positive charge center. R is defined as the ionic radius. According to the Lorentz equation, the volume associated with the polarizability of a *molecule* is expressed as,

$$\alpha_m = \frac{1}{4\pi\epsilon_0} \sum_i \alpha_i = V_m \frac{n^2 - 1}{l(n^2 - 1) + 4\pi}, \quad (\text{S44})$$

where α_i is the polarizability of the i th ion in the molecule as defined in Eq. (S43). V_m is the volume of the crystal divided by the number of molecules in the crystal. n is the refractive index and l is the Lorentz factor. For ideal ionic structures like the alkali halides with the local field included, $l = 4\pi/3$. Without considering the local field, the system is like an electron gas where $l = 0$. For a binary ionic crystal, according to Eq. (S44), we can write

$$R_h^3 + R_a^3 = V_m \frac{\epsilon - 1}{l(\epsilon - 1) + 4\pi}, \quad (\text{S45})$$

where we have used the relationship between the dielectric constant of the material refractive index $\epsilon = n^2$. R_h and R_a are the defined as the ionic radii of the halogen and the alkali, respectively. Combined with the bond length equation, as in our model,

$$R_h + R_a = \frac{L}{2} \quad (\text{S46})$$

the two ionic radii can be readily solved.

It is possible for us to define the ionic radius of a super-ion by using the same method. For each super-ion with a given geometry, we can define an effective ionic radius by mapping the super-ion to a spherical ion that has the same polarizability,

$$\alpha_{\text{sh}} + \alpha_{\text{sa}} = \alpha_{\text{sh}}^{\text{eff}} + \alpha_{\text{sa}}^{\text{eff}} = R_{\text{sh}}^3 + R_{\text{sa}}^3 = V_{\text{m}} \frac{\varepsilon - 1}{l(\varepsilon - 1) + 4\pi}. \quad (\text{S47})$$

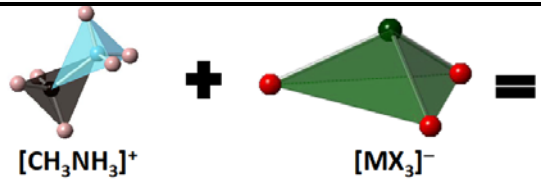
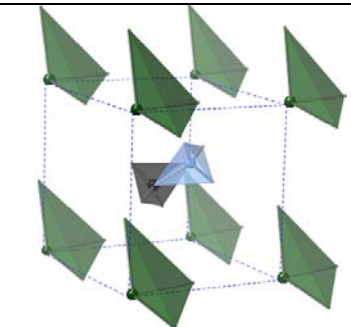
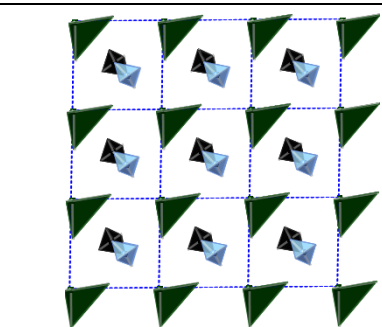
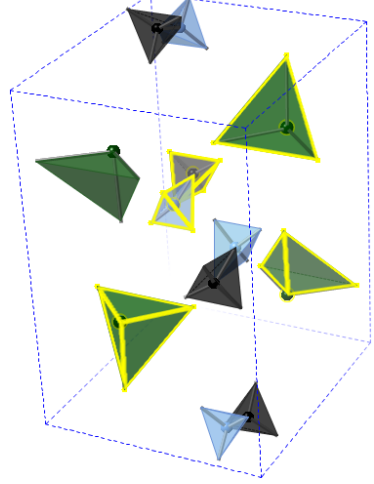
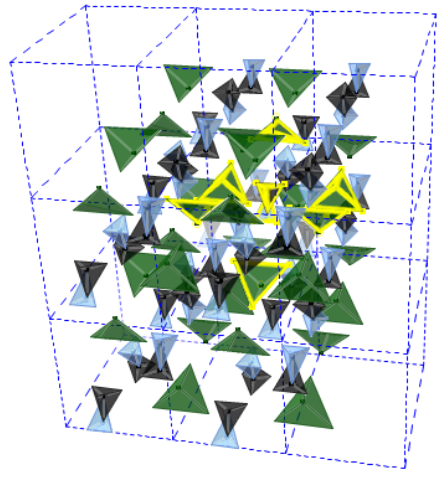
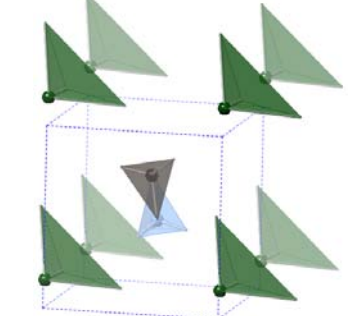
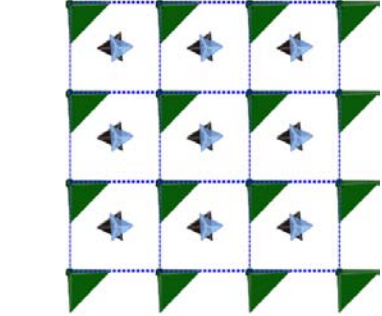
The dielectric constant ε can be measured or computed for the super alkali halides.

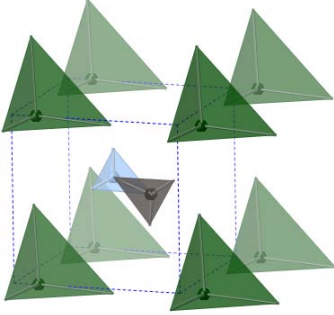
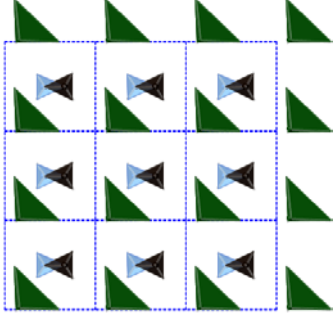
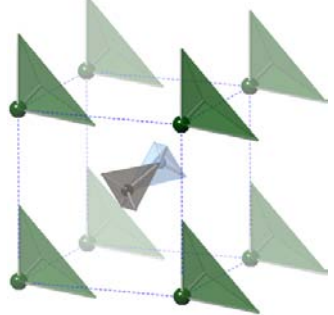
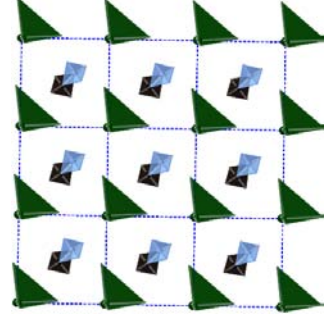
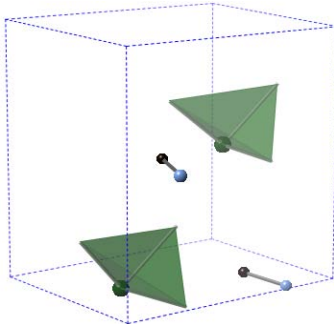
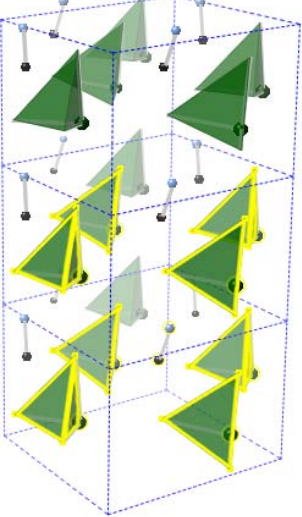
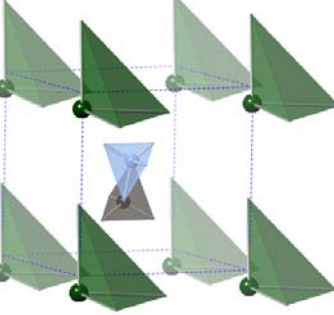
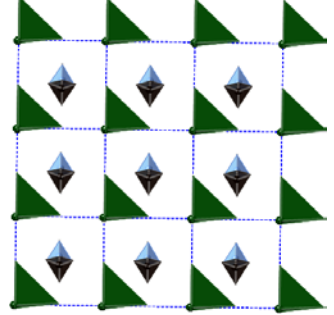
Here, we define the effective ionic radius of a super-ion for the first time. Not only because we can use the radius in the model, more importantly, knowing the radii of the super-ions would be very helpful for the analysis of structural stability of materials composed of super-ions, as already seen in alkali halide crystals where the physical properties are by in large decided by the ratio of the cation and the anion radius (Pauling's rules).

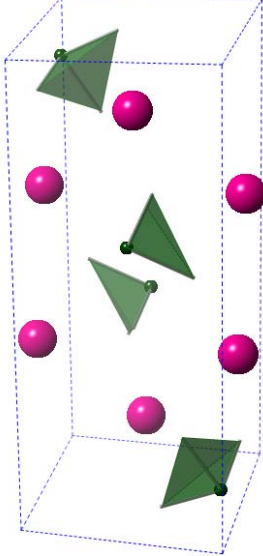
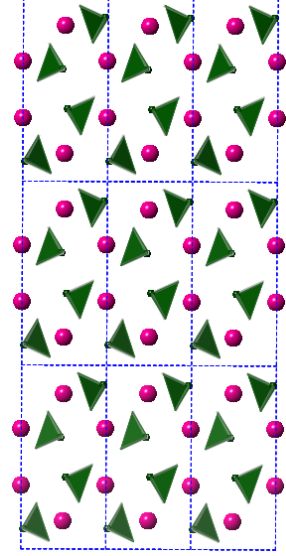
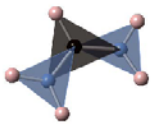
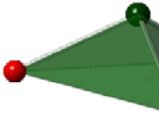
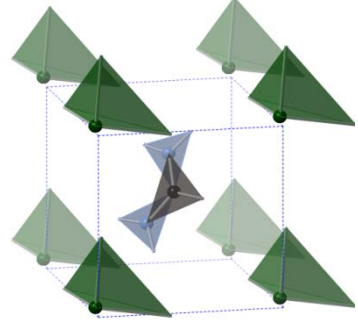
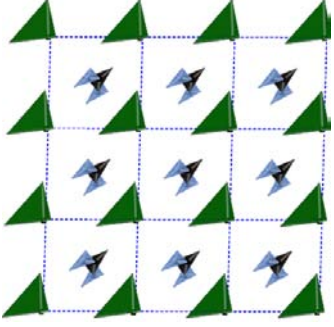
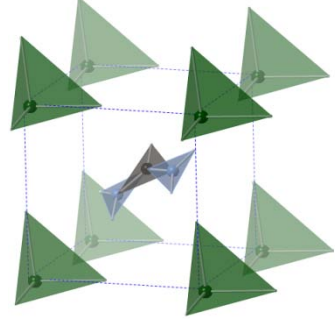
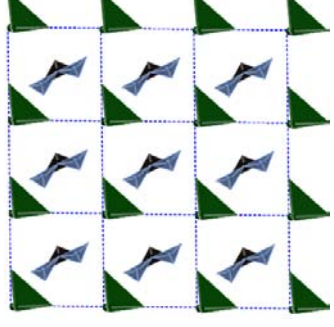
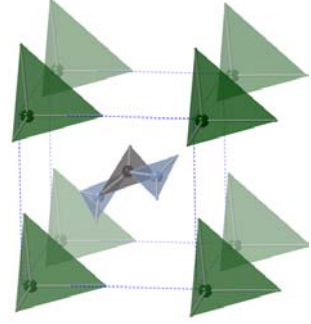
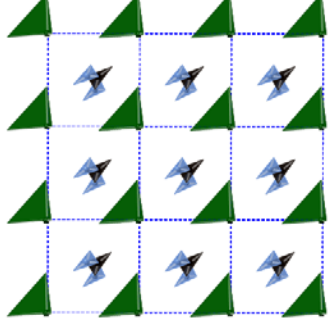
Unlike the regular ions, the super-alkalis and super-halogens are themselves atomic clusters, hence have their own geometry with internal degrees of freedom. Although the chemical formula suggests that $[\text{MA or FA}]^+ : [\text{MX}_3]^-$ ($\text{M} = \text{Ge, Sn}; \text{X} = \text{Cl, Br, I, BH}_4$) must equal to 1 : 1 in the material composition, in order to define their ionic radii, the cations $[\text{MA}]^+$ and $[\text{FA}]^+$ as well as the anions $[\text{MX}_3]^-$ should appear explicitly in the materials. A direct demonstration is to show that their geometrical structures change little across different materials.

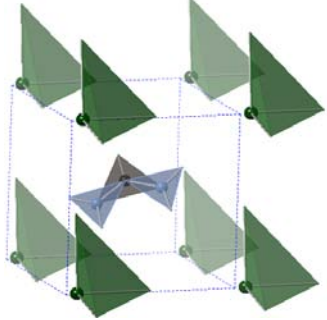
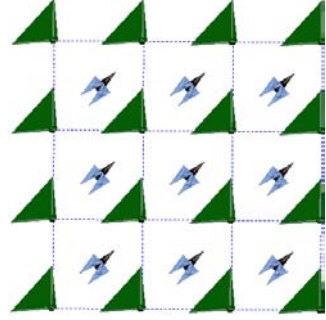
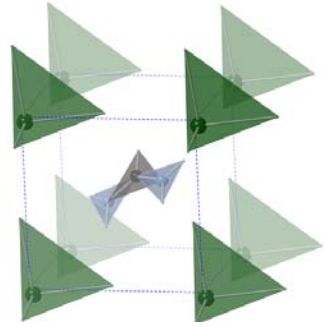
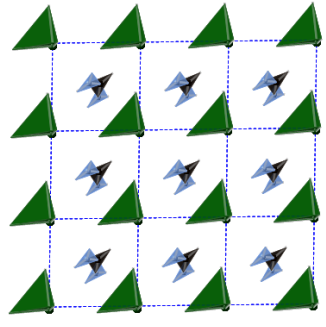
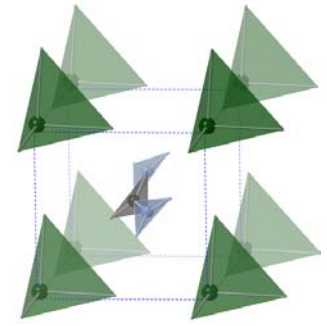
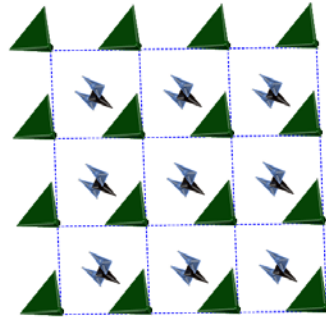
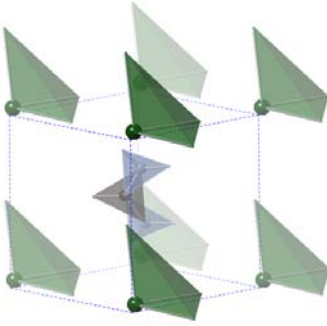
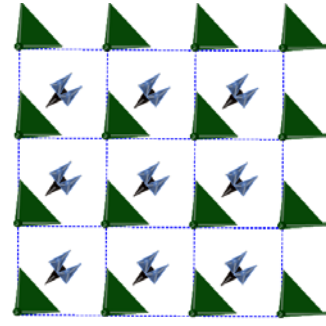
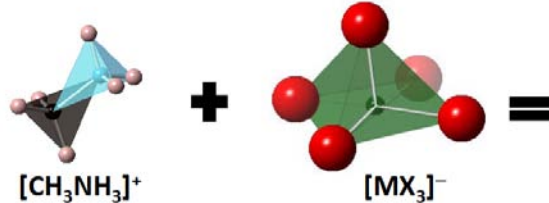
Table S3 lists the unit cells and the super cells of all the studied super alkali halides under ambient condition by using either simulated or experimental data. Figure S6 shows the simulated X-ray diffraction patterns of the averaged configurations calculated from the molecular dynamics simulations under the ambient condition (Figure S5). The cation MA^+ adopts a polyhedral shape consisting of CH_3 and NH_3 pyramids embedded opposite to each other. FA^+ adopts a planar shape consisting of a CH_3 triangle between two NH_3 triangles. The anions $[\text{GeCl}_3]^-$, $[\text{GeBr}_3]^-$, $[\text{GeI}_3]^-$, $[\text{Ge}(\text{BH}_4)_3]^-$ and $[\text{SnCl}_3]^-$ are pyramids with the metal atom at the peak. The anions $[\text{SnBr}_3]^-$ and $[\text{SnI}_3]^-$, on the other hand, tend to be square pyramids with the metal atom at the center of the bottom square.

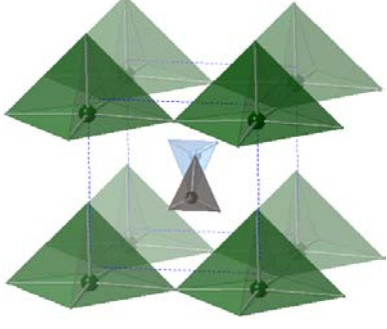
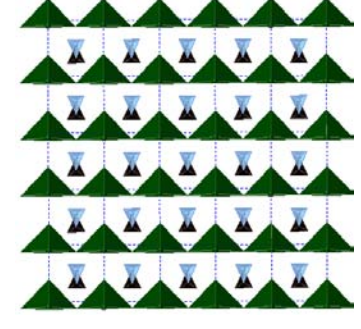
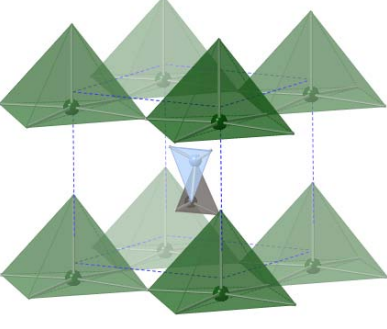
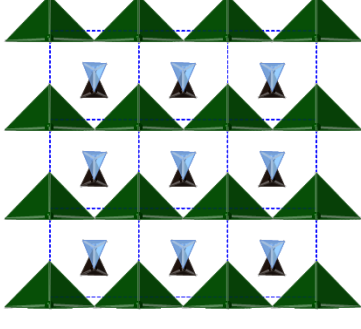
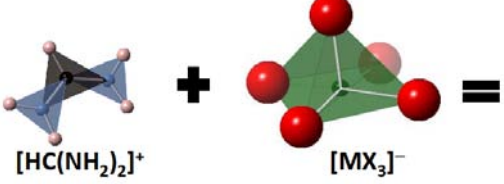
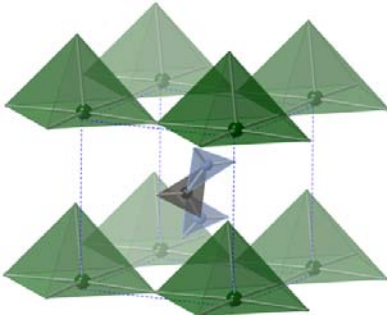
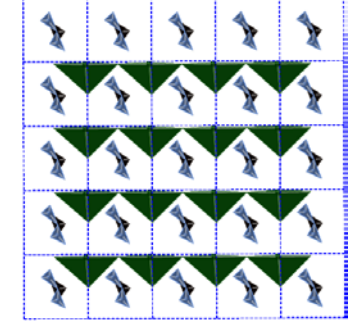
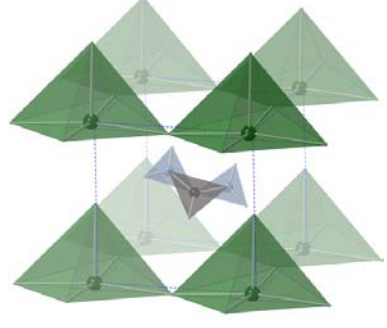
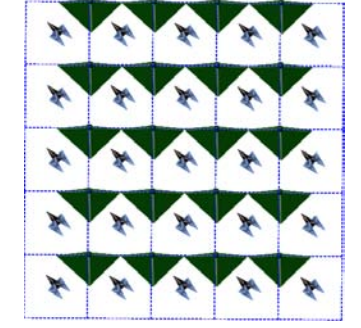
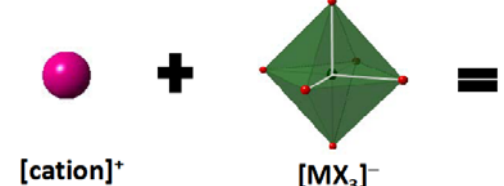
TABLE S3. Experimental or simulated crystal structures of the studied hybrid perovskites under ambient conditions. For the simulated structures, the crystal system and the lattice parameters are obtained from molecular dynamic simulations using the NpT ensemble (Figure S5) and the simulated X-ray diffraction patterns of the averaged configurations (Figure S6). The positions of ions in the unit cell were then relaxed with fixed lattice parameters. It was found that $[\text{SnBr}_3]^-$ can be grouped both as a pyramid and as a square pyramid in the MASnBr_3 crystal with cutoff radii of 2.925 and 2.956 Å, respectively. The same was observed for the FASnBr_3 crystal, where the two cutoff radii are 2.954 and 3.104 Å, respectively. The last row shows the cubic phase that all the hybrid perovskites tend to have at high temperatures. The cation in such a case is represented by a dummy atom. The highlighted (in yellow) super ions show that the materials have 6 or 8 coordination number, as normally seen in the alkali halide structures.

		
Crystal	Unit Cell	Supercell
$\text{MAGe}(\text{BH}_4)_3$ Rhombohedral		
MAGeCl_3 Orthorhombic		
MAGeBr_3 Tetragonal		

<p>MAGeI₃ Tetragonal</p>		
<p>MASn(BH₄)₃ Rhombohedral</p>		
<p>MASnCl₃ Monoclinic</p>		
<p>MASnBr₃ Tetragonal</p>		

<p>CsSnCl₃(RT) Monoclinic</p>		
<div style="display: flex; align-items: center; justify-content: center;">  +  = </div> <div style="display: flex; justify-content: space-around; margin-top: 5px;"> $[HC(NH_2)_2]^+$ $[MX_3]^-$ </div>		
<p>Crystal</p>	<p>Unit Cell</p>	<p>Supercell</p>
<p>FAGe(BH₄)₃ Rhombohedral</p>		
<p>FAGeCl₃ Rhomboneal</p>		
<p>FAGeBr₃ Tetragonal</p>		

<p>FAGeI₃ Tetragonal</p>		
<p>FASn(BH₄)₃ Rhombohedral</p>		
<p>FASnCl₃ Rhombohedral</p>		
<p>FASnBr₃ Tetragonal</p>		
 <p>[CH₃NH₃]⁺ + [MX₃]⁻ =</p>		
<p>Crystal</p>	<p>Unit Cell</p>	<p>Supercell</p>

<p>MASnBr₃</p>		
<p>MASnI₃</p>		
 <p style="text-align: center;"> $[\text{HC}(\text{NH}_2)_2]^+$ $[\text{MX}_3]^-$ </p>		
<p>Crystal</p>	<p>Unit Cell</p>	<p>Supercell</p>
<p>FASnBr₃ Tetragonal</p>		
<p>FASnI₃ Tetragonal</p>		
 <p style="text-align: center;"> $[\text{cation}]^+$ $[\text{MX}_3]^-$ </p>		

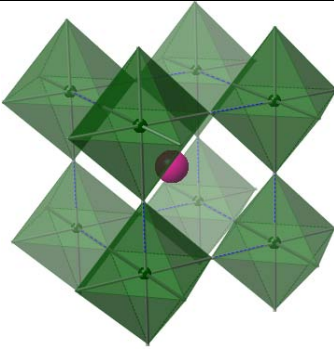
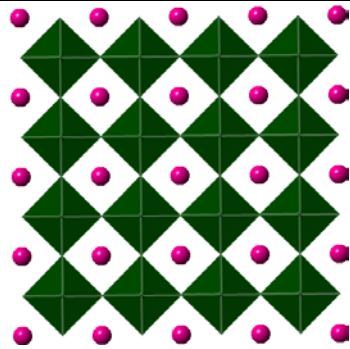
Crystal	Unit Cell	Supercell
High-temperature cubic phase		

Table S4 shows the geometrical data of the above mentioned super-alkalis and super-halogens. For the super-alkalis, it is clear that their structures almost remain the same in different materials and hardly change from that of its isolated cluster geometry. We use the same color to represent the structural data of the same super halogen in different materials, which shows very little change between different materials. A typical relative difference in both the distance and the angle data between the structures in vacuum and in the crystal field is smaller than 5%. For hyper halogens $[\text{Ge}(\text{BH}_4)_3]^-$ and $[\text{Sn}(\text{BH}_4)_3]^-$, the relative difference between the ions in the crystals and the isolated cluster is within 7% in X-X distances and about 18% in M-X-X angles.

TABLE S4. Experimental and simulated parameters of the studied super-alkalis and super-halogens as isolated clusters and in the studied hybrid perovskites under ambient conditions. ‘Bh’ stands for [BH₄] and the B-H bond length is always between 1.2 and 1.3 Å. CsGeCl₃, CsGeBr₃ and CsGeI₃ show the rhombohedral phase (*R3m*) at the room temperature. Their lattice parameters are 5.43, 5.64 and 5.98 Å, respectively. RbGeBr₃, on the other hand, shows an orthorhombic phase at room temperature (*Pn2₁a*). For the super-alkalis, the data include the C-N distance, the C-H distance, the N-H distance, the N-C-H angle and the C-N-H angle. For the super-halogens, the data include the metal-halogen (M-X) distance, the nearest halogen-halogen (X-X) distance, the halogen-metal-halogen (X-M-X) angle, the angle of metal-halogen-halogen (M-X-X) with the neighboring halogens and the long metal-halogen (M---X) bond(s) that are grouped out of the (square) pyramids. For comparison, data involve the same super-halogens are put in the same color.

Super Ion	C-N (Å)	C-H (Å)	N-H (Å)	N-C-H (°)	C-N-H (°)	M-X (Å)	X-X (Å)	X-M-X (°)	M-X-X (°)	M---X (Å)
MA ⁺	1.52	1.09	1.03	108.26	111.50	-	-	-	-	-
[GeCl ₃] ⁻	-	-	-	-	-	2.36	3.60~ 3.61	99.30~ 99.40	40.24~ 40.38	-
MAGeCl ₃ ^a	1.50	1.07	1.02	107.16	113.07	2.32~ 2.34	3.42~ 3.43	94.23~ 95.57	42.22~ 43.17	3.28~ 3.29
CsGeCl ₃ ^c	-	-	-	-	-	2.35	3.44	94.16	42.92	3.09
[Ge(Bh) ₃] ⁻	-	-	-	-	-	2.55	4.18~ 4.19	110.51~ 110.65	34.67~ 34.73	-
MAGe(Bh) ₃	1.49	1.09	1.04	108.94	112.16	2.53	3.85	98.85~ 98.96	40.51~ 40.58	3.40
[GeBr ₃] ⁻	-	-	-	-	-	2.53	3.90	100.62~ 100.65	39.67~ 39.68	-
MAGeBr ₃	1.49	1.09	1.04	108.69	112.69	2.50~ 2.59	3.76~ 3.81	93.40~ 97.09	40.69~ 43.43	3.28~ 3.58
RbGeBr ₃ ^c	-	-	-	-	-	2.52~ 2.54	3.72~ 3.76	94.59~ 96.35	41.78~ 42.90	3.21~ 3.26
CsGeBr ₃ ^c	-	-	-	-	-	2.53	3.74	95.16	42.42	3.12
[GeI ₃] ⁻	-	-	-	-	-	2.77	4.32	102.13~ 102.33	38.83~ 38.93	-
MAGeI ₃	1.49	1.09	1.04	108.74	112.98	2.74~ 2.85	4.11~ 4.23	93.08~ 99.12	39.83~ 43.85	3.25~ 3.47
CsGeI ₃ ^c	-	-	-	-	-	2.74	3.87	96.77	41.63	3.26
[SnCl ₃] ⁻	-	-	-	-	-	2.54	3.85~ 3.86	98.60~ 98.82	40.58~ 0.70	-
MASnCl ₃ ^b	1.49	-	-	-	-	2.60~ 2.69	3.61~ 4.07	86.16~ 100.12	39.34~ 48.01	3.06~ 3.18
CsSnCl ₃ (RT) ^c	-	-	-	-	-	2.49~ 2.55	3.45~ 3.64	86.95~ 92.26	43.24~ 46.19	3.21~ 3.77
[Sn(Bh) ₃] ⁻	-	-	-	-	-	2.67	4.34	108.78~ 108.90	35.55~ 35.62	-
MASn(Bh) ₃	1.49	1.09	1.04	108.86	112.36	2.78	4.06	93.82~ 93.88	43.05~ 43.09	3.32
[SnBr ₃] ⁻	-	-	-	-	-	2.70	4.12~ 4.13	99.59~ 99.64	40.18~ 40.21	-
MASnBr ₃ ^c	1.49	1.09	1.04	108.71	113.05	2.83~ 2.96	4.00~ 4.34	86.57~ 98.39	40.16~ 47.04	3.04
[SnI ₃] ⁻	-	-	-	-	-	2.94	4.54~ 4.55	101.09~ 101.18	39.40~ 39.47	-
MASnI ₃ ^c	1.49	1.09	1.04	108.83	112.83	3.01~ 3.10	4.31~ 4.50	88.87~ 95.03	41.70~ 45.57	3.17

FA ⁺	1.31	1.09	1.01	117.36	119.97~ 123.19	-	-	-	-	-
FAGeCl ₃	1.31	1.09	1.02	117.47	119.11~ 122.35	2.35~ 2.38	3.44~ 3.50	92.51~ 95.66	41.89~ 43.88	3.47~ 3.52
FAGe(Bh) ₃	1.31	1.09	1.02	117.67	119.08~ 122.34	2.49~ 2.56	3.76~ 3.91	94.75~ 101.54	38.62~ 42.73	3.48~ 3.57
FAGeBr ₃	1.31	1.09	1.02	117.82	119.23~ 122.07	2.52~ 2.56	3.72~ 3.83	93.15~ 97.99	40.66~ 43.46	3.36~ 3.45
FAGeI ₃	1.31	1.09	1.02	118.28	119.13~ 121.91	2.76~ 2.81	4.08~ 4.31	94.13~ 101.41	38.96~ 43.39	3.28~ 3.35
FASnCl ₃	1.31	1.09	1.02	117.59	118.00~ 123.99	2.56~ 2.71	3.66~ 3.87	87.09~ 94.83	41.25~ 47.83	3.13~ 3.31
FASn(Bh) ₃	1.31	1.09	1.02	117.79	119.35~ 121.93	2.74~ 2.79	3.93~ 4.07	89.38~ 94.69	42.14~ 45.36	3.26~ 3.34
FASnBr ₃	1.31	1.09	1.02	117.87	119.00~ 122.16	2.78~ 3.10	3.99~ 4.43	86.80~ 96.35	41.14~ 49.45	3.22
FASnI ₃ ^c	1.31	1.09	1.02	118.06	119.17~ 122.16	3.09~ 3.13	4.21~ 4.59	85.09~ 95.25	42.06~ 47.50	3.14

^aAvailable experimental data from 2 to 475 K with different crystal structures [3].

^bAvailable experimental data of the monoclinic (Space group = *Pc*) at 318 K [4].

^cAvailable experimental data [5-10].

Besides evaluating the structures of the super-halogens in various materials under ambient conditions, it is noted that all the studied hybrid perovskites tend to adopt a cubic phase at high temperatures (as shown in the last row of Table S3). The super halogens in such high symmetric phase appear to be regular octahedral. The halogen atom X on the vertices of an octahedron is shared by the two neighboring super-halogens, i.e. each X provides ‘half’ electron to bond with the center metal ion to make $[(M^{+1/2})_2(X^{-1/2})_6]^- = [MX_3]^-$. Suppose, in a pyramidal configuration, the M-X bond is a normal two-center two-electron bond with bond order $n_b = 1$, then a symmetric X-M-X bond in the octahedron can be described as a three-center four-electron bond with two electrons participating in bonding and the other two ascribed to the neighboring octahedra occupying the non-bonding orbital. The bond order in such a case is regarded as $n_b = 0.5$. In other words, the total number of bonding electrons on a symmetric X-M-X bond remains unchanged upon deformation to a single M-X bond with the *trans* M...X bond length approaching infinity. Indeed, as found in our cluster calculations of the super-halogen $[SnI_3]^-$ in both its symmetric and asymmetric forms, the stretching frequency of a M-X bond in the pyramid is $\omega_{X-M} = 145 \text{ cm}^{-1}$ and the frequency of M vibrating in a symmetric X-M-X bond is $\omega_{X-M-X} = 101 \text{ cm}^{-1}$, which makes the ratio between the two corresponding force constants $k_{M-X}/k_{X-M-X} = (\omega_{X-M}/\omega_{X-M-X})^2 \approx 2$. Such a ratio suggests the

bond strength of a symmetric X-M-X bond being exactly half of the M-X bond in a pyramid, as the bonding electron of the latter is equally shared between two symmetric bonds in the former.

Based on the assumption that the electron density of the ground state decreases exponentially with the distance from the nucleus, the bond order of M-X bond in X...M-X can be expressed as (the Pauling's equation [11])

$$n_b = n_0 \exp\left(-\frac{d_{M-X} - d_0}{a}\right), \quad (\text{S47})$$

where d_{M-X} is the bond length of M-X. n_0 is the bond order when $d_{M-X} = d_0$. Because of the conservation of the total bond order (as discussed above), the bond order of the *trans* X...M in X...M-X should be

$$n_{trans} = 1 - n_b = n_0 \exp\left(-\frac{d_{M...X} - d_0}{a}\right) \quad (\text{S48})$$

with $d_{M...X}$ being the bond length of the *trans* bond X...M. a is the characteristic length of a specific M-X bond, measuring how fast the bond order is reduced because of bond length increase. A bigger a corresponds to slower change of the bond order with the bond length, and vice versa.

From Eq. (S47)-(S48), it can be seen that, when the super-halogen adopts a completely asymmetric form (like in a pyramidal geometry), we have

$$d_{M-X} = d_0, \quad n_b = 1 \quad (\text{S49})$$

and the *trans* X...M bond length

$$d_{M...X} \rightarrow \infty. \quad (\text{S50})$$

For a large bond length, one would imagine that the bond order should be much less sensitive to the change of bond length than for a short bond length. For example, when the *trans* bond length $d_{M...X} \rightarrow \infty$, the bond order will be essentially zero and will hardly change with increasing $d_{M...X}$. On the other hand, the bond order of M-X will decrease fast with small $d_{M...X} - d_0$. Indeed, the exponential function in Eq. (S47)-(S48) describes such behavior nicely, as the derivative of the exponential function also decreases exponentially with respect to the bond length. When the super-halogen adopts a symmetric form with

$$d_{X...M} = d_{M-X}, \quad (\text{S51})$$

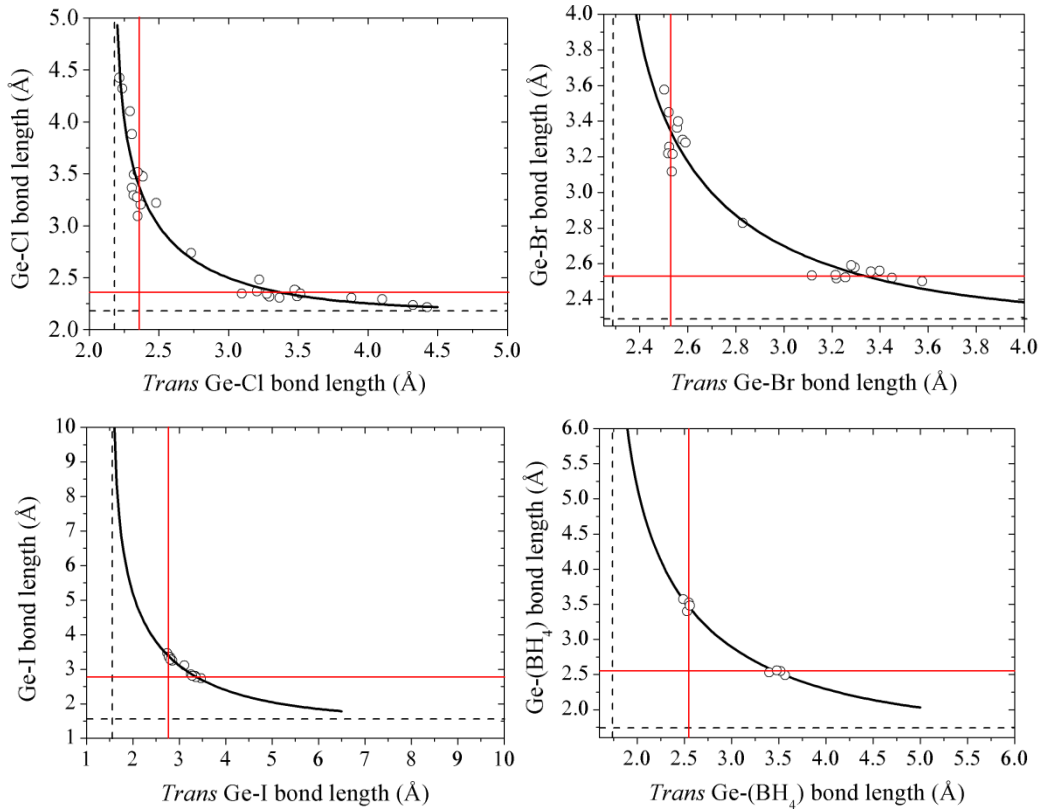
as the case in the regular-octahedron geometry, we have

$$n_{trans} = n_b = \frac{1}{2}. \quad (\text{S52})$$

Combining Eq. (S47) and (S48), we can obtain the relation between the bond length of M-X and the corresponding bond length of the *trans* X...M,

$$d_1 = -a \ln \left[\exp\left(-\frac{d_0}{a}\right) - \exp\left(-\frac{d_2}{a}\right) \right]. \quad (\text{S53})$$

Since the values that $d_{X...M}$ and d_{X-M} can take are totally symmetric, we have put one of them as d_1 and the other as d_2 in Eq. (S53). Now, we can use Eq. (S53) to fit to the bond length data extracted from the experimental or simulated crystal structures for different phases of all the studied hybrid perovskites. For the bond involving super halogen $[\text{BH}_4]^-$, we take the bond length between the metal and the boron atom.



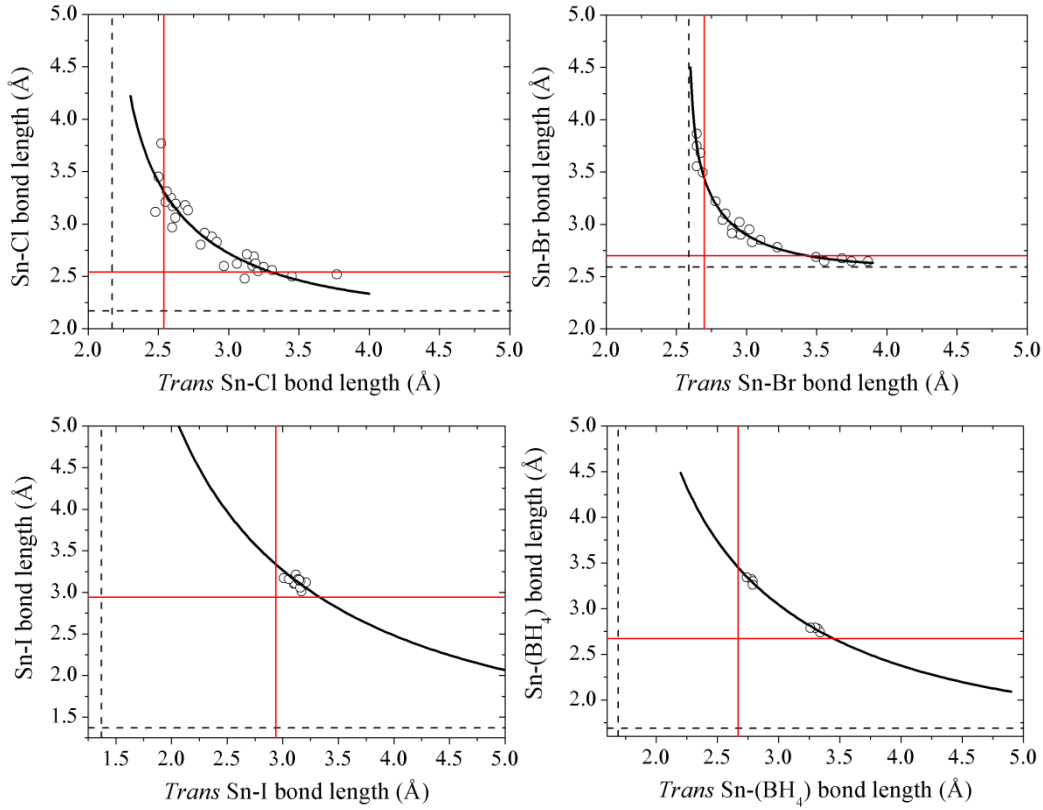


Fig.S7 Least-square fitting to the (*trans*) bond length (X...M) with M-X data taken from experiments or simulations by using Eq. (S53). The dashed lines in each case are the asymptotical lines at which the bond length is d_0 and the *trans* bond length is infinity. The red lines in each case mark the bond length of an isolated $[\text{MX}_3]^-$ pyramid from a cluster calculation.

For each material, we can obtain the characteristic length a and the bond length d_0 that M-X should have in an ‘ideal asymmetrical’ pyramid in the crystal, as listed in Table S5. The fittings are shown in Figure S7. As expected, the M-X bond length asymptotically approaches d_0 where its *trans* bond length X...M goes to infinity. We drew the bond length found for the isolated pyramid in a cluster calculation as the red line in each case. It turns out that this cluster bond length, d_c , marks the boundary of the (*trans*) bond length (X...M) M-X that are found in a crystal (as the intersection points between the bond length curve and the two red lines in each figure). Given the *trans* bond length of d_c calculated from Eq. (S53) as d_c^{trans} , the following relation approximately holds

$$d_c \leq d_1 \leq d_c^{\text{trans}}, \quad d_c^{\text{trans}} \geq d_2 \geq d_c. \quad (\text{S54})$$

This shows that there is very little difference between the chemistry of bonding in an isolated super-halogen and that in the bulk crystal. In the low-temperature low-symmetry phases, such as triclinic, monoclinic, orthorhombic and rhombohedral phases generally observed in the hybrid perovskites, the super ions $[\text{MX}_3]^-$ adopt the asymmetrical form of a pyramid and have

a M-X bond length around d_c . In the high-temperature high-symmetry phases, such as tetragonal and cubic phases often observed in the hybrid perovskites, part of the bonding electrons in the M-X bond ‘moves’ to the other side of M to form a *trans* bond X...M. The reduction of the bond order in M-X will increase the bond length, while the increase of the bond order in X...M will decrease the *trans* bond length, until a symmetric (*trans*) bond X-M-X is formed corresponding to half bond order in M-X. The super-ions $[\text{MX}_3]^-$ in such a case adopt a form of square pyramid or octahedron with high symmetry.

Given the symmetric nature for the change of (*trans*) bond length (X...M) M-X and a relatively large parameter a , the characteristic curves in Figure S7 can be approximated by an ‘isosceles right triangle’ in the left panel of Figure S8. According to simple trigonometry, it is found that, within the range bounded by the red lines (corresponding to d_c and its *trans* d_c'), the sum between any bond length (d_1) and its *trans* bond length (d_2) will be a constant

$$d_1 + d_2 = 2d_{1/2}, \quad (\text{S55})$$

where $d_{1/2}$ is the bond length when X-M-X in its symmetric form with the bond order $n_b = 0.5$. This is a good approximation. For example, with the smallest a among the series, $[\text{SnBr}_3]^-$ has $d_c = 2.7 \text{ \AA}$ and the corresponding *trans* bond length $d_c' = 3.4 \text{ \AA}$, the sum of the two 6.1 \AA agrees well with $2d_{1/2} = 5.9 \text{ \AA}$. $[\text{GeCl}_3]^-$ has the second smallest a , its sum $d_c + d_c' = 2.36 + 3.36 = 5.72 \text{ \AA}$ agrees well with its $2d_{1/2} = 5.42 \text{ \AA}$. Thus, the super-halogen in each hybrid perovskite can be represented by a specific characteristic triangle (as in Figure S8) -- it adopts a polarized (asymmetrical) pyramidal form in low-symmetry phases and changes to a symmetrical form of octahedron in high-symmetry phases. In fact, such behavior is just like a regular ion, where in the cubic phase, the ion on the high-symmetry site must assume a spherical shape. However, ions on the low-symmetry site may adopt a polarized (asymmetrical) shape, like found in the recent study of chalcogen ions in pyrite-type crystals, where an ellipsoidal shape is proposed to describe each ion [12].

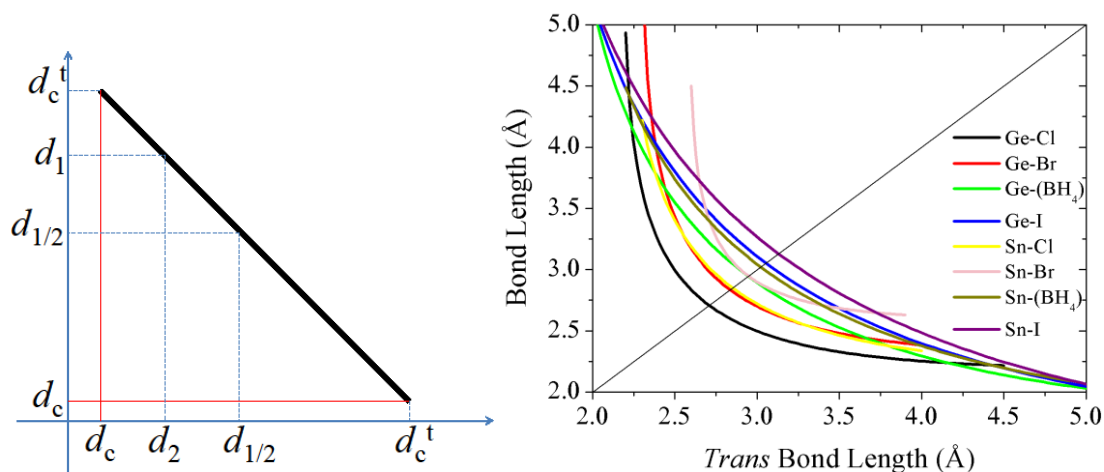


Fig.S8 Left panel: schematic plot of a characteristic triangle of a super-halogen in the crystal. Right panel: the characteristic curves of bond length of the studied super-halogens in the crystals. The intersection between each curve and the diagonal line indicate the bond length value at 0.5 bond order in that super-halogen.

The characteristic curves of the bond lengths of all the super-halogens in the crystals are given in the right panel of Figure S8. The diagonal line intersects each curve at $d_{1/2}$ ($n_b = 0.5$). In the Ge series, $d_{1/2}$ is increasing in the order Ge-Cl, Ge-Br, Ge-(BH₄) and Ge-I due to the reduced bond polarizability. The same trend goes for the Sn series. In the figure, larger curvature and smaller $d_{1/2}$ implies that the bond order changes fast (small a) with the bond length and the corresponding super-halogen is more likely to assume a polarized (asymmetric) form of pyramid in the crystal.

To sum up the previous discussions, the geometries of the same super-alkali [MA/FA]⁺ or super-halogen [MX₃]⁻ changes little throughout the studied crystals under ambient condition. For different (temperature) phases of a material, the super halogen [MX₃]⁻ may adopt a polarized (asymmetric) pyramidal form in the low-symmetry phases and an octahedral symmetric form in the cubic phase. However, its geometrical dimension is bounded by the corresponding characteristic triangle (Figure S8). The two right-angle sides of such a triangle are equal to the difference between the *trans* bond length and the bond length of M-X of the isolated cluster ($d_c^t - d_c$). The only physical assumption used to define the characteristic triangle is that the electronic density of an atom decreases exponentially with the distance from the nucleus.

Now, we can start defining the ionic radii for super-alkalis and super-halogens. The *intuitive* definition of a radius r for an ion implies the ion has a symmetric form – a sphere for a regular ion and a regular octahedron for a super-halogen which can be put inside a sphere with its vertices touching the spherical surface. Moreover, in order to use the interionic distance data to calculate the ionic radii, it is actually much easier to define the ionic radius for its symmetric form, because, for the corresponding cubic phase of the crystal, one can directly calculate the interionic distance between the cation and the anion using

$$R = r_a + r_h = \frac{\sqrt{3}}{2} L_c. \quad (\text{S56})$$

r_a and r_h are the defined ionic radii of the alkali and the halogen, respectively. L_c is the side length of the cubic cell.

Let us first start with a simple soft-sphere model by allowing the two neighboring super-halogen spheres gently overlap with each other. Such assumption is reasonable given the $[\text{MX}_3]^-$ super-halogen adopts a regular octahedron shape in the cubic phase and shares the electrons of the halogen on the vertex with its neighbor. To obtain a set of radii that are comparable to Shannon’s ionic radii of the alkalis and halogens, we calculate the radii of super-ions based on the Shannon [13] radius of Cs^+ . We found experimental interionic distances for the series CsMX_3 ($\text{M} = \text{Ge}, \text{Sn}$; $\text{X} = \text{Cl}, \text{Br}, \text{I}$). The crystal that has the smallest super-halogen $[\text{MX}_3]^-$ is most likely to satisfy the condition that the cation and the anion touch. We chose Cs^+ over Rb^+ due to the same reason (to make the cation-anion ratio as large as possible). CsGeCl_3 is, therefore, our starting point. The radii of the studied super-alkalis and super-halogens can be calculated hereafter. We used as many experimental data as we could in the process. Table S5 shows the computed ionic radii for those with coordination number (CN) equals 6 and 8. For $\text{CN} = 8$, the cation will be bigger, because the repulsion between neighboring anions will be bigger with larger coordination number. We then used the obtained ionic radii to calculate the interionic distances for the hybrid perovskites that have not been used to compute these radii. The distances agree well with the simulated ones with an average deviation of 0.05 \AA , as shown in Table S6.

Table S5 Fitted values of d_0 and a of Eq. (S53) for different super-halogens. $d_{1/2}$ is the calculated bond length at the bond order $n_b = 0.5$. L_c is the side length of the (pseudo) cubic cell. ‘Bh’ is a short form for $[\text{BH}_4]$. For the cases of coordination number (CN) of 6 and 8 (shown in square brackets in the last column), the ionic radii were calculated directly by assuming that the $[\text{GeCl}_3]$ ‘sphere’ is touching the Cs^+ sphere in CsGeCl_3 crystal. Values in red are the ones adopted to minimize the overlap between the anions. The effective radii of Cs^+ and Rb^+ are the Shannon’s radii [13].

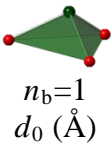
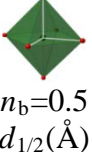
Ion	 $n_b=1$ d_0 (Å)	a (Å)	 $n_b=0.5$ $d_{1/2}$ (Å)	$2d_{1/2}$ (Å)	L_c (Å)	Ionic radius(Å)		Overlap (Å)
Cs^+	-	-	-	-	-	1.81 (CN=6)	1.88 (CN=8)	-
Rb^+	-	-	-	-	-	1.66 (CN=6)	1.75 (CN=8)	-
$[\text{GeCl}_3]^-$	2.18	0.76	2.71	5.42	5.47(CsGeCl_3)	2.93	2.86	0.19[6] 0.12[8]
MA^+	-	-	-	-	5.658(MAGeCl_3)	1.97	2.04	-
$[\text{GeBr}_3]^-$	2.29	0.79	2.84	5.68	5.659(RbGeBr_3) 5.68(CsGeBr_3) 5.93(MAGeBr_3 tetragonal)	3.24(Rb^+) 3.11(Cs^+) 3.16(MA^+)	3.15(Rb^+) 3.04(Cs^+) 3.09(MA^+)	0.19[6] 0.12[8]
$[\text{GeI}_3]^-$	1.56	2.16	3.05	6.10	6.04(CsGeI_3) 6.11(MAGeI_3 tetragonal)	3.42(Cs^+) 3.32(MA^+)	3.35(Cs^+) 3.25(MA^+)	0.26[6] 0.19[8]
$[\text{SnCl}_3]^-$	2.17	0.98	2.85	5.68	5.604(CsSnCl_3) 5.760(MASnCl_3)	3.04(Cs^+) 3.02(MA^+)	2.97(Cs^+) 2.95(MA^+)	0.14[6] 0.07[8]
$[\text{SnBr}_3]^-$	2.59	0.52	2.95	5.90	5.808(CsSnBr_3) 5.901(MASnBr_3)	3.22(Cs^+) 3.14(MA^+)	3.15(Cs^+) 3.07(MA^+)	0.19[6] 0.12[8]
$[\text{SnI}_3]^-$	1.37	2.54	3.13	6.26	6.219(CsSnI_3) 6.243(MASnI_3)	3.58(Cs^+) 3.44(MA^+)	3.51(Cs^+) 3.37(MA^+)	0.32[6] 0.25[8]
FA^+	-	-	-	-	6.329(FASnI_3)	2.04	2.11	-
$[\text{Ge}(\text{Bh})_3]^-$	1.74	1.74	2.94	5.88	5.876(MAGeBh_3 trigonal)	3.12	3.05	0.18[6] 0.11[8]
$[\text{Sn}(\text{Bh})_3]^-$	1.69	1.92	3.02	6.04	6.054(MASnBh_3)	3.27	3.20	0.24[6] 0.17[8]

Table S6 Calculated interionic distances using the ionic radii given in Table S5, compared to the simulated ones.

Material	Simulated interionic distance (Å)	Additive interionic distance (Å)	Residual (Å)
FAGeCl ₃ (trigonal)	5.05	4.97	0.08
FAGeBr ₃ (tetragonal)	5.14	5.20	-0.06
FAGeI ₃ (tetragonal)	5.28	5.36	-0.08
FAGe(BH ₄) ₃ (trigonal)	5.20	5.16	0.04
FASnCl ₃ (trigonal)	5.05	5.06	-0.01
FASnBr ₃ (tetragonal)	5.17	5.18	-0.01
FASn(BH ₄) ₃ (trigonal)	5.24	5.31	-0.07

According to Eq. (S56), we can also use least-square fitting to obtain a set of ionic radii that best fit the experimental and simulated interionic distances, as shown in Table S7. To make the radii consistent with Shannon radii, we set Cs⁺ and Rb⁺ radii fixed at Shannon's values during the fitting. To reduce the number of fitting variables, we also fix the radius of [SnBr₃]⁻ obtained from the calculated electric dielectric constant using Eq. (S45)-(S47).

We test the results by using the Goldschmidt tolerance factor t for perovskites material ABX

$$r_A = t \cdot \sqrt{2} (r_B + r_X) - r_X, \quad (\text{S57})$$

where, in our case, r_A , r_B and r_X are the ionic radii of the super-alkali, the metal and the halogen, respectively. t is found to be between 0.9 and 1.0 for cubic perovskite structures. By using the Shannon's ionic radii of Ge²⁺ (0.87 Å), Sn²⁺ (1.03 Å), Cl⁻ (1.67 Å) and I⁻ (2.06 Å), we estimate the radius range of the cation (MA⁺ and FA⁺) to be between 1.56 and 2.31 Å. Our values in Table S7 fall well within this range.

Table S7 Fitted ionic radii of super-alkalis and super-halogens using Eq. (S56). The mean deviation of the calculated interionic distances compared to the the experimental (or simulated) values is 0.06Å. The upper figure in each case is the calculated one.

Ion		Cs ⁺	MA ⁺	FA ⁺	Rb ⁺
	Ionic radius (Å)	1.88 ^a	2.14	2.21	1.75 ^a
[GeCl ₃] ⁻	2.84	4.72 4.74	4.98 4.90	5.05 5.05	-
[GeBr ₃] ⁻	3.00	4.88 4.92	5.14 5.13	5.21 5.14	4.75 4.90
[GeI ₃] ⁻	3.14	5.02 5.23	5.28 5.29	5.35 5.28	-
[SnCl ₃] ⁻	2.85	4.73	4.99	5.05	-

		4.85	4.99	5.05	
[SnBr ₃] ⁻	2.94 ^b	4.82	5.08	5.14	-
		5.03	5.11	5.17	
[SnI ₃] ⁻	3.27	5.15	5.41	5.48	-
		5.39	5.41	5.48	
[Ge(BH ₄) ₃] ⁻	2.95	-	5.09	5.16	-
			5.09	5.20	
[Sn(BH ₄) ₃] ⁻	3.01	-	5.15	5.22	-
			5.24	5.22	

^aShannon's data of coordination number 8 [13].

^bComputed by using Eq.(S43)-(S46) with the static dielectric constant of MASnBr₃, $\epsilon_0 = 5.67$, obtained from our HSE06 calculation.

Pauling proposed a method to define ionic radii for alkali halide crystals based on the lattice energy [14]

$$U = -\frac{z^2 e^2 A}{r} + \frac{B}{r^n}, \quad (\text{S58})$$

where ze is the charge of an ion and r the interionic distance. The first term on the right hand side is the Coulomb attraction with A being the Madelung constant of the crystal, while the second term is the repulsive potential with

$$B = (r_+ + r_-)^{n-1} B_0 \left[c_{+-} + \frac{1.25 \cdot c_{++}}{r_{++}^n} \left(\frac{2\rho}{1+\rho} \right)^{n-1} + \frac{0.75 \cdot c_{--}}{r_{--}^n} \left(\frac{2}{1+\rho} \right)^{n-1} \right]. \quad (\text{S59})$$

r_+ and r_- are the ionic radii of the cation and anion, respectively. c_{+-} is the cation-anion coordination number which is 6 in a NaCl-alike crystal and 8 in a CsCl-alike crystal. c_{++} and c_{--} are the cation-cation and the anion-anion coordination numbers, respectively. In a NaCl crystal $c_{++} = c_{--} = 12$, while $c_{++} = c_{--} = 6$ in a CsCl crystal. r_{++} and r_{--} are the nearest neighbor cation-cation distance and anion-anion distance, respectively. $\rho = r_+/r_-$ is the radius ratio between the cation and anion. Eq. (S59) shows that the repulsive potential is inversely proportional to the high power of the interionic distance, where the power n is usually taken to be 9 for the alkali halides [14].

If we follow Pauling's strategy, B_0 in Eq. (S59) is chosen to make the equilibrium interionic radius (by putting $U' = 0$)

$$R = (r_+ + r_-)^{\frac{n}{n-1}} \cdot F(\rho) \quad (\text{S60})$$

with the so-called correction factor $F(\rho) = 1$ when $\rho = 0.75$ for NaCl crystals and $\rho = 1.0$ for CsCl crystals. According to Eq. (S58) and (S59), for a general ρ of a NaCl-alike crystal

$$F(\rho) = \left\{ \frac{(1.75)^n \cdot \left((1+\rho)^n + 1.25 \cdot (\sqrt{2}\rho)^n + 0.75 \cdot (\sqrt{2})^n \right)}{(1+\rho)^n \cdot \left((1.75)^n + 1.25 \cdot \left(\frac{\sqrt{2} \cdot 0.75}{\sqrt{\rho}} \right)^n + 0.75 \cdot \left(\frac{\sqrt{2}}{\sqrt{\rho}} \right)^n \right)} \right\}^{\frac{1}{n-1}} \quad (\text{S61})$$

and for a CsCl-alike crystal

$$F(\rho) = \left\{ \frac{(1.75)^n \cdot \left((1+\rho)^n + 1.25 \cdot 0.375 \cdot (\sqrt{3}\rho)^n + 0.75 \cdot 0.375 \cdot (\sqrt{3})^n \right)}{(1+\rho)^n \cdot \left((1.75)^n + 1.25 \cdot 0.375 \cdot \left(\frac{\sqrt{3} \cdot 0.75}{\sqrt{\rho}} \right)^n + 0.75 \cdot 0.375 \cdot \left(\frac{\sqrt{3}}{\sqrt{\rho}} \right)^n \right)} \right\}^{\frac{1}{n-1}} \quad (\text{S62})$$

The correction factors in Eq. (S61) and (S62) have the advantage of taking into account both the anion-anion and the cation-cation repulsion (so-called double repulsion) at the critical radius ratio ($\rho = 0.414$ for NaCl crystals and $\rho = 0.732$ for CsCl crystals) when the anion and cation as well as the anion and anion are just touching each other in a hard-sphere model. Such repulsion will effectively make the equilibrium bond length longer than the cation-anion ionic radii added together. This is quite different from our soft-sphere model discussed before.

Figure S9 shows the correction factor against the radius ratio as calculated from Eq. (S61) and (S62). Clearly, both lines (solid red and black) deviate upwards significantly from 1.0 at the critical ratios (0.414 and 0.732). For small radius ratios, the $n \rightarrow \infty$ line of the 8 coordination (dotted black) goes above the $n = 9$ line (solid black), as opposed to the case of 6-coordination lines. This reflects that the large coordination number produces small anion-anion distance and the repulsion increases much faster for larger n . With certain correction factor, the 6-coordination line corresponds to smaller ratio than the 8-coordination line, suggesting that the cation radius tends to increase with the coordination number due to larger repulsion between the anions.

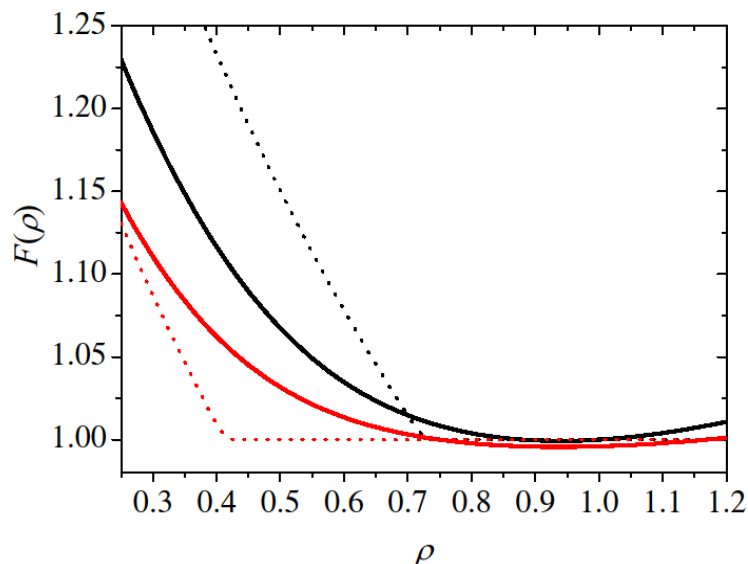


Fig. S9 Calculated correction factor against the radius ratio for NaCl-like (in red) and CsCl-like (in black) crystals using Eq.(S61) and (S62), respectively. The dotted line corresponds to the correction factor when the power n tends to infinity in each case, i.e. when the repulsion is infinitely small for large interionic distance and is infinitely large for small interionic distance.

Pauling in his work [14] has defined the ionic radii for all the alkalis ($= \text{Li}^+, \text{Na}^+, \text{K}^+, \text{Rb}^+, \text{Cs}^+$) and halogens ($= \text{F}^-, \text{Cl}^-, \text{Br}^-, \text{I}^-$) by using Eq. (S61) to fit to the experimental interionic distances of the alkali halide crystals. To define a set of ionic radii for the super-alkalis and super-halogens that are consistent and comparable with Pauling's data, we first note that abundant experimental data are available for $[\text{Cs/Rb}]^+[\text{super halogen}]^-$ salts, as indicated in Table S5. Thus, by using Pauling's ionic radii of Cs^+ and Rb^+ and by using Eq. (S61)-(S62), we can define a set of ionic radii for the super-alkalis and super-halogens that are able to best fit the available and simulated interionic distances. The fitted ionic radii are shown for both NaCl-like crystals ($\text{CN} = 6$) and CsCl-like crystals ($\text{CN} = 8$) in Table S8 and S9, respectively. Together shown are the calculated interionic distances compared to the measured or simulated ones. Note that the interionic distances deviate from the sum of the corresponding ionic radii due to the repulsion between like and unlike ions as contained in the correction factor of $F(\rho)$. The experimental (or simulated) interionic distances fit very well by these ionic radii, with the radii obtained for the 8 coordination number showing a slightly better overall fitting than the 6-coordinated ones.

Table S8 Fitted ionic radii for coordination number 6. The mean deviation of the calculated interionic distances from the experimental (or simulated) ones is 0.045Å. The upper figure in each case is the calculated one.

Ion		Cs ⁺	MA ⁺	FA ⁺	Rb ⁺
	Ionic radius (Å)	1.434 ^a	1.632	1.686	1.294 ^a
[GeCl ₃] ⁻	2.492	4.737 4.737	4.957 4.900	5.020 5.050	-
[GeBr ₃] ⁻	2.610	4.919 4.919	5.134 5.135	5.196 5.136	4.780 4.901
[GeI ₃] ⁻	2.714	5.081 5.231	5.291 5.291	5.351 5.276	-
[SnCl ₃] ⁻	2.513	4.769 4.853	4.988 4.988	5.051 5.051	-
[SnBr ₃] ⁻	2.594	4.895 5.030	5.120 5.110	5.172 5.166	-
[SnI ₃] ⁻	2.799	5.216 5.386	5.422 5.406	5.481 5.481	-
[Ge(BH ₄) ₃] ⁻	2.580	-	5.089 5.089	5.151 5.196	-
[Sn(BH ₄) ₃] ⁻	2.624	-	5.155 5.243	5.216 5.216	-

^aPauling's data [14].

Table S9 Fitted ionic radii for coordination number 8. The mean deviation of the calculated interionic distances from the experimental (or simulated) ones is 0.038Å. The upper figure in each case is the calculated one.

Ion		Cs ⁺	MA ⁺	FA ⁺	Rb ⁺
	Ionic radius (Å)	1.434 ^a	1.617	1.674	1.294 ^a
[GeCl ₃] ⁻	2.425	4.795 4.737	4.900 4.900	4.965 5.050	-
[GeBr ₃] ⁻	2.542	4.953 4.919	5.055 5.135	5.118 5.136	5.117 4.901
[GeI ₃] ⁻	2.648	5.195 5.231	5.291 5.291	5.351 5.276	-
[SnCl ₃] ⁻	2.476	4.884 4.853	4.987 4.988	5.051 5.051	-
[SnBr ₃] ⁻	2.548	5.010 5.030	5.110 5.110	5.172 5.166	-
[SnI ₃] ⁻	2.738	5.329 5.386	5.423 5.406	5.481 5.481	-
[Ge(BH ₄) ₃] ⁻	2.535	-	5.124 5.089	5.186 5.196	-
[Sn(BH ₄) ₃] ⁻	2.578	-	5.214 5.243	5.275 5.216	-

^aPauling's data [14].

All the ionic radii defined above should be considered as the ionic radii of the super-halogens when they adopt the symmetric form, because all the interionic distances we used in the fittings are either from the cubic phase or from a high-symmetry cell calculated as a cubic one. Under ambient conditions, the hybrid perovskites usually show a less-symmetric phase and the super-halogens adopt a polarized form of pyramid or square pyramid. Based on our discussion about the characteristic triangle of the super-halogen $[\text{MX}_3]^-$, its symmetric form (regular octahedron) should have a larger radius than its polarized form (pyramid), given the former has bigger geometrical dimension due to the longer M-X bond distances and more distributed electrons. Indeed, if we compare the volume per molecule between the low symmetry phase and the high symmetry phase of the same material, the volume decreases with lower symmetry. This is commonly observed in the displacive phase transition of perovskites, where a high-symmetry phase with larger volume is favored over a low-symmetry distorted phase at higher temperatures due to its larger entropy term in the Gibbs free energy. It should be noted that, when we define the effective ionic radii, we ignore the thermal expansion effect of the material. The ordinary linear thermal expansion coefficient is in the order of $1 \times 10^{-6}/\text{K}$, which means for a crystal with cell length as large as 10 Å, increasing 1000 K in temperature will only affect the second decimal place of the cell length or the ionic radii. For the temperature in our consideration (several hundred K), the effect of thermal expansion would be on the third decimal place of the ionic radii.

In order to estimate the ionic radii for the ‘pyramidal’ super-halogens, we first note that the bond length of the symmetric form (regular octahedron) $d_{1/2}$ is correlated with its defined radius. Figure S10 shows the calculated bond lengths of the super-halogens in their symmetric form (see the data of $n_b = 0.5$ in Table S5) against the defined ionic radii in Table S7 and S8. Approximately, the ionic radius is linearly proportional to the bond length. Linear fittings reveal that the ratios are 0.8 and 1.3 for the Shannon’s type radii (Table S7) and Pauling’s type radii (Table S9), respectively.

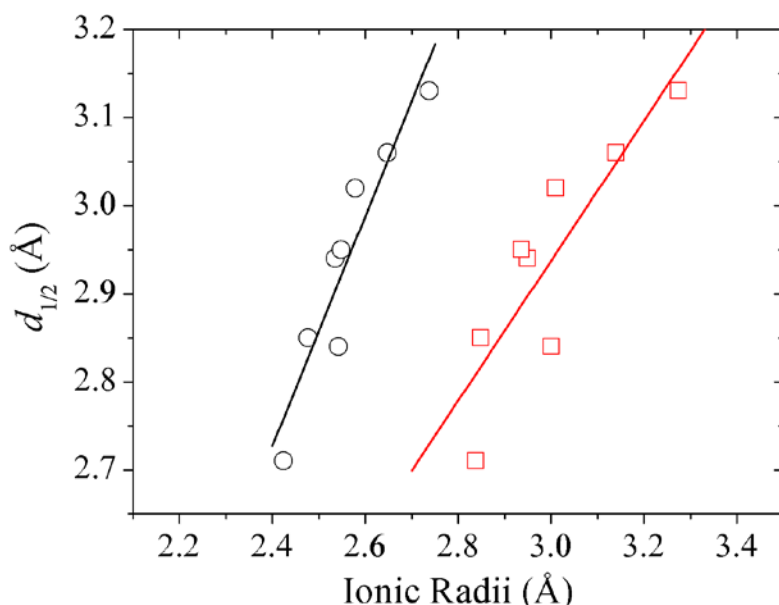


Fig. S10 The approximately linear relation between the bond length $d_{1/2}$ ($n_b = 0.5$) and the defined Shannon-type (red square) and Pauling-type (black circle) ionic radii of the super-halogens in the symmetric form. The solid lines represent linear fit. The slopes of the black and red lines are 1.3 and 0.8, respectively. The intercepts are -0.4 and 0.5 , respectively.

Since $d_{1/2}$ is correlated with the cluster bond length d_c of the pyramidal form of the super-halogens according to the characteristic triangle, it is only natural to define the ionic radii for the pyramidal super-halogens by assuming the same linear relationship between d_c and the radii. Table S11 shows the calculated ionic radii of the pyramidal super-halogens using this method. As expected, the calculated ionic radii of the pyramidal super-halogens are smaller than the ones with the symmetric configurations.

Table S11 Calculated ionic radii of super halogens in their pyramidal form by using the cluster bond length d_c . The Shannon-type radii correspond to the slope of 0.8 and the intercept of 0.5 \AA . The Pauling-type radii correspond to the slope of 1.3 and the intercept of -0.4 \AA . For comparison, the Shannon-type or Pauling-type radius of the symmetric super-halogen is the lower figure in each case.

Super halogen	$d_c(\text{\AA})$	Ionic radii of pyramid (\AA)	
		Slope = 0.8 Intercept = 0.5 \AA	Slope = 1.3 Intercept = -0.4 \AA
$[\text{GeCl}_3]^-$	2.36	2.32 (2.84)	2.123 (2.425)
$[\text{GeBr}_3]^-$	2.53	2.54 (3.00)	2.254 (2.542)
$[\text{GeI}_3]^-$	2.77	2.84 (3.14)	2.438 (2.648)
$[\text{SnCl}_3]^-$	2.54	2.55 (2.85)	2.261 (2.476)
$[\text{SnBr}_3]^-$	2.7	2.75	2.385

		(2.94)	(2.548)
$[\text{SnI}_3]^-$	2.94	3.05 (3.27)	2.569 (2.738)
$[\text{Ge}(\text{BH}_4)_3]^-$	2.55	2.56 (2.95)	2.269 (2.535)
$[\text{Sn}(\text{BH}_4)_3]^-$	2.67	2.71 (3.01)	2.361 (2.578)

Now, with the effective ionic radii of the super-alkalis and super-halogens properly defined, we can compute the electronic band gaps of the alkali halides and the hybrid perovskites in our physical model and compare the results with available experiments. Table S12 lists the model calculated band gaps of the alkali halides and the available experimental values. We emphasize that one must use the radii of cation and anion computed within the same method. For example, one should not use Shannon’s radius for the cation and Pauling’s radius for the anion in the same calculation, because these radii are defined self-consistently only within the same category. Also, only the data from the same type of radii (Shannon or Pauling) are comparable to each other. It is inappropriate to compare, for example, the band gap calculated using Shannon’s radii to a band gap using Pauling’s radii. Table S13 lists the computed band gaps of the studied hybrid perovskites with the experimental values or the values from PBE, HSE06 and GW calculations, whichever is available.

Table S12 Calculated band gaps (E_g) of the alkali halides using our physical model (see Eq. (S23), (S33) and (S36)). Experimental data (Exp.) [15] are given for comparison. $\Delta\chi$ is the ionicity of the bond defined in Eq. (S3). R_+ and R_- are the ionic radii. In each case, Shannon radius (S) is the upper number and Pauling radius (P) is the lower number. L_c is the cell length of the model calculated as twice the sum of R_+ and R_- . For Pauling’s radii, the correction factor in Eq. (S31) has been used in computing L_c . In the CsX (X = halogen) series, Cs^+ is 6-coordinated in CsF and 8-coordinated in the others, corresponding to Shannon’s radii 1.81 Å and 1.88 Å, respectively.

Material	$\Delta\chi$ (eV)	R_+ (Å)	R_- (Å)	L_c	E_g (eV)	Exp. (eV)
LiF	18.74	0.90 (S)	1.19 (S)	4.18 (S)	10.9 (S)	13.6
		0.574 (P)	1.225 (P)	4.016 (P)	10.1 (P)	
LiCl	12.73	0.90 (S)	1.67 (S)	5.14 (S)	6.7 (S)	9.4
		0.574 (P)	1.589 (P)	5.134 (P)	5.5 (P)	
LiBr	11.24	0.90 (S)	1.82 (S)	5.44 (S)	5.9 (S)	7.6
		0.574 (P)	1.702 (P)	5.494 (P)	4.6 (P)	
NaF	18.91	1.16 (S)	1.19 (S)	4.70 (S)	8.2 (S)	11.7
		0.873 (P)	1.225 (P)	4.614 (P)	8.2 (P)	
NaCl	12.90	1.16 (S)	1.67 (S)	5.66 (S)	5.5 (S)	8.5
		0.873 (P)	1.589 (P)	5.630 (P)	5.2 (P)	
NaBr	11.41	1.16 (S)	1.82 (S)	5.96 (S)	5.0 (S)	7.7
		0.873 (P)	1.702 (P)	5.958 (P)	4.6 (P)	

KF	19.89	1.52 (S) 1.173 (P)	1.19 (S) 1.225 (P)	5.42 (S) 5.326 (P)	5.6 (S) 5.8 (P)	10.7
KCl	13.88	1.52 (S) 1.173 (P)	1.67 (S) 1.589 (P)	6.38 (S) 6.280 (P)	4.1 (S) 4.2 (P)	8.4
KBr	12.39	1.52 (S) 1.173 (P)	1.82 (S) 1.702 (P)	6.68 (S) 6.586 (P)	3.7 (S) 3.8 (P)	7.4
KI	10.49	1.52 (S) 1.173 (P)	2.06 (S) 1.867(P)	7.16 (S) 7.054 (P)	3.3 (S) 3.3 (P)	6.0
RbF	20.21	1.66 (S) 1.294 (P)	1.19 (S) 1.225 (P)	5.70 (S) 5.634 (P)	5.0 (S) 5.1 (P)	10.4
RbCl	14.20	1.66 (S) 1.294 (P)	1.67 (S) 1.589 (P)	6.66 (S) 6.554 (P)	3.7 (S) 3.8 (P)	8.2
RbBr	12.71	1.66 (S) 1.294 (P)	1.82 (S) 1.702 (P)	6.96 (S) 6.868 (P)	3.4 (S) 3.4 (P)	7.5
RbI	10.81	1.66 (S) 1.294 (P)	2.06 (S) 1.867(P)	7.44 (S) 7.326 (P)	3.0 (S) 3.0 (P)	6.2
CsF	20.45	1.81 (S) 1.434 (P)	1.19 (S) 1.225 (P)	6.00 (S) 6.010 (P)	4.4 (S) 4.3 (P)	10.9
CsCl	14.44	1.88 (S) 1.434 (P)	1.67 (S) 1.589 (P)	7.10 (S) 6.910 (P)	3.1 (S) 3.3 (P)	8.3
CsBr	12.95	1.88 (S) 1.434 (P)	1.82 (S) 1.702 (P)	7.40 (S) 7.208 (P)	2.9 (S) 3.1 (P)	7.3
CsI	11.05	1.88 (S) 1.434 (P)	2.06 (S) 1.867(P)	7.88 (S) 7.656 (P)	2.6 (S) 2.7 (P)	6.3

Table S13 Calculated band gaps (E_g) of the studied hybrid perovskites using our physical model (see Eq. (S23), (S33) and (S36)). Experimental data (Exp.) or calculated ones from DFT (PBE, HSE and GW) are given for comparison. $\Delta\chi$ is the ionicity of the bond defined in Eq. (S3). R_+ and R_- are the ionic radii of the cation and anion, respectively. In each case, Shannon-type radius (S) is the upper figure and Pauling-type radius (P) the lower one. The radii for the case of 8 coordination number are used. The left figure is when the super-halogen is in its symmetric form (regular octahedron in the cubic phase) and the right figure is when the super-halogen adopts its pyramidal form (in low-symmetry phases) with all three M-X bond lengths close to d_c . L_c is the cell length in the model calculated as twice the sum of R_+ and R_- . For Pauling-type radii, the correction factor in Eq. (S31) has been used in computing L_c .

Material	$\Delta\chi$ (eV)	R_+ (Å)	R_- (Å)	L_c	E_g (eV)	Exp/DFT. (eV)
CsGeCl ₃	8.88	1.88(S) 1.434(P)	2.84/2.32(S) 2.42/2.12(P)	9.44/8.40(S) 9.59/8.49(P)	1.74~2.30(S) 1.65~2.20(P)	3.67(Exp.) ^a
CsGeBr ₃	8.32	1.88(S) 1.434(P)	3.00/2.54(S) 2.54/2.25(P)	9.76/8.84(S) 9.91/8.91(P)	1.62~2.06(S) 1.54~1.98(P)	2.32(Exp.) ^a
CsSnCl ₃	9.35	1.88(S) 1.434(P)	2.85/2.55(S) 2.48/2.26(P)	9.46/8.86(S) 9.77/8.93(P)	1.71~2.00(S) 1.57~1.93(P)	4.5(Exp.) ^b
CsSnBr ₃	8.65	1.88(S) 1.434(P)	2.94/2.75(S) 2.55/2.38(P)	9.64/9.26(S) 10.02/9.34(P)	1.66~1.82(S) 1.49~1.76(P)	1.8(Exp.) ^b
CsSnI ₃	7.92	1.88(S) 1.434(P)	3.27/3.05(S) 2.74/2.57(P)	10.30/9.86(S) 10.66/9.97(P)	1.44~1.59(S) 1.30~1.53(P)	1.3(Exp.) ^b
MASnCl ₃	10.2	2.14(S) 1.62(P)	2.85/2.55(S) 2.48/2.26(P)	9.98/9.38(S) 9.97/9.31(P)	1.49~1.72(S) 1.48~1.74(P)	3.69(Exp.) ^c
MASnBr ₃	9.5	2.14(S) 1.62(P)	2.94/2.75(S) 2.55/2.38(P)	10.16/9.78(S) 10.22/9.70(P)	1.44~1.58(S) 1.41~1.59(P)	2.15(Exp.) ^d
MASnI ₃	8.77	2.14(S)	3.27/3.05(S)	10.82/10.38(S)	1.26~1.39(S)	1.3(Exp.) ^d

		1.62(P)	2.74/2.57(P)	10.85/10.30(P)	1.24~1.40(P)	
MASn(BH ₄) ₃	8.81	2.14(S) 1.62(P)	3.01/2.71(S) 2.58/2.36(P)	10.30/9.70(S) 10.43/9.62(P)	1.41~1.63(S) 1.36~1.64(P)	3.61(HSE) 2.8(PBE)
MAGeCl ₃	9.73	2.14(S) 1.62(P)	2.84/2.32(S) 2.42/2.12(P)	9.96/8.92(S) 9.80/8.89(P)	1.50~1.95(S) 1.55~1.95(P)	3.72(GW) ^e
MAGeBr ₃	9.17	2.14(S) 1.62(P)	3.00/2.54(S) 2.54/2.25(P)	10.28/9.36(S) 10.11/9.29(P)	1.41~1.76(S) 1.45~1.78(P)	3.69(HSE) 2.87(PBE)
MAGeI ₃	8.53	2.14(S) 1.62(P)	3.14/2.84(S) 2.65/2.44(P)	10.56/9.96(S) 10.58/9.87(P)	1.34~1.54(S) 1.32~1.56(P)	2.53(HSE) 1.95(PBE)
MAGe(BH ₄) ₃	8.51	2.14(S) 1.62(P)	2.95/2.56(S) 2.53/2.27(P)	10.18/9.40(S) 10.25/9.33(P)	1.46~1.77(S) 1.42~1.78(P)	4.16(HSE) 3.23(PBE)
FASnCl ₃	8.71	2.21(S) 1.67(P)	2.85/2.55(S) 2.48/2.26(P)	10.12/9.52(S) 10.10/9.42(P)	1.48~1.71(S) 1.47~1.74(P)	2.72(HSE) 2.02(PBE)
FASnBr ₃	8.01	2.21(S) 1.67(P)	2.94/2.75(S) 2.55/2.38(P)	10.30/9.92(S) 10.34/9.80(P)	1.44~1.58(S) 1.41~1.60(P)	2.78(HSE) 2.15(PBE)
FASnI ₃	7.28	2.21(S) 1.67(P)	3.27/3.05(S) 2.74/2.57(P)	10.96/10.52(S) 10.96/10.39(P)	1.26~1.39(S) 1.25~1.41(P)	1.41(Exp.) ^f 1.62(PBE)
FASn(BH ₄) ₃	7.32	2.21(S) 1.67(P)	3.01/2.71(S) 2.58/2.36(P)	10.44/9.84(S) 10.55/9.73(P)	1.42~1.63(S) 1.37~1.65(P)	3.83(HSE) 3.0(PBE)
FAGeCl ₃	8.24	2.21(S) 1.67(P)	2.84/2.32(S) 2.42/2.12(P)	10.10/9.06(S) 9.93/9.01(P)	1.50~1.94(S) 1.55~1.95(P)	4.11(HSE) 3.19(PBE)
FAGeBr ₃	7.68	2.21(S) 1.67(P)	3.00/2.54(S) 2.54/2.25(P)	10.41/9.50(S) 10.24/9.40(P)	1.41~1.76(S) 1.45~1.78(P)	3.75(HSE) 2.93(PBE)
FAGeI ₃	7.04	2.21(S) 1.67(P)	3.14/2.84(S) 2.65/2.44(P)	10.70/10.10(S) 10.70/9.97(P)	1.34~1.54(S) 1.33~1.57(P)	2.5(HSE) 1.98(PBE)
FAGe(BH ₄) ₃	7.02	2.21(S) 1.67(P)	2.95/2.56(S) 2.53/2.27(P)	10.32/9.54(S) 10.37/9.44(P)	1.47~1.77(S) 1.43~1.79(P)	4.49(HSE) 3.5(PBE)

^aExperimental values from Ref. 16.

^bExperimental values from Ref. 17.

^cExperimental value from Ref. 18.

^dExperimental values from Ref. 8.

^eDerived from the PBE value and the GW value of the material at its high-temperature cubic phase (*Pm-3m*) [6], by assuming that the GW correction to the band gaps obtained from PBE is the same for different phases of the material [17].

^fExperimental values from Ref. 5.

As shown in Table S11, the ionic radii of super-halogens in their pyramidal forms are significantly smaller than their radii in the symmetric form. By assuming the cation radii change little, this leads to larger radius ratio in the low-symmetry phase of the material. According to our model, this corresponds to larger band gaps compared to the high-symmetry phase, as shown in Table S13 for both Shannon-type and Pauling-type radii. Different hybrid perovskites may show different phases under the same ambient condition. For example, both MASnBr₃ and MASnI₃ show the high-symmetry phases of tetragonal and cubic phases at room temperature, while MASnCl₃ shows the low-symmetry triclinic or monoclinic phase. Therefore, in order to compare the band gaps through materials, it is only fitting to represent the band gap of a material in a range with the value of the cubic phase as the lower bound and

the value of the low-symmetry phase (where the super-halogen is a pyramid with its three M-X bond lengths close to d_c) as the upper bound. Indeed, as observed in the available experiments and calculations, the cubic phase of a hybrid perovskite shows a smaller band gap compared to its low-symmetry phases.

VII. NBO analysis of the super alkali halides

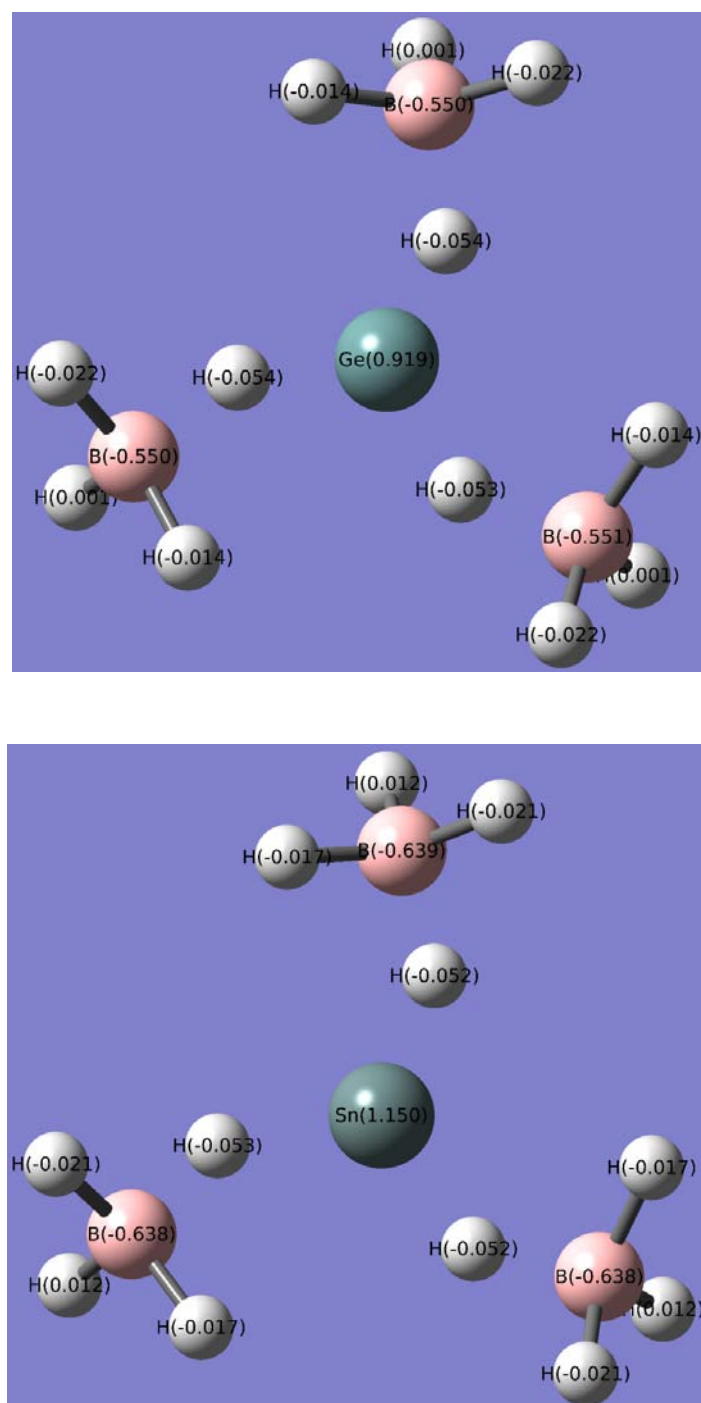
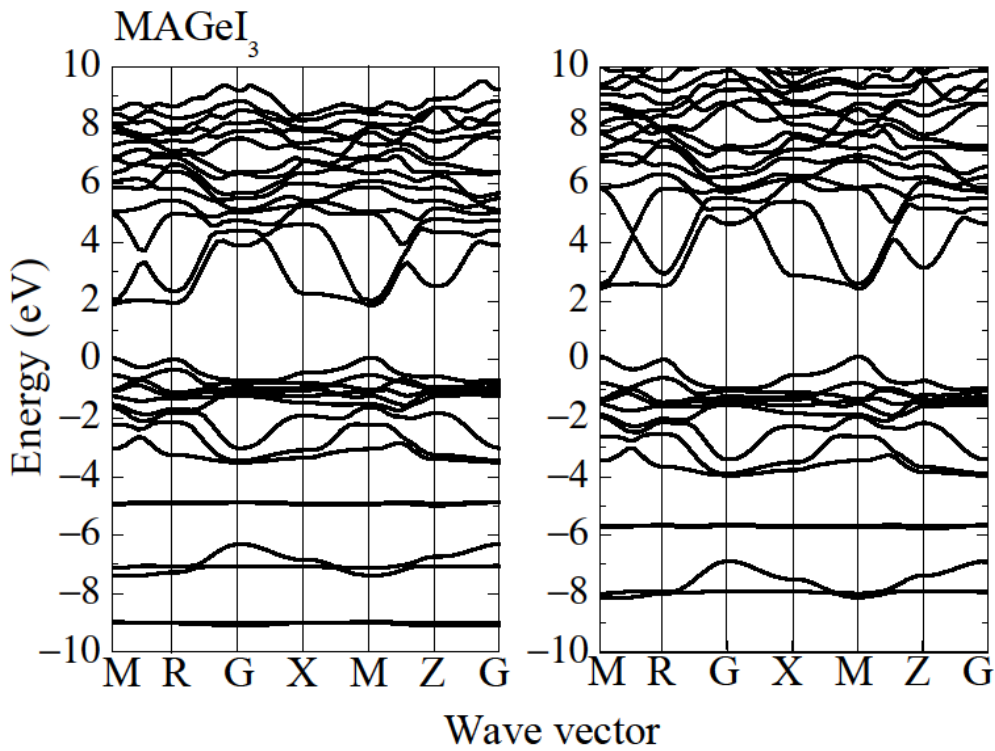
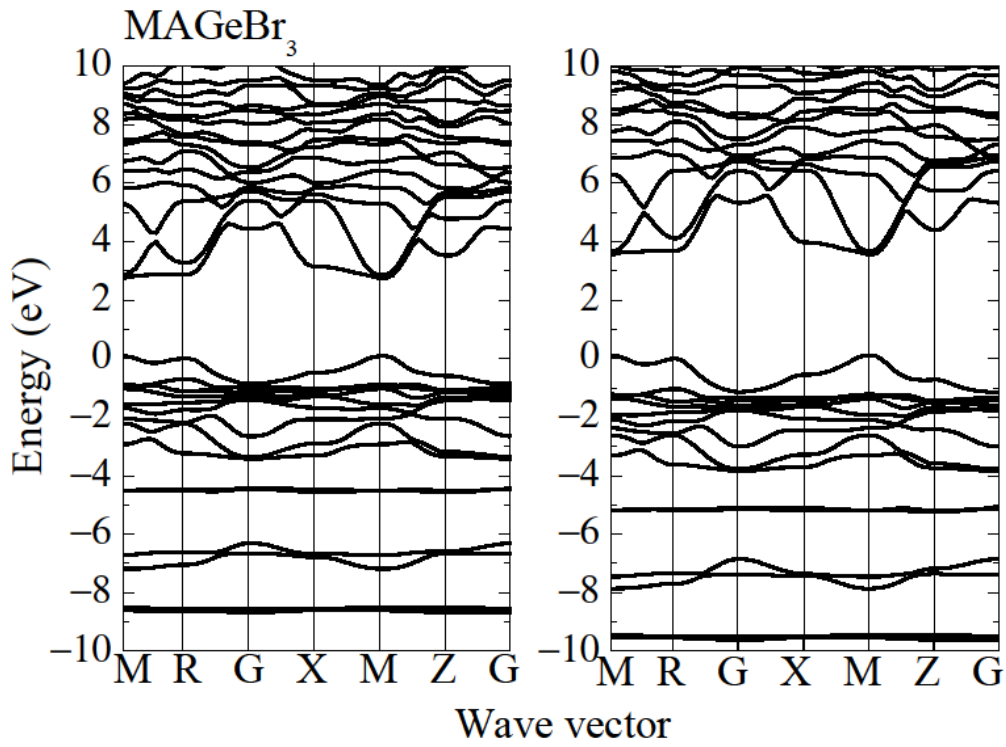
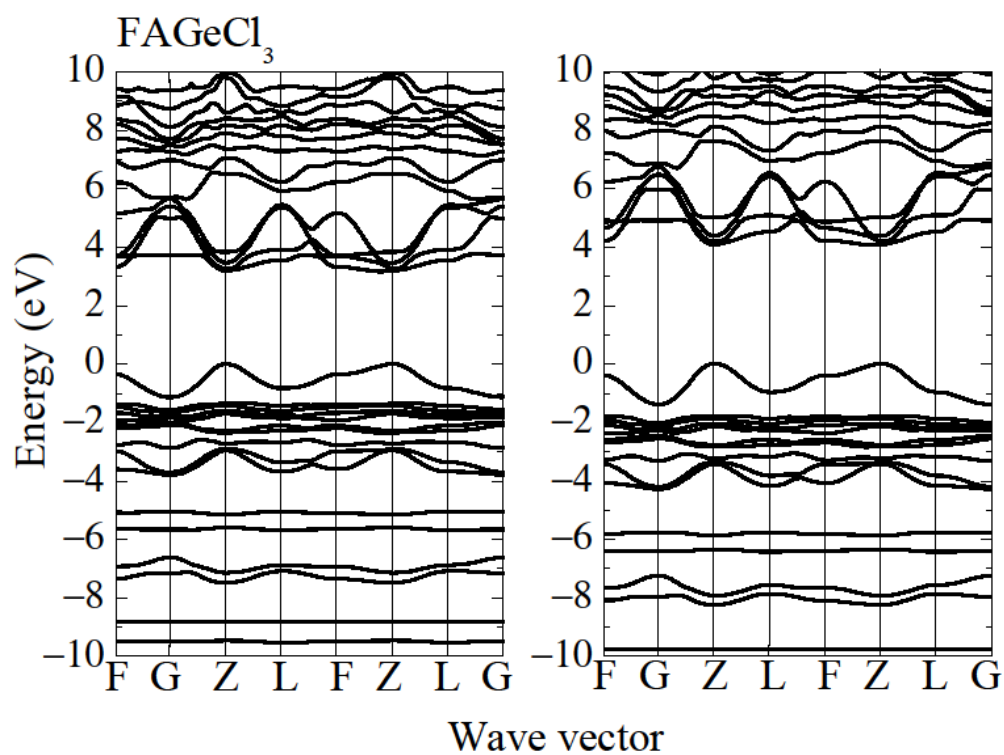
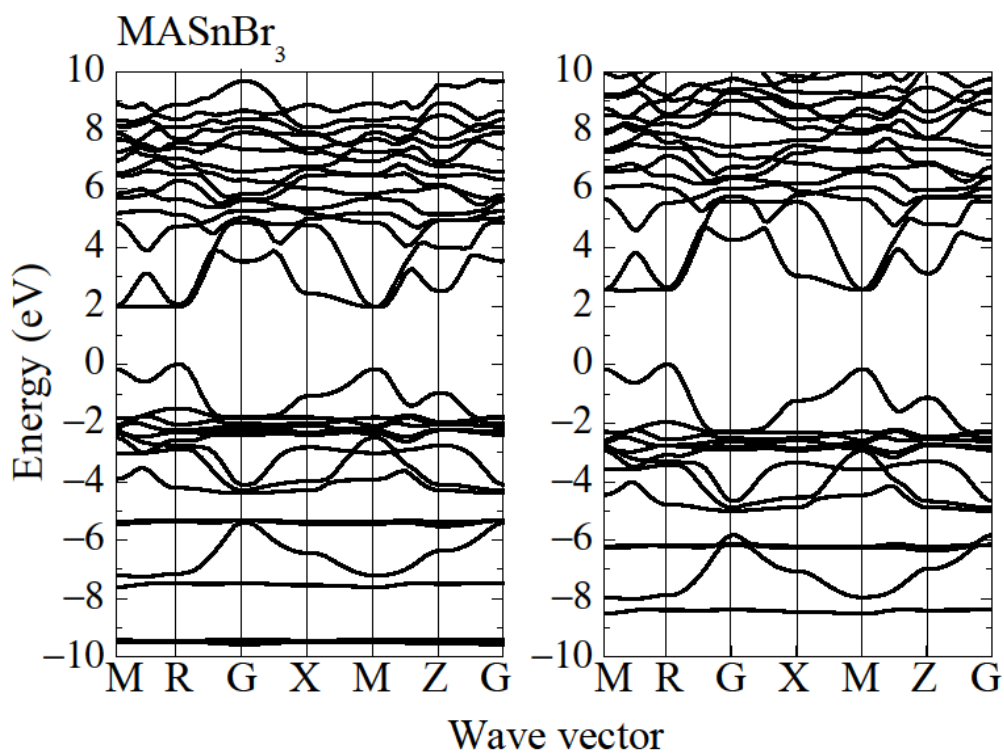
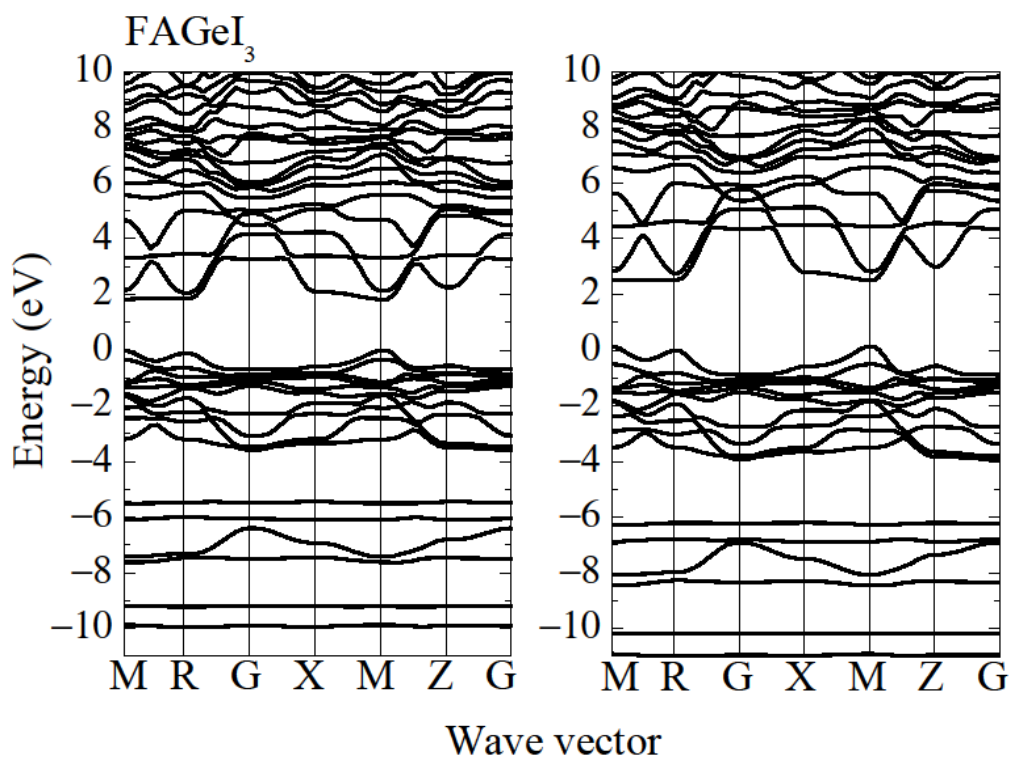
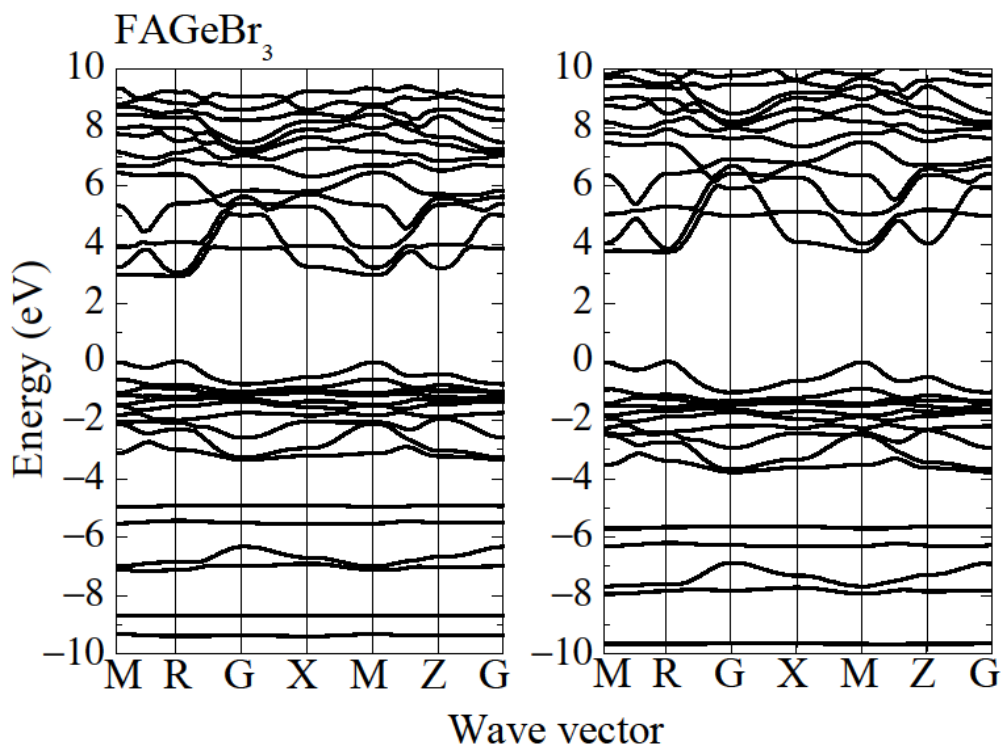


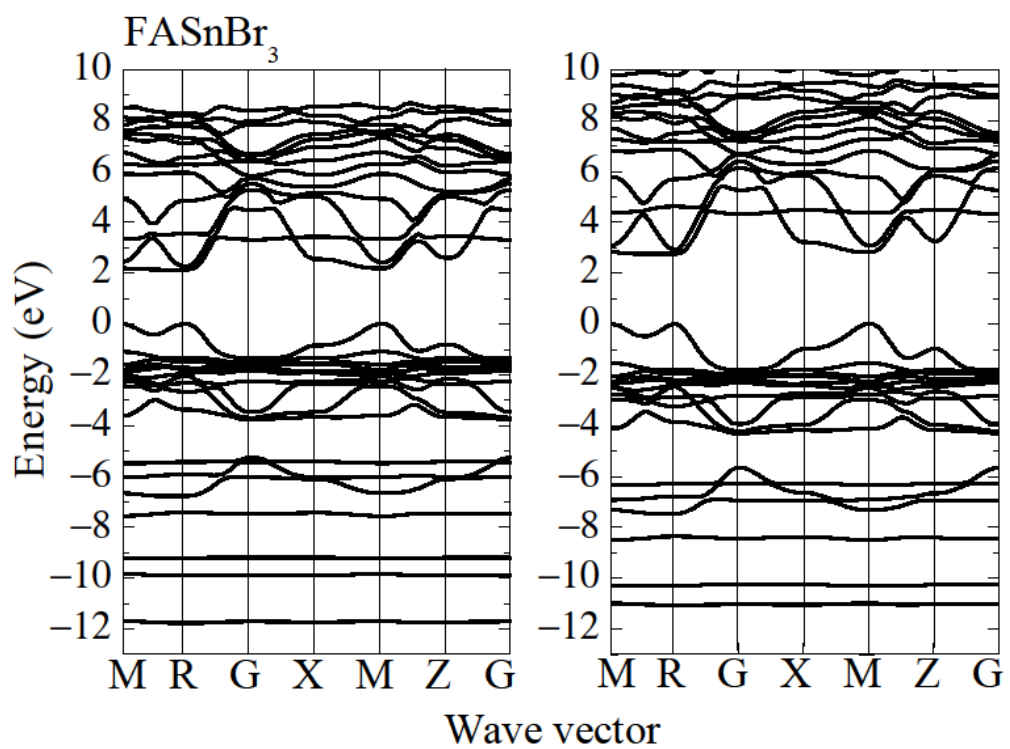
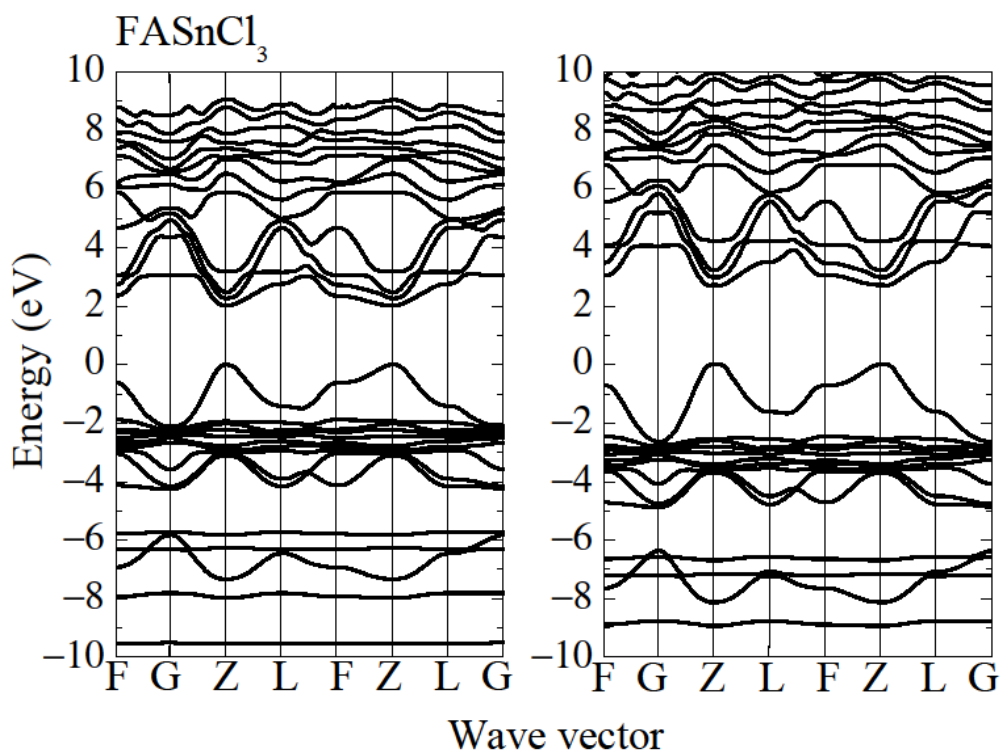
Fig. S11 NBO analysis of $[\text{Ge}(\text{BH}_4)_3]^-$ and $[\text{Sn}(\text{BH}_4)_3]^-$ hyper-halogens shows that the latter has larger bonding ionicity due to higher charge states although its radius ratio with the same cation is larger than the former.

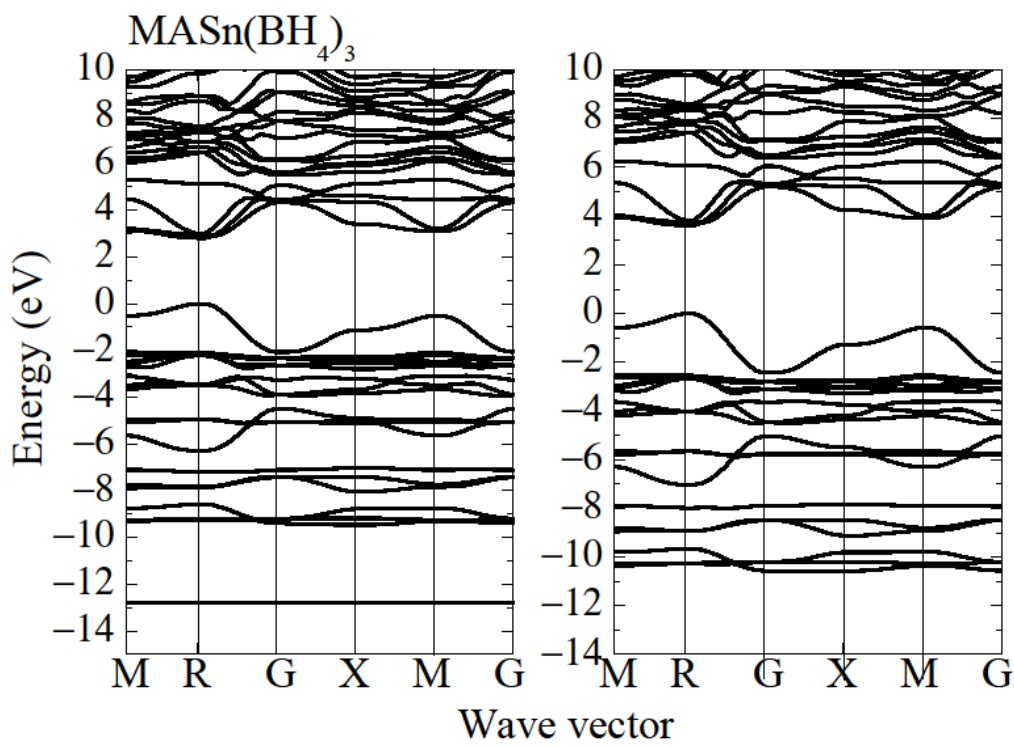
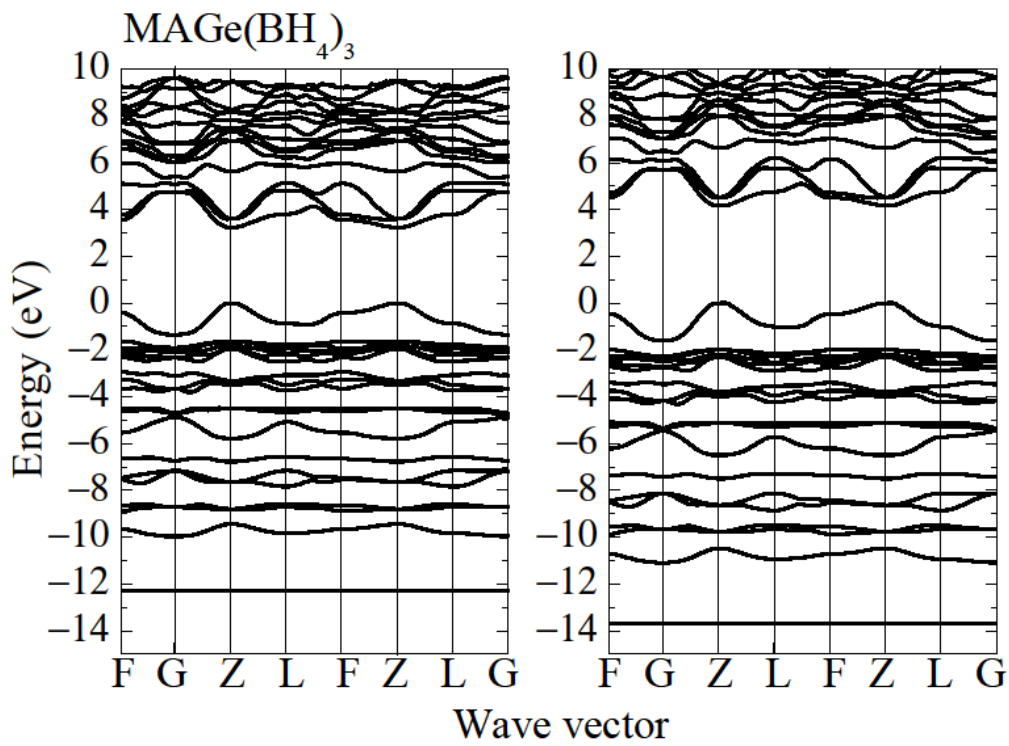
VIII. DFT calculated electronic band structures











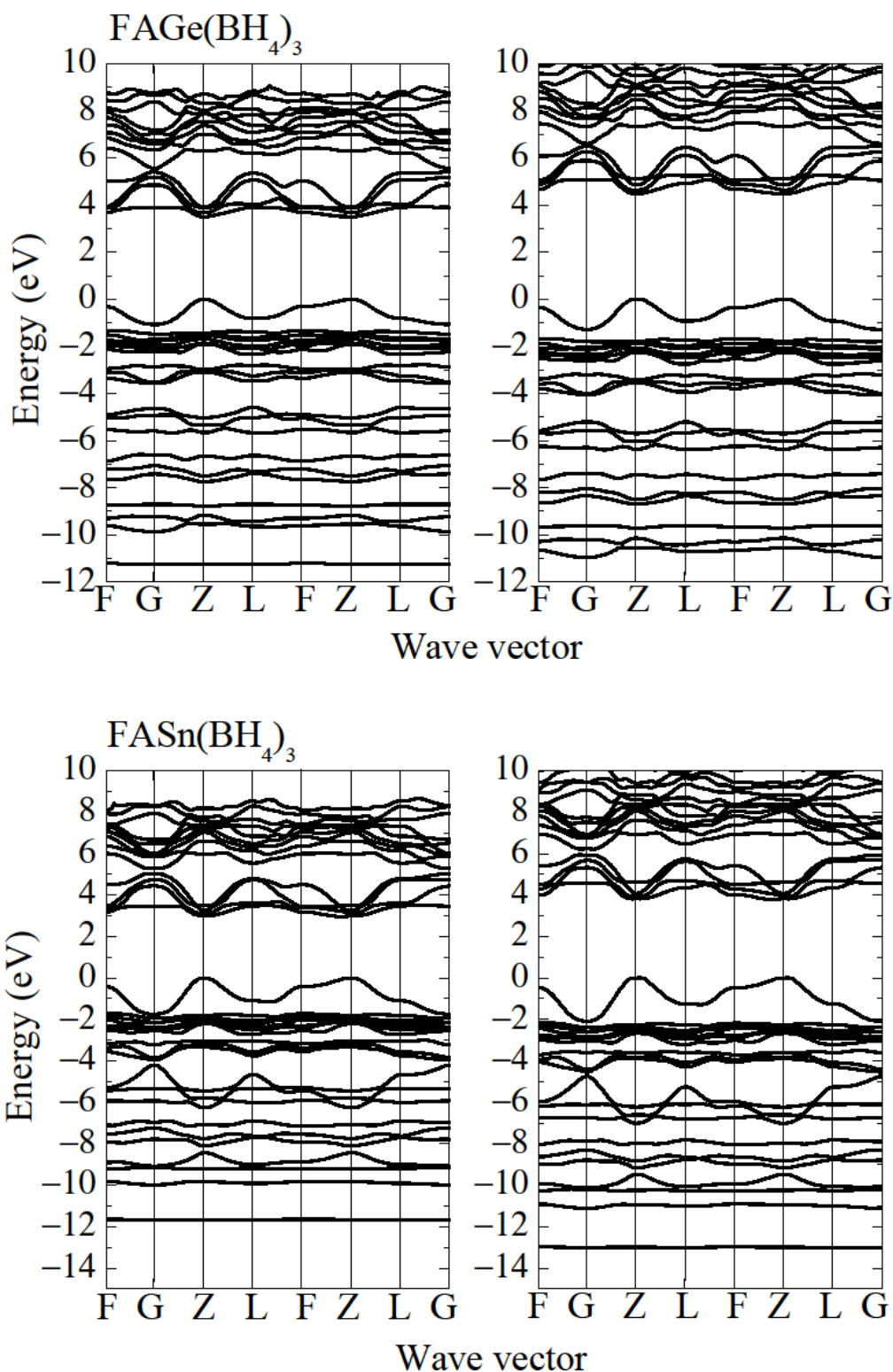
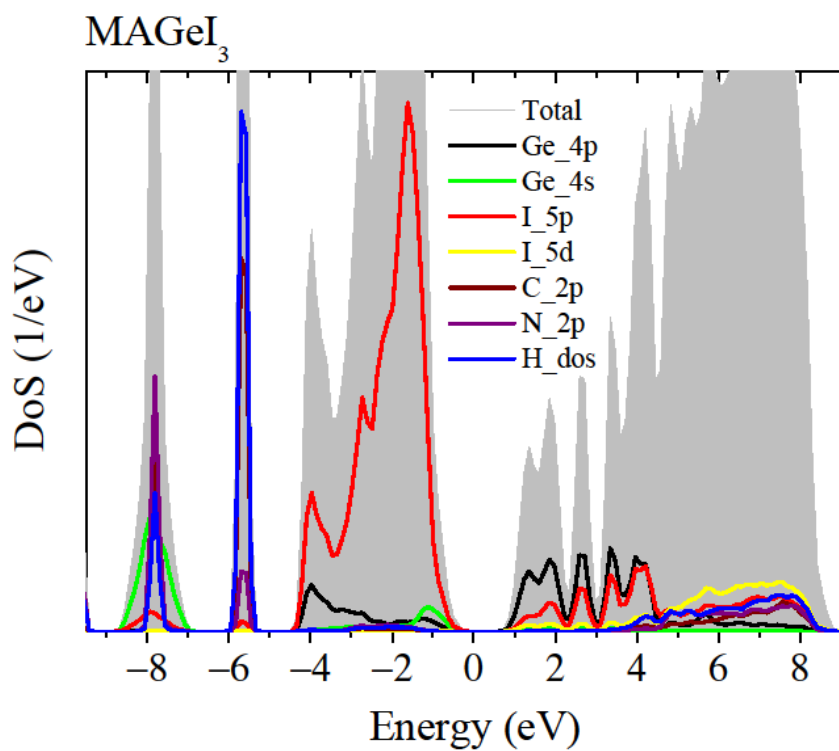
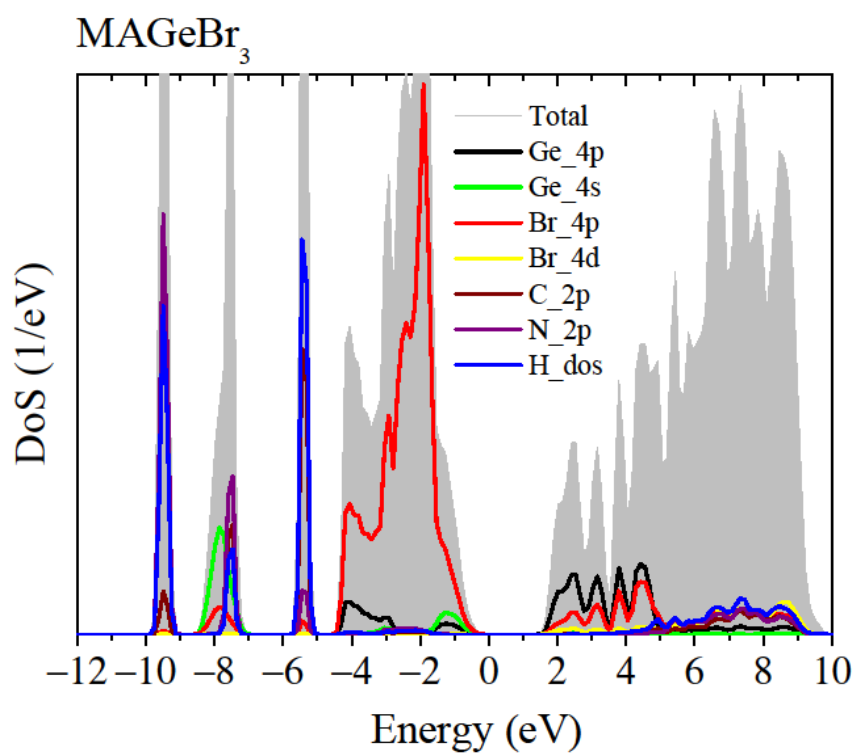
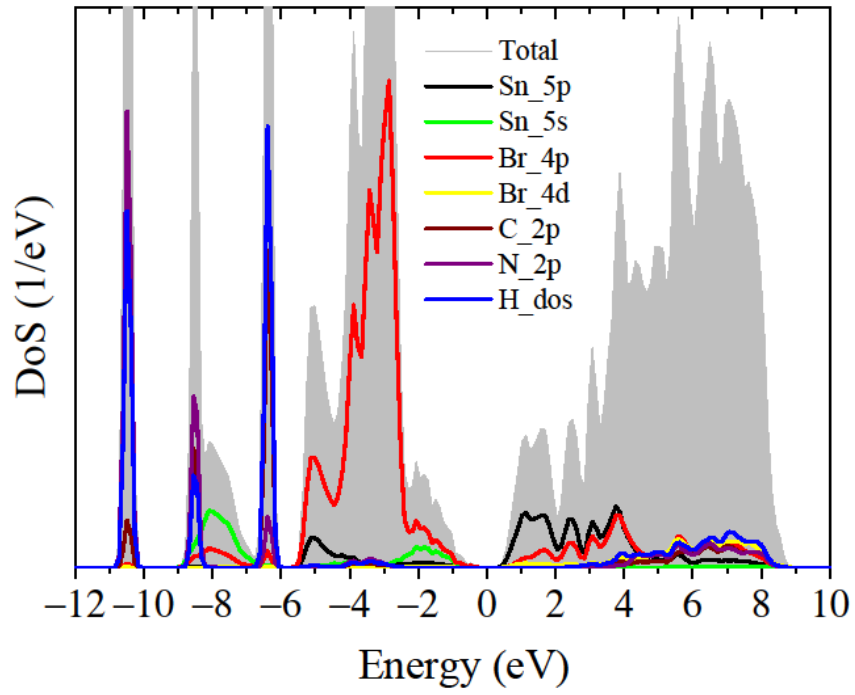


Fig. S12 DFT calculated electronic band structures of hybrid perovskites based on crystal structures obtained from the molecular dynamics simulations in Fig. S5 and relaxed ionic positions. The top of the valence band has been adjusted to zero energy in each case. All materials show direct band gaps. In each case, the left panel is from PBE calculation and the right panel is from HSE06 calculation. The "G" point in each case denotes the Γ point.

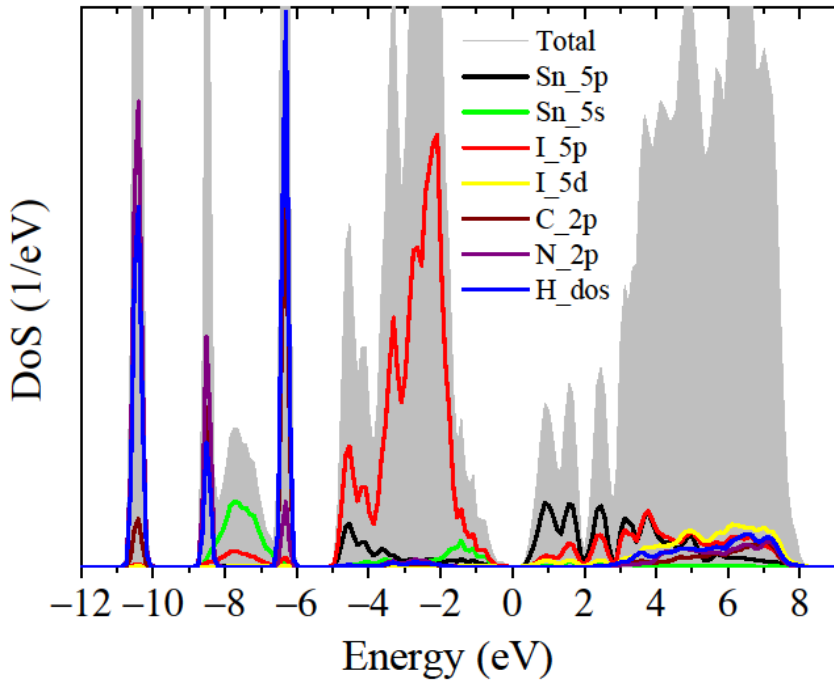
IX. DFT calculated electronic density of states



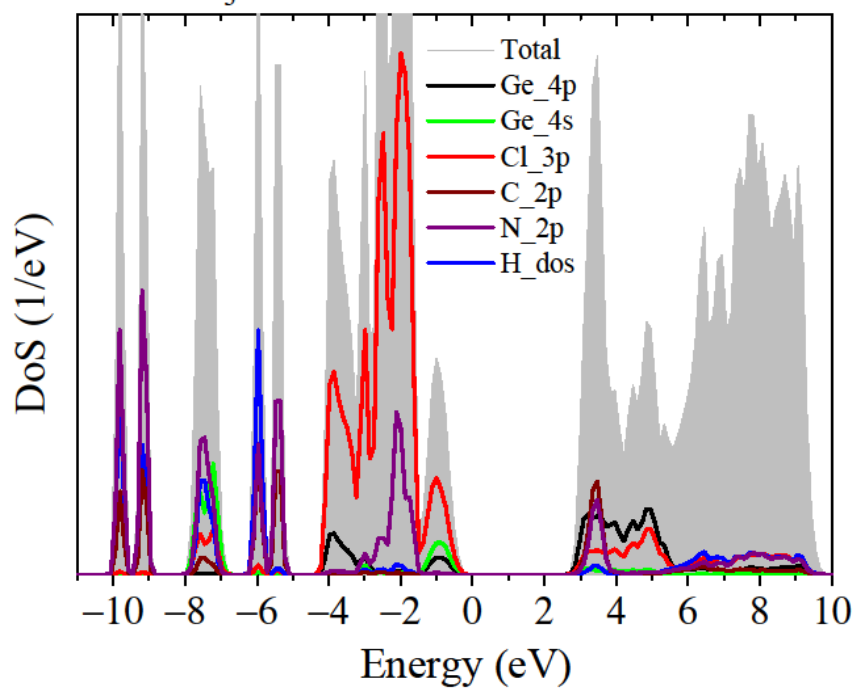
MASnBr₃



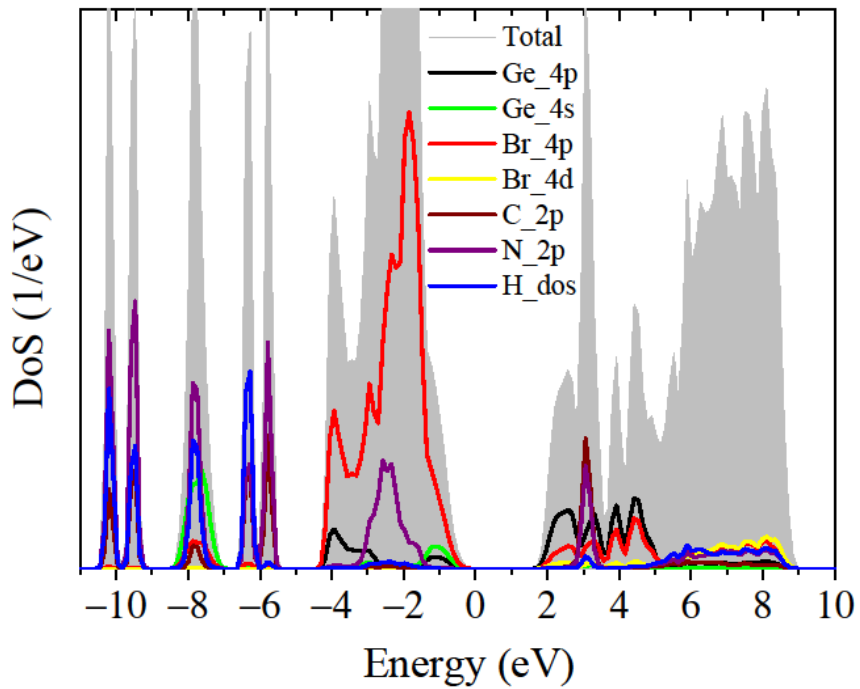
MASnI₃



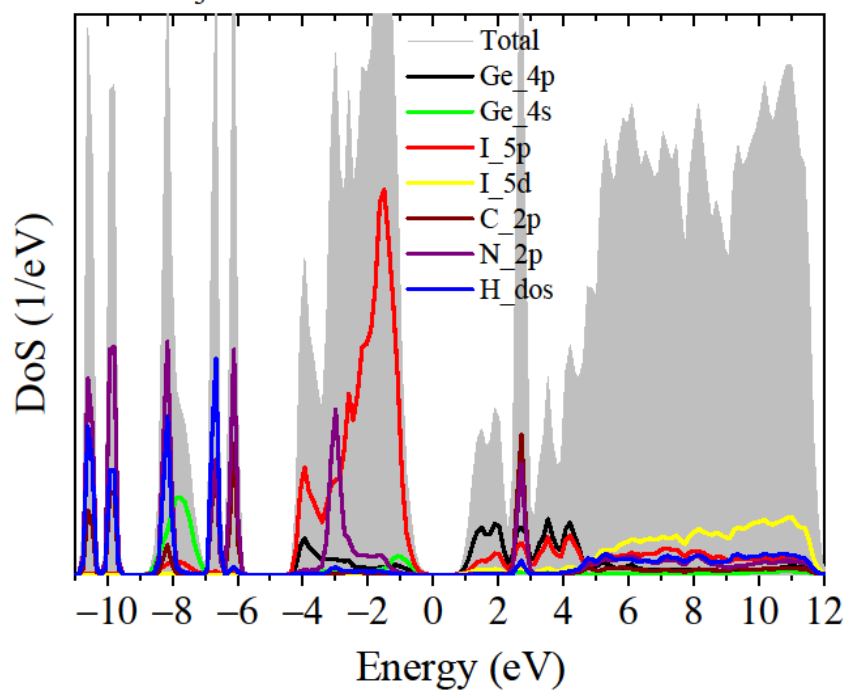
FAGeCl₃



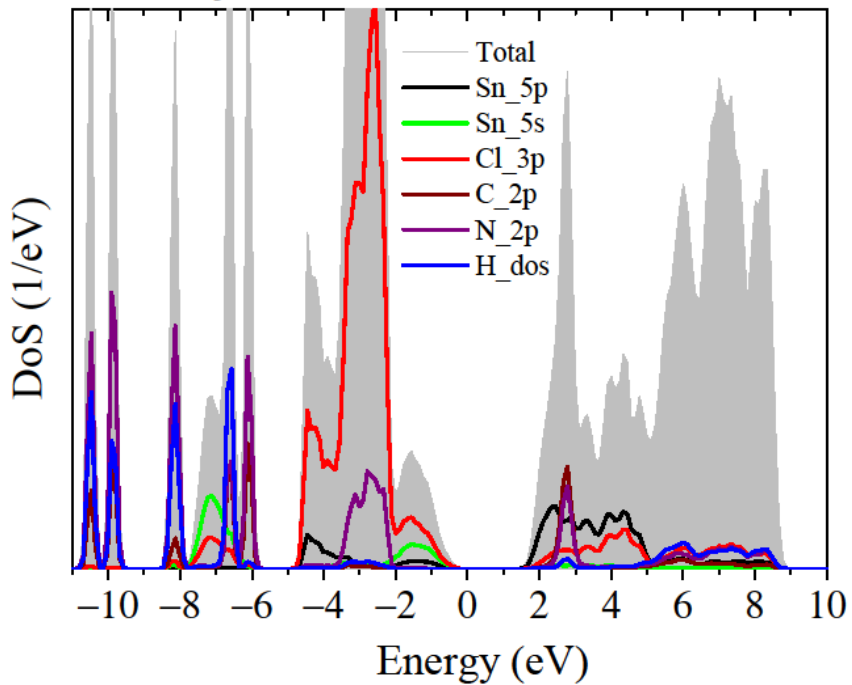
FAGeBr₃

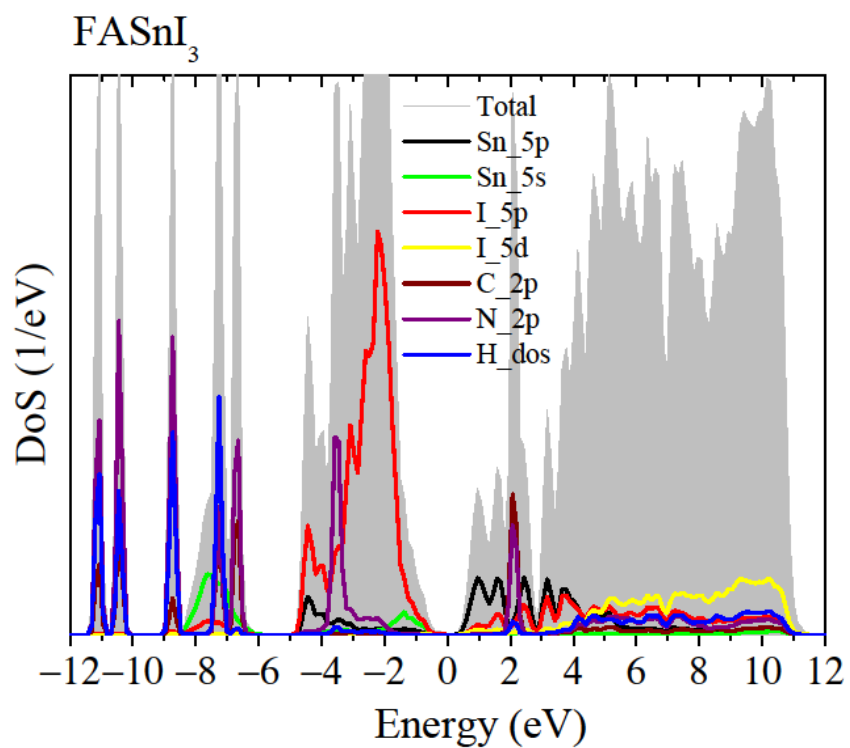
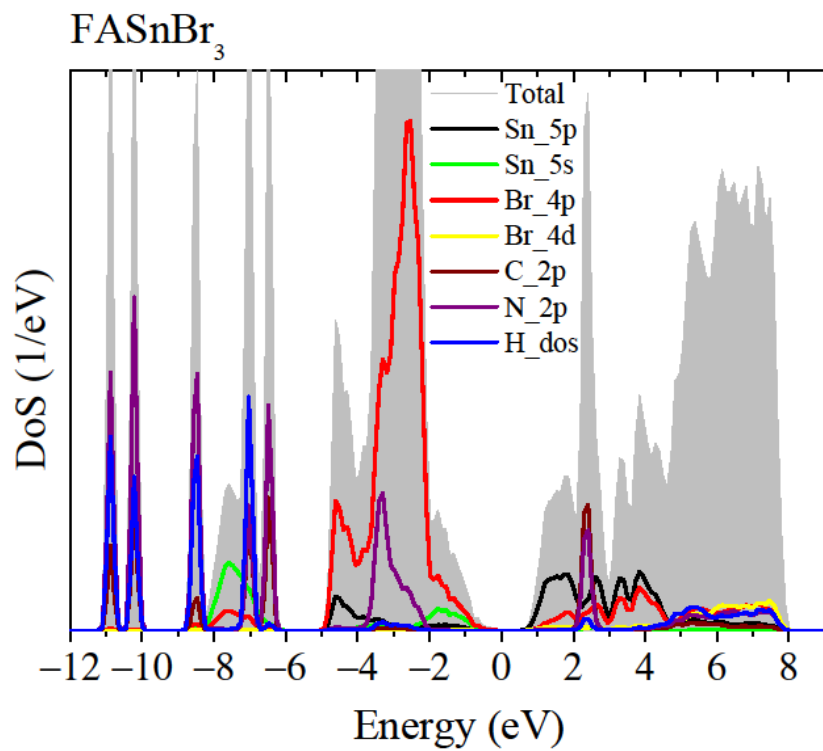


FAGeI₃

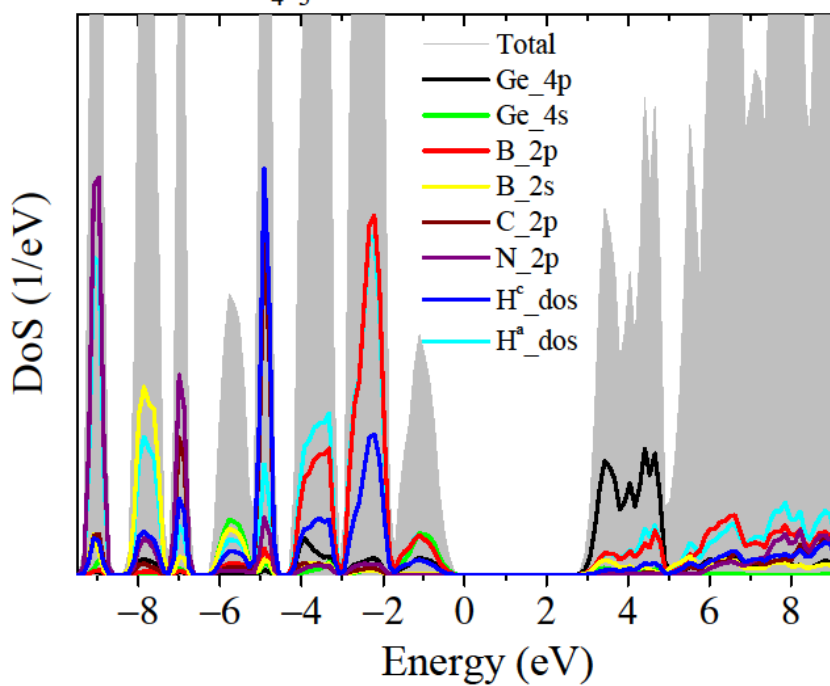


FASnCl₃

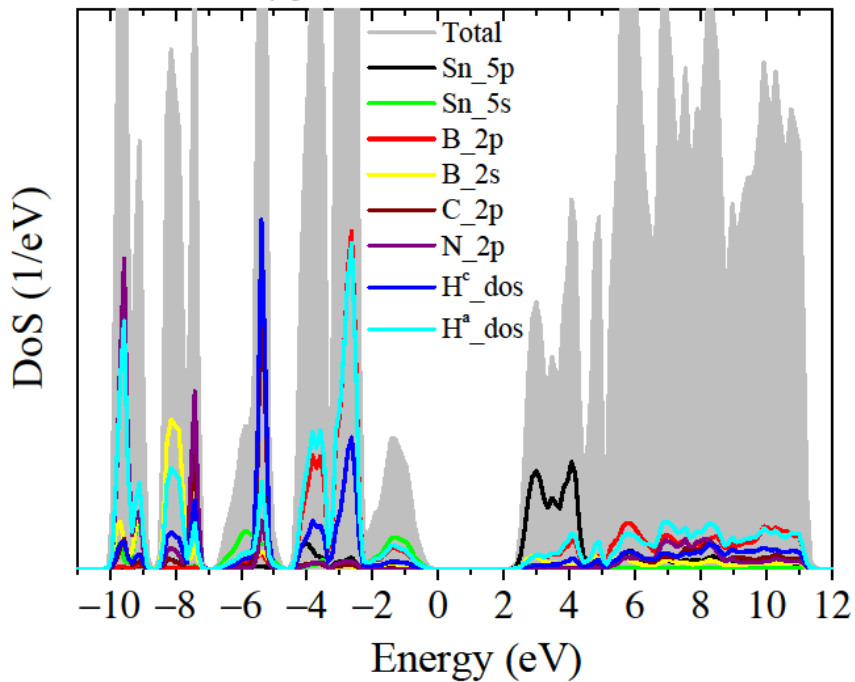


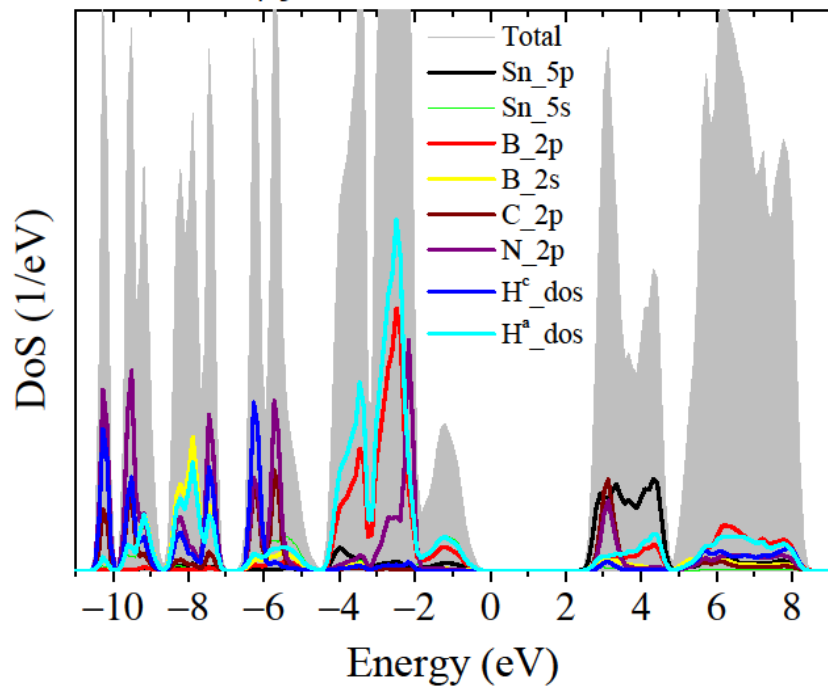
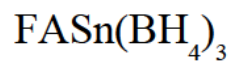
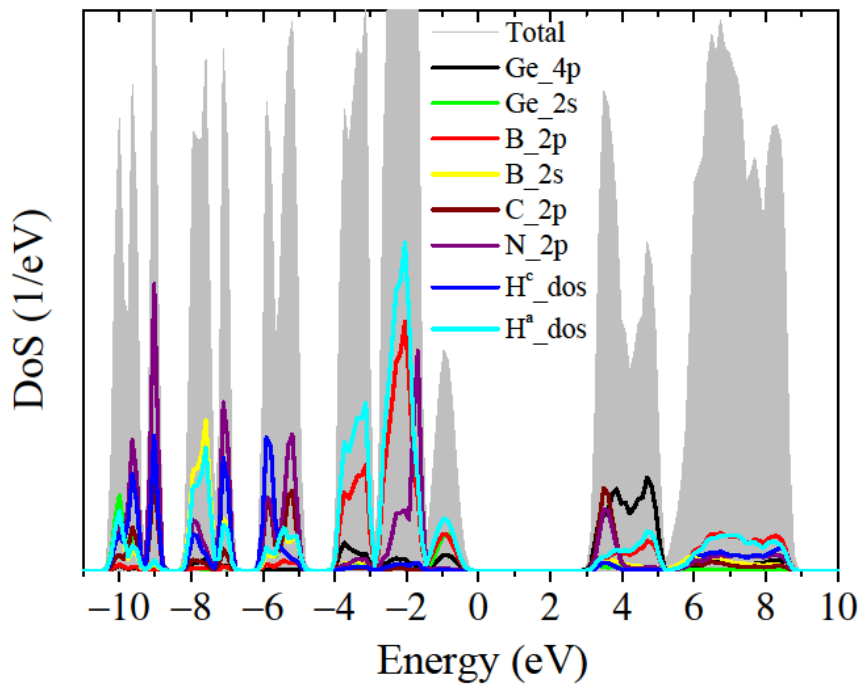
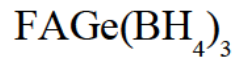


MAGe(BH₄)₃

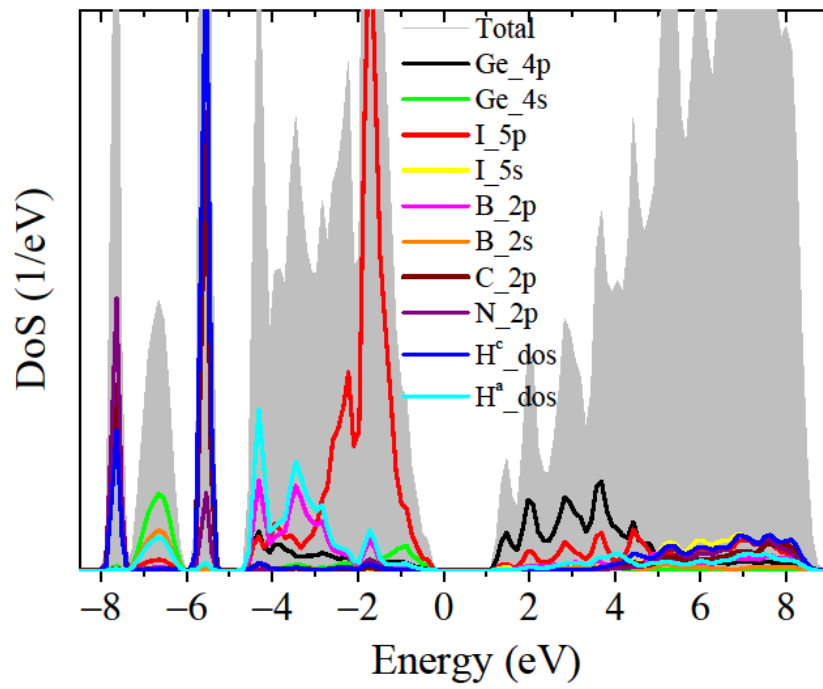


MASn(BH₄)₃

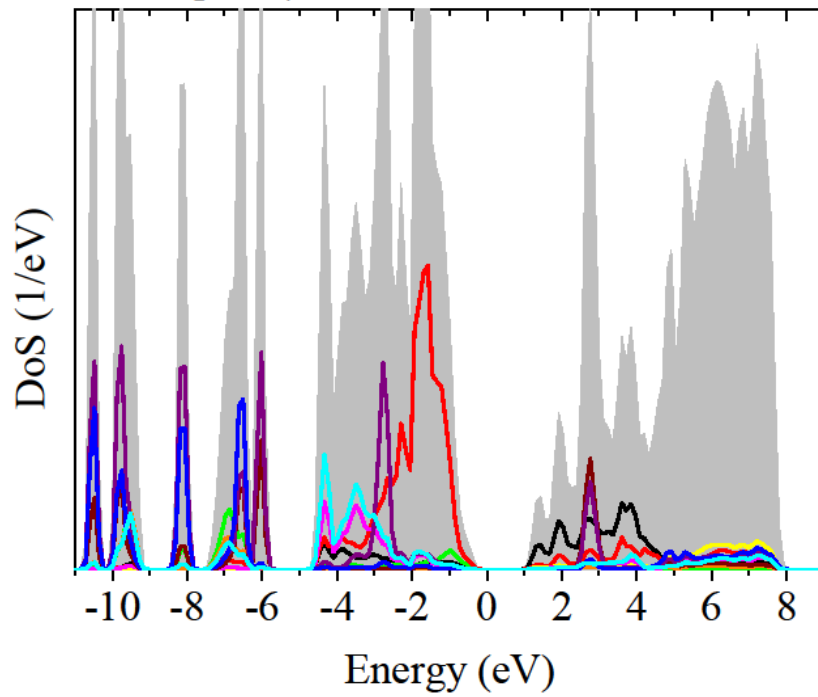




MAGeI₂(BH₄)



FAGeI₂(BH₄)



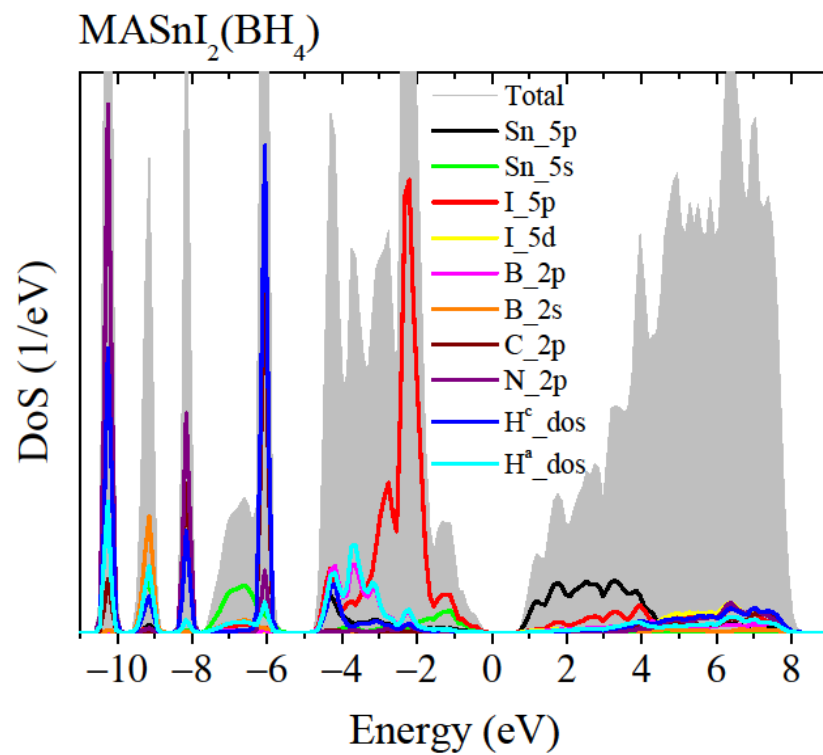


Fig. S13 DFT-PBE calculated electronic density of states (DoS). In each case, partial DoS analysis has been carried out. The top of the valance band is at zero energy. “H_dos” stands for the total density of states of the hydrogen. “H^c_dos” stands for the total density of states of the hydrogen associated with the cation. “H^a_dos” stands for the density of states from the hydrogen associated with the anion.

X. Phonon calculations of $\text{MAGe}(\text{BH}_4)_3$ and $\text{MASn}(\text{BH}_4)_3$

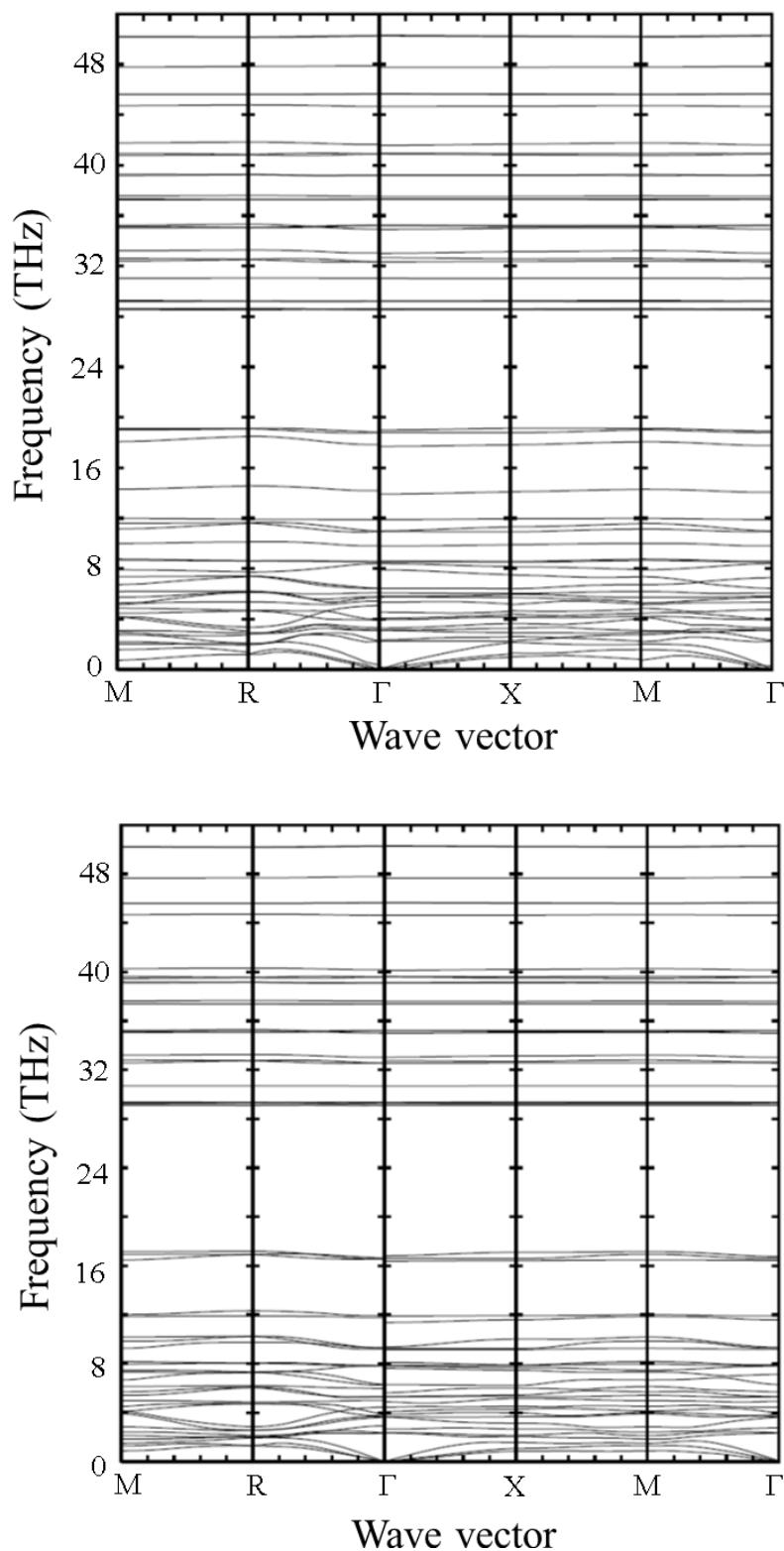
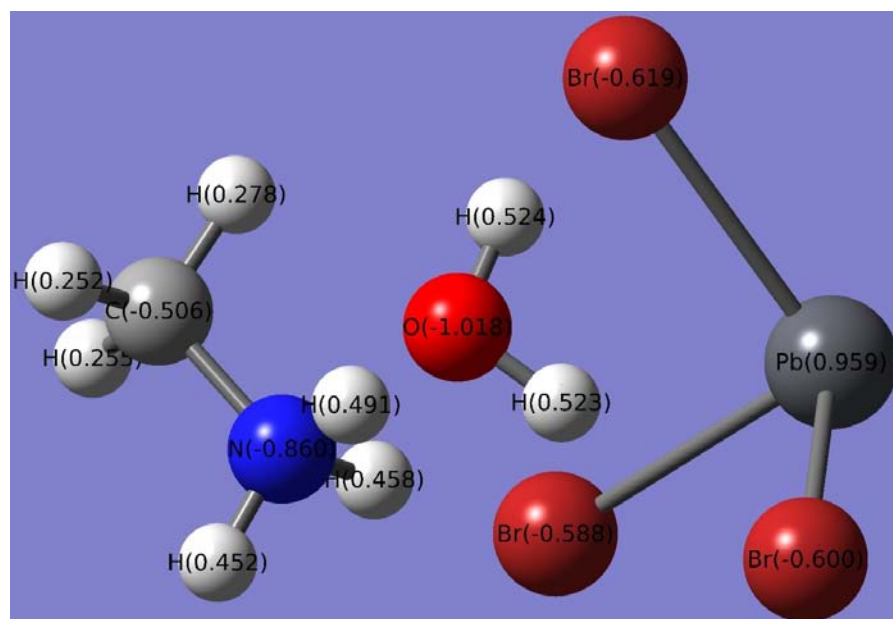
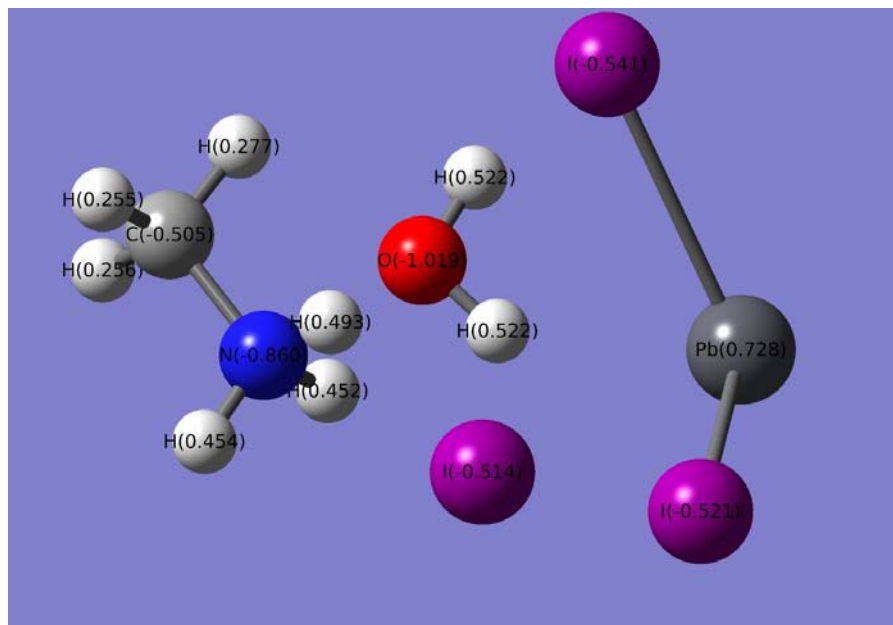


Fig. S14 Calculated phonon dispersions of $\text{MAGe}(\text{BH}_4)_3$ (upper) and $\text{MASn}(\text{BH}_4)_3$ based on crystal structures obtained from the molecular dynamics simulations under ambient condition and optimized ionic positions. MA stands for CH_3NH_3 .

XI. Stability analyses of the hybrid perovskite under moisture



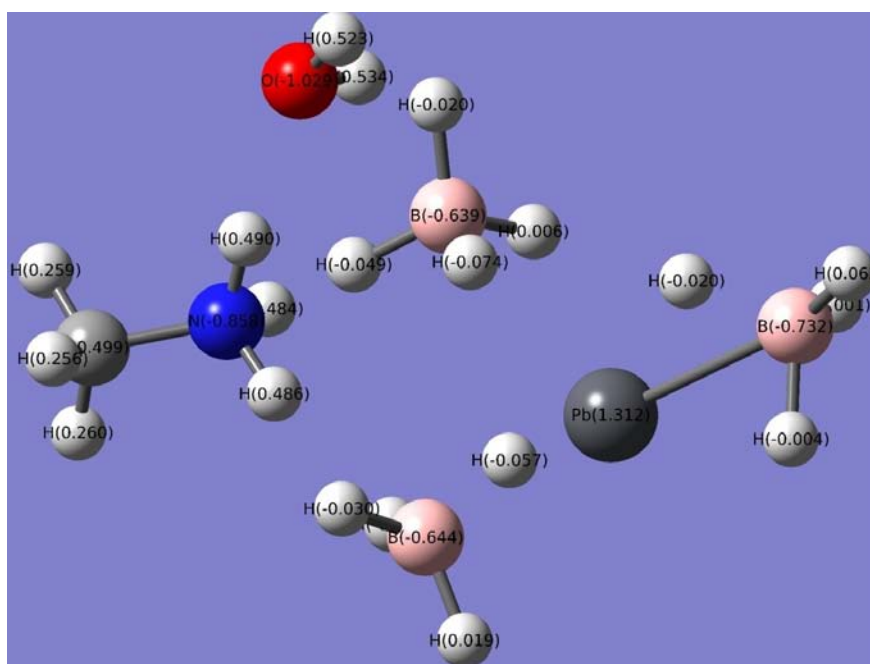
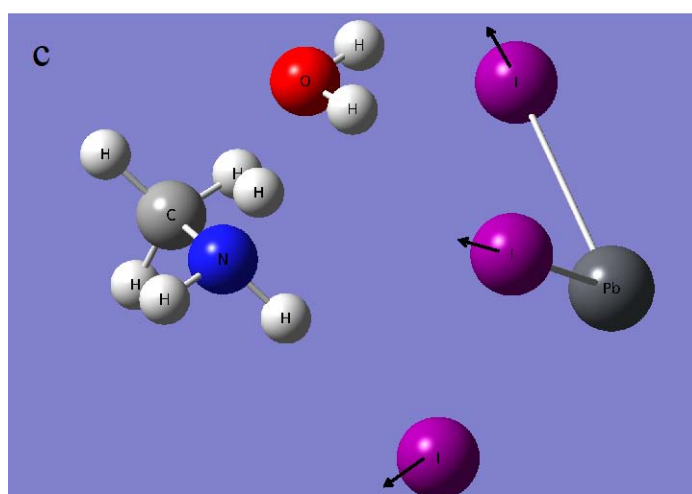
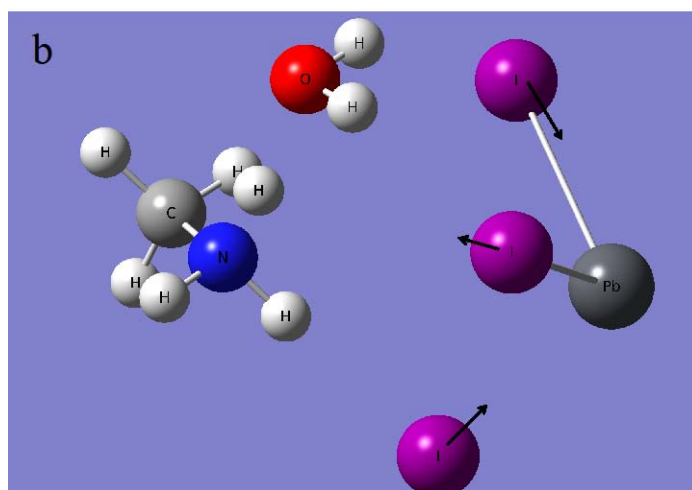
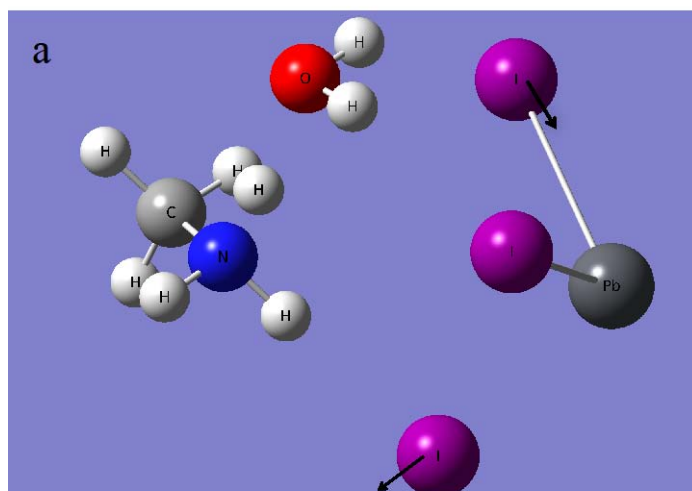


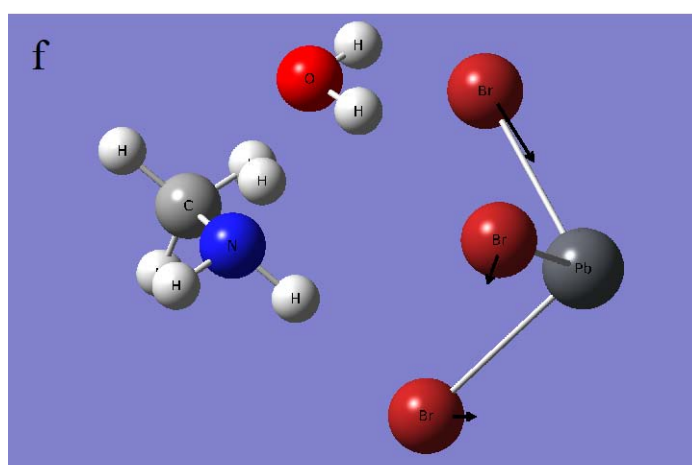
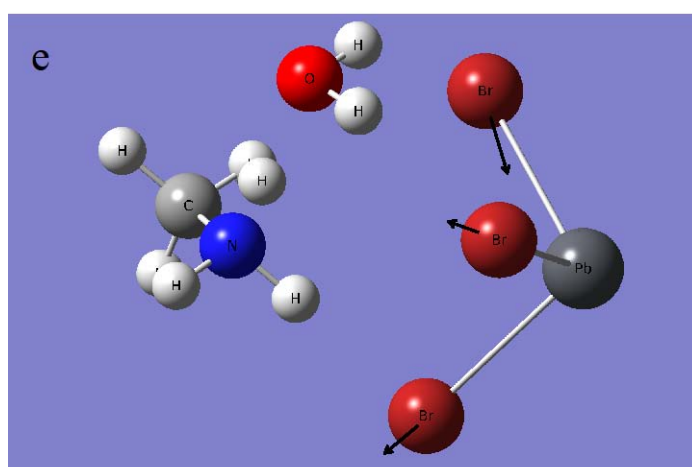
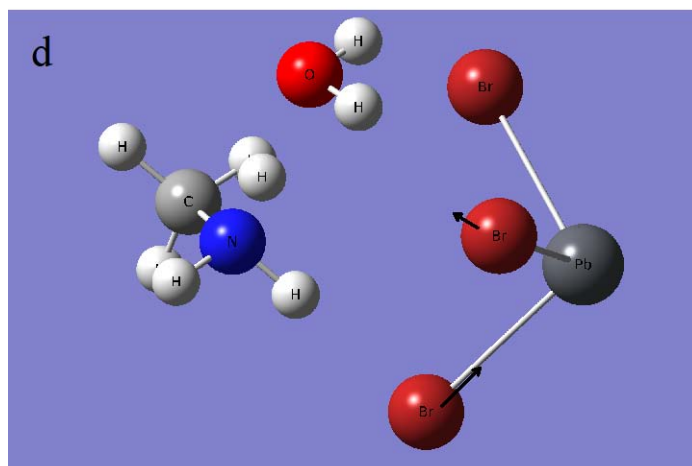
Fig. S15 NBO analysis for MAPbI₃, MAPbBr₃ and MAPb(BH₄)₃ super-salts bound to a water molecule. MA stands for CH₃NH₃.

Table S14 Calculated binding energy between various super-salts and a water molecule. The bond length of M-X within [MX₃]⁻ super-ion is the averaged value in the optimized structure with the water molecule. MA and FA stand for CH₃NH₃ and HC(NH₂)₂, respectively.

Cluster	Binding energy (eV)	Bond length of M-X (Å)
MAGe(BH ₄) ₃	0.652	2.68
MAGeCl ₃	0.711	2.38
MAGeBr ₃	0.694	2.54
MAGeI ₃	0.705	2.78
MASn(BH ₄) ₃	0.600	2.72
MASnCl ₃	0.763	2.56
MASnBr ₃	0.731	2.71
MASnI ₃	0.731	2.95
MAPb(BH ₄) ₃	0.593	2.76
MAPbBr ₃	0.782	2.80
MAPbI ₃	0.670	3.03
FA ⁺	0.709	—
MA ⁺	0.824	—
[Li ₃ O] ⁺	0.996	—

XII. Vibrational spectra of super halide molecule with water





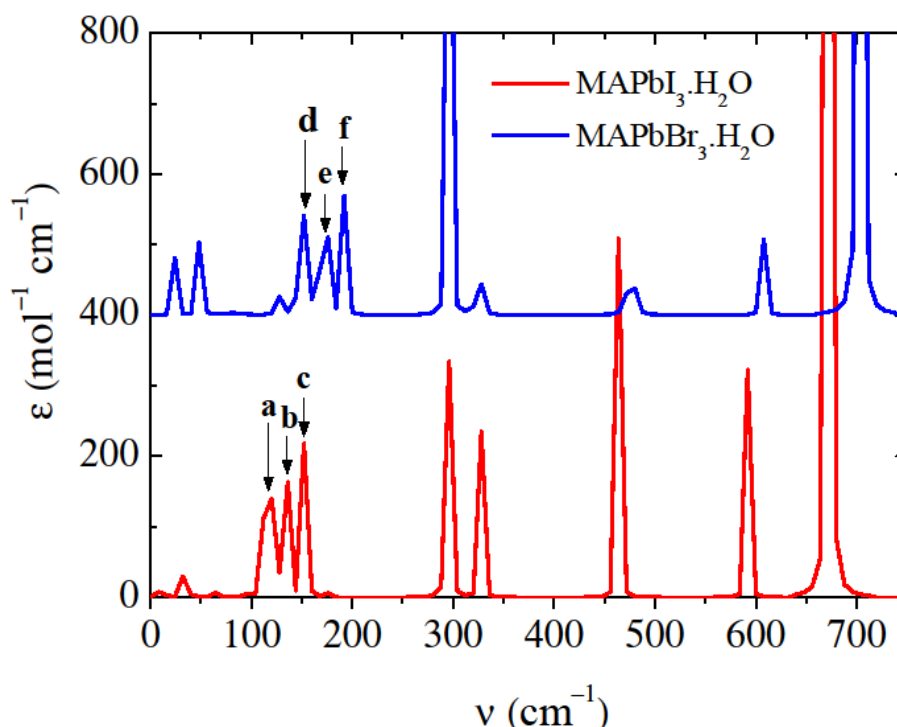


Fig. S16 Simulated infrared spectra of molecules MAPbI_3 and MAPbBr_3 with one water molecule binding to them. MA stands for CH_3NH_3 . The vibration modes involving the bond stretching of Pb-I and Pb-Br are indicated by the arrows in the plot. The Pb-Br bond shows significantly higher frequencies (148.15, 153.15 and 165.43 cm^{-1}) of these modes than the Pb-I bond (112.40, 113.62 and 128.79 cm^{-1}). The corresponding displacements of the iodine and bromine are shown schematically in the figures **a** to **f**, respectively.

XIII. Inorganic super alkali $[\text{Li}_3\text{O}]^+$

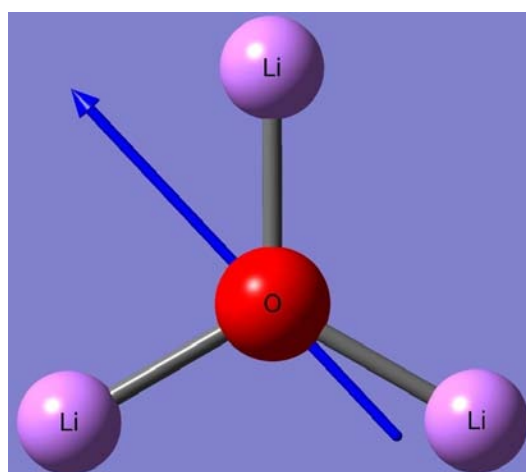


Fig. S17 Planer inorganic super-alkali $[\text{Li}_3\text{O}]^+$. In its asymmetric configuration, it has an intrinsic dipole moment of 29.40 Debye as indicated by the blue arrow originating from the center of electronic charge. However, with symmetric constraint during the optimization, the dipole moment becomes zero.

XIV. Electronic structures of the hybrid perovskites composed of hyper halogens

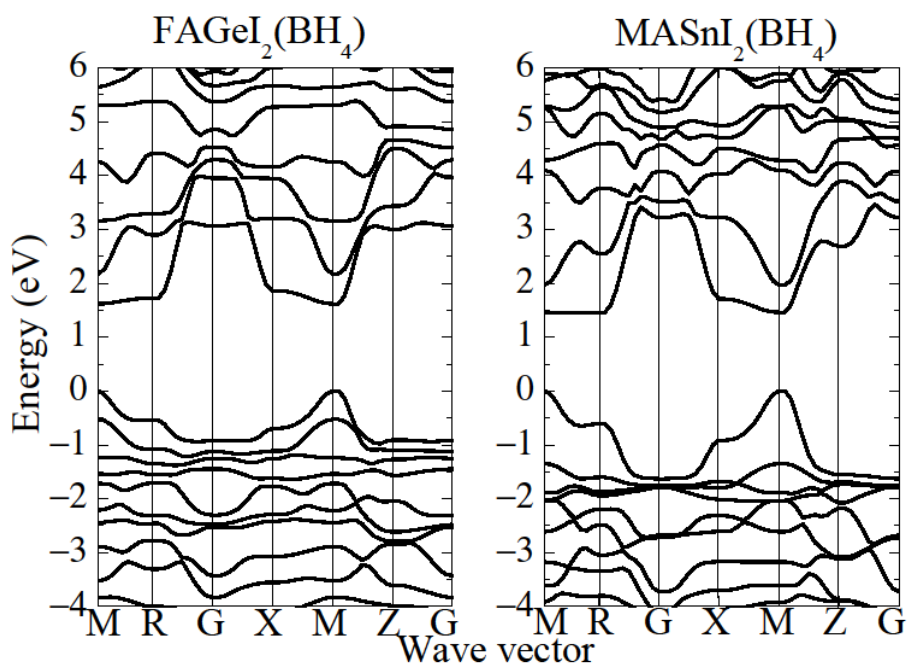


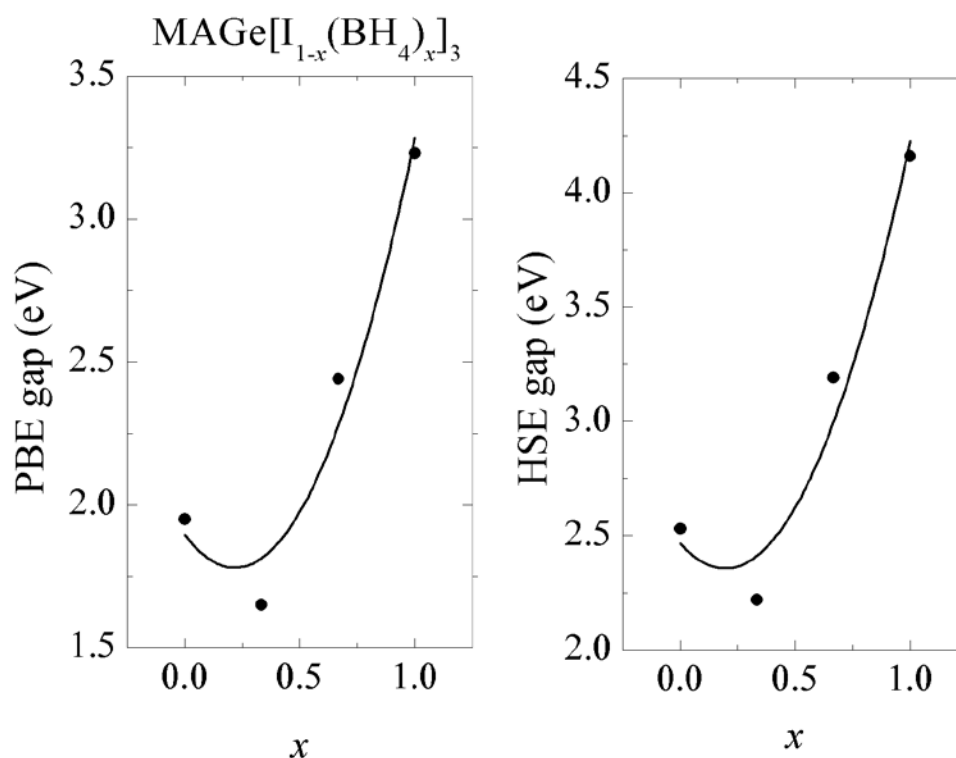
Fig. S18 DFT-PBE calculated electronic bands of newly-designed hybrid perovskites with iodine partially replaced by super halogen $[BH_4]^-$. MA and FA stand for CH_3NH_3 and $HC(NH_2)_2$, respectively. This indicates that $MASnI_2(BH_4)$ should have smaller band gap than $FGeI_2(BH_4)$. The lattice parameters of $[MA/FA][Ge/SnI_3]$ are used with relaxed positions of the ions. The "G" point in each case denotes the Γ point.

XV. Bowing factors of $\text{AM}[\text{I}_{1-x}(\text{BH}_4)_x]_3$ (A = MA and FA; M = Ge and Sn; $x = 0, 1/3, 2/3, 1$) from band gaps

Table S15 DFT calculated band gaps for $\text{AM}[\text{I}_{1-x}(\text{BH}_4)_x]_3$ (A = MA and FA; M = Ge and Sn, $x = 0, 1/3, 2/3, 1$) and the bowing factors from the polynomial fittings. MA and FA denote CH_3NH_3 and $\text{HC}(\text{NH}_2)_2$, respectively. In each case, the value is from DFT-PBE result and the value in the bracket corresponds to the HSE result.

	Direct band gap at x (eV)				Bowing Factor (eV)
	0	0.333	0.667 ^a	1	
$\text{MAGe}[\text{I}_{1-x}(\text{BH}_4)_x]_3$	1.95 (2.53)	1.65 (2.22)	2.44 (3.19)	3.23 (4.16)	2.45 (2.88)
$\text{FAGe}[\text{I}_{1-x}(\text{BH}_4)_x]_3$	1.98 (2.50)	1.62 (2.17)	2.54 (3.31)	3.50 (4.49)	2.97 (3.39)
$\text{MASn}[\text{I}_{1-x}(\text{BH}_4)_x]_3$	1.58	1.46	2.28	2.80	1.44
$\text{FASn}[\text{I}_{1-x}(\text{BH}_4)_x]_3$	1.62	1.31	2.30	3.00	2.27

^aThe HSE band gaps are derived from the PBE values assuming corrections of 0.75 eV and 0.77 eV for $\text{MAGe}[\text{I}_{1/3}(\text{BH}_4)_{2/3}]_3$ and $\text{FAGe}[\text{I}_{1/3}(\text{BH}_4)_{2/3}]_3$, respectively. In each case, the correction is the averaged correction by comparing the HSE and PBE gaps of the two cases $x = 0.333$ and $x = 1$.



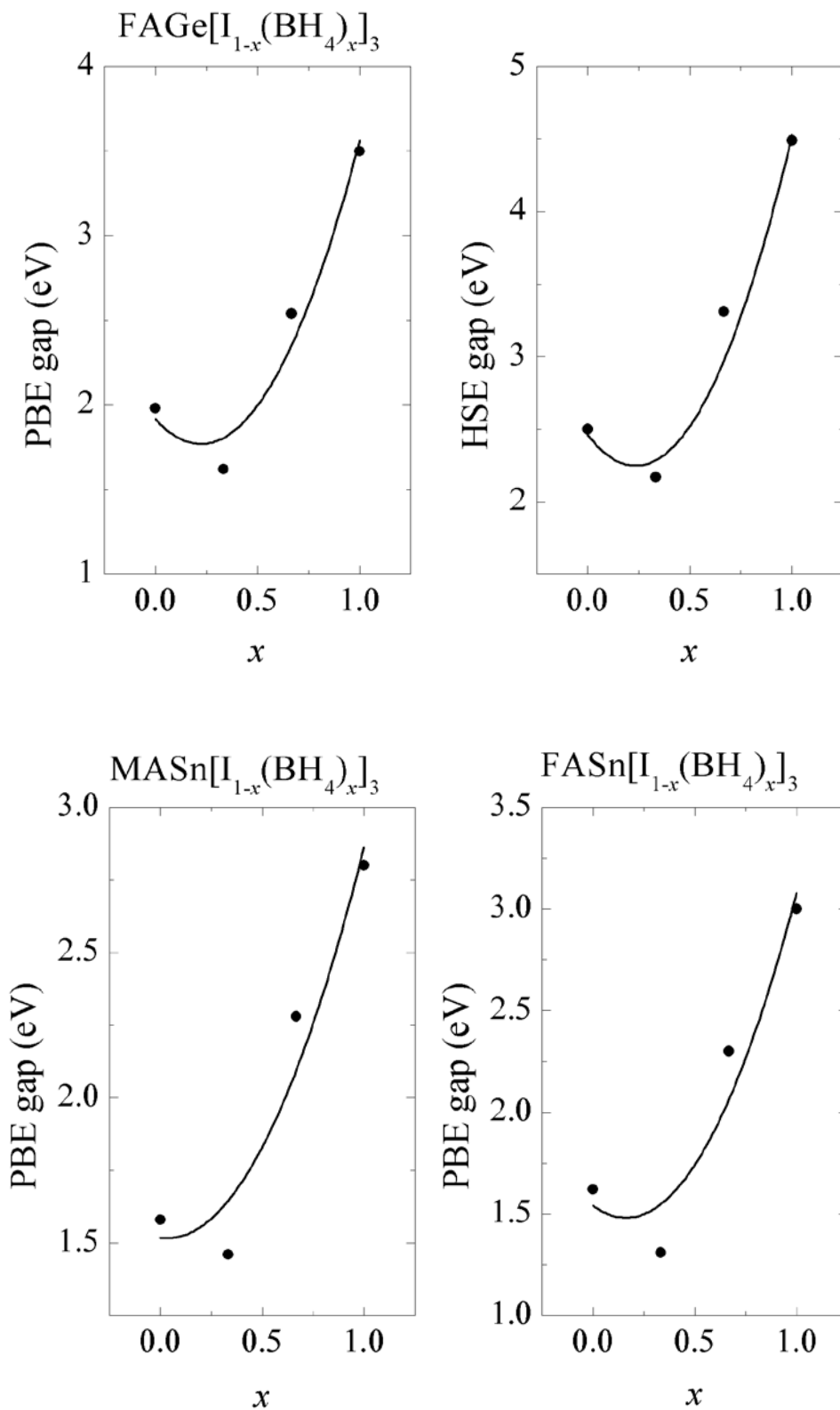


Fig. S19 DFT calculated band gaps (E_g) for the admixtures $AM[I_{1-x}(BH_4)_x]_3$ ($A = MA$ and FA ; $M = Ge$ and Sn , $x = 0, 1/3, 2/3, 1$). In each case, the bowing factor (b) is obtained by fitting the data points using a polynomial $E_g(x) = E_0 + ax + bx^2$.

References

1. Jena, P. Beyond the periodic table of elements: The role of superatoms. *J. Phys. Chem. Lett.* 4, 1432 (2013).
2. Gilmore, R. *Elementary Quantum Mechanics in One Dimension* (The Johns Hopkins University Press, 2004).
3. Yamada, K., Mikawa, K., Okuda, T. and Knight, K. S. Static and dynamic structures of $\text{CD}_3\text{ND}_3\text{GeCl}_3$ studied by TOF high resolution neutron powder diffraction and solid state NMR. *J. Chem. Soc., Dalton Trans.*, 2112 (2002).
4. Yamada, K., Kuranaga, Y., Ueda, K., Goto, S., Okuda, T. and Furukawa, Y. Phase transition and electric conductivity of ASnCl_3 ($A = \text{Cs}$ and CH_3NH_3). *Bull. Chem. Soc. Jpn.*, 71, 127 (1998).
5. Stoumpos, C. C., Malliakas, C. D. and Kanatzidis, M. G. Semiconducting tin and lead iodide perovskites with organic cations: Phase transitions, high mobilities, and near-infrared photoluminescent properties. *Inorg. Chem.* 52, 9019 (2013).
6. Katan, C., Pedesseau, L., Kepenekian, M., Rolland, A. and Even, J. Interplay of spin-orbit coupling and lattice distortion in metal substituted 3D tri-chloride hybrid perovskites. *J. Mater.Chem.A* 3, 9232 (2015).
7. Yamada, K., Funabiki, S., Horimoto, H., Matsui, T., Okuda, T. and Ichiba, S., Structural phase transitions of the polymorphs of CsSnI_3 by means of Rietveld analysis of the X-ray diffractions. *Chem. Lett.*, 801 (1991).
8. Hao, F., Stoumpos, C. C., Cao, D. H., Chang, R. P. H. and Kanatzidis, M. G. Lead-free solid-state organic-inorganic halide perovskite solar cells. *Nature Photonics* 8, 489 (2014).
9. Thiele, G., Rotter, H. W. and Schmidt, K. D. Die kristallstrukturen und phasentransformationen von RbGeBr_3 . *Z. Anorg. Allg. Chem.* 559, 7 (1988).
10. Thiele, G., Rotter, H. W. and Schmidt, K. D. Kristallstrukturen und phasentransformationen von caesiumtrihalogenogermanaten (II) CsGeX_3 ($X = \text{Cl}, \text{Br}, \text{I}$). *Z. Anorg. Allg. Chem.* 545, 148 (1987).
11. Pauling, L. *The Nature of the Chemical Bond*. Cornell University Press, New York, 1960.
12. Birkholz, M. Modeling the shape of ions in pyrite-type crystals. *Crystals* 4, 390 (2014).
13. Shannon, R. D. Revised effective ionic radii and systematic studies of interatomic distances in halides and chalcogenides. *Acta. Cryst. A* 32, 751 (1976).
14. Pauling, L. The influence of relative ionic sizes on the properties of ionic compounds. *J. Am. Chem. Soc.* 50, 1036 (1928).
15. Gopikrishnan, C. R., Jose, D. and Datta, A. Electronic structure, lattice energies and Born exponents for alkali halides from first principles. *AIP Advances* 2, 012131 (2012).
16. Seo, D. K., Whangbo, M. H., Hillebrecht, H. and Thiele, G. Pressure-induced changes in the structure and band gap of CsGeX_3 ($X = \text{Cl}, \text{Br}$) studied by electronic band structure calculations. *Inorg. Chem.* 37, 407 (1998).
17. Huang, L. and Lambrecht, W. R. L. Electronic band structure, phonons, and exciton binding energies of halide perovskites CsSnCl_3 , CsSnBr_3 , and CsSnI_3 . *Phys. Rev. B* 88, 165203 (2013).
18. Chiarella, F., Zappettini, A. and Licci, F. Combined experimental and theoretical investigation of optical, structural, and electronic properties of $\text{CH}_3\text{NH}_3\text{SnX}_3$ thin films ($X = \text{Cl}, \text{Br}$). *Phys. Rev. B* 77, 045129 (2008).